PROBING THE DYNAMICS OF A SIMPLE JUMPING ROBOT ON HARD AND SOFT GROUND

A Dissertation
Presented to
The Academic Faculty

by

Jeffrey J. Aguilar

In Partial Fulfillment
of the Requirements for the Degree
Doctor of Philosophy in the
School of Mechanical Engineering

Georgia Institute of Technology
August 2016

PROBING THE DYNAMICS OF A SIMPLE JUMPING ROBOT ON HARD AND SOFT GROUND

Approved by:

Professor Harvey Lipkin,
Committee Chair
School of Mechanical Engineering
Georgia Institute of Technology

Professor Daniel I. Goldman, Advisor
School of Physics
Georgia Institute of Technology

Professor Kurt Wiesenfeld
School of Physics
Georgia Institute of Technology

Professor Alexander Alexeev
School of Mechanical Engineering
Georgia Institute of Technology

Professor Jun Ueda
School of Mechanical Engineering
Georgia Institute of Technology

Date Approved: 20 June 2016

To friends and family

ACKNOWLEDGEMENTS

It goes without saying that my graduate school experience, the quality of my work, and the person I am today would not have been the same without the countless people who have helped, mentored, supported and worked with me throughout the years. I would like to thank my advisor Prof. Daniel I. Goldman for taking me on as a student and being a great mentor and source of advice through graduate school. He has always pushed for excellence and his insight and curiosity as a researcher have not only directly influenced the quality of my own work but have also influenced my own sensibilities as an inquisitive researcher as well as my ability to communicate scientific ideas. I am infinitely grateful and indebted for his advocacy of me and support for my future career endeavors.

I would also like to thank my co-advisor, Prof. Harvey Lipkin, who supported me from within the Mechanical Engineering department and granted me the invaluable experience of TA for Robotics ME 4451. I would also like to give thanks to my other committee members, Prof. Alexander Alexeev, Prof. Jun Ueda, and Prof. Kurt Wiesenfeld for taking the time to be a part of my thesis committee. I thank Prof. Kurt Wiesenfeld in particular for his insights throughout the years, in particular during our collaboration with Alex Lesov on the hard ground jumping project. Their theoretical insight and effort in our project was invaluable. Special thanks to Alex for leading the effort on the theoretical analysis of my experimental results. Many thanks to Prof. Paul Umbanhowar at Northwestern University for continued support and interest in my work as well as helpful discussions throughout the years.

I am indebted to the incredible group of members, friends and alumni of the CRABLab which include but are not limited to: Ryan Maladen, Yang Ding, Chen Li,

Sarah Sharpe, Nick Gravish, Nicole Mazouchova, Andrei Savu, Feifei Qian, Tingnan Zhang, Mark Kingsbury, Will Savoie, Perrin Schiebel, Mateo Garcia, Andrew Masse, Robyn Kuckuk, Vlad Levenfeld, Vadim Linevich, Xiaobin Xiong, Bahnisikha Dutta, Jungsoo Park, Shengkai Li, Daria Monaenkova, Henry Astley, Jennifer Rieser, Hamid Marvi, Andy Karsai. Special thanks to Andrei for helping me construct the hard ground jumping apparatus. Special thanks to Nick Gravish for helping with automation. I would like to thank Andy for simulation efforts for jumping in granular media, as well as Allison Kim for recent efforts in intrusion force measurements. I would to thank Lionel London for insightful discussion on the dynamics of granular cone jamming and RFT, and honorary lab member Christian Hubicki, with whom I collaborated on optimized motion planning for jumping on granular media. His expertise in motion planning, enthusiasm and many discussions have been invaluable to the experience.

I would also like to thank my parents for being constants of love and guidance and always supporting my endeavors no matter what. I thank my brother, cousins and friends for enriching my life, and in general just being dope. Thanks!

SUMMARY

Legged locomotors effectively manipulate their appendages to traverse complex environments that are challenging for wheeled vehicles. Jumping is a common impulsive mode of legged locomotion for various animals. It is used as a primary mode of locomotion, to reach higher places, for predation, and also as a survival mechanism. With the advent of robots designed with inspiration from nature's excellent jumpers, it is important to understand the fundamental factors and mechanics that optimize jumping performance. Animals often amplify their jumping power with effective use of compliant structures by performing catapult jumps, squat jumps and countermovements. Certain animals utilize a variant of countermovement known as the stutter jump, where the jump is preceded by a small initial hop. Biologically inspired robots have taken a cue from nature to produce hopping gaits, catapults and squat jumps, yet systematic studies of the movement trajectories that maximize jumping performance are relatively scarce.

Jumping locomotors that exhibit such high speed movements have been described in certain literature by complex models. Yet even on hard ground, simple spring-mass jumpers can exhibit rich dynamics and provide insight into more complex systems. In this dissertation we discuss how, even on hard ground, the jumping performance of a one dimensional actuated spring-mass hopper is sensitive to its active self-deformation strategy, which induces motion coupled to both aerial and passive spring-mass dynamics. In concert with simulation, we systematically varied the robot's actuation trajectory and uncovered how a countermovement produced a stutter jump that is optimal at a frequency lower than the natural frequency, f_0, and a squat jump produced a single jump that is comparably optimal but at a higher frequency, which requires

more internal power. An analysis of the dynamical model revealed how optimal lift-off results from non-resonant transient dynamics.

We then posited that understanding the dynamics of rapidly self-deforming objects in complex media would require a robophysics (the pursuit of principles of self generated motion) approach that could grant new insights into both nonlinear robot dynamics and soft matter physics. Thus, we studied the performance and dynamics of the spring-mass hopper in granular media via a three-fold approach. First, we performed jumping experiments in a bed of granular media that was constructed such that it controlled volume fraction (loose packed, $\phi = 0.58$, to close packed, $\phi = 0.63$) via air fluidization, air pulses, and bed shaking (Fig. 38) and automated the performance and kinematic data collection of hundreds of jumps in succession. Second, we performed systematic empirical measurements of quasistatic resistive forces during slow constant speed intrusions. We also performed a particle image velocimetry analysis of granular flow during jumping that granted insights into substrate inertia and a jammed granular cone that developed beneath foot during intrusion. Finally, we compared experimental jumps with a simulation using various granular force models acting on the foot which combined velocity-dependent inertial drag and depth-dependent hydrostatic friction. These experiments led to the development of a reactive force theory incorporating a granular cone-based added mass force that was able to reproduce experimental jump heights in simulation. This model was then embedded into a motion planning optimizer to produce optimal open-loop controlled jumps.

TABLE OF CONTENTS

LIST OF TABLES

LIST OF FIGURES

CHAPTER I

INTRODUCTION

1.1 Motive and Overview

Terrestrial organisms [13][61] as well as robots [128][163][162] run, climb, and jump over diverse terrain to traverse complex environments in ways that conventional wheeled vehicles are unable to accomplish [20], and do so by effectively bending their multi-jointed appendages and bodies. In particular, jumping is a common mode of locomotion for various animals [84][29][174][130][219][1][42] as well as for robots [20][183][173][78]. Unlike periodic gaits such as hopping or running, whereby energy generated in previous cycles can be leveraged to efficiently sustain motion, jumping relies almost purely on a transient burst of activity to produce take-off from rest. While bioinspired robots have utilized jumping mechanisms revealed from biological studies, there have been few systematic studies of the dynamics of these transient behaviors, particularly on complex media like sand. And with the advent of robots taking inspiration from nature's excellent jumpers, there is a need to understand the mechanisms that influence jumping performance.

This dissertation presents a robophysics approach (the pursuit of principles of self generated motion [4]) to systematically study the dynamics of jumping on both hard and deformable ground. For jumping on hard ground, the present work expands on the results from Aguilar et al. [3], which characterized the dependence of jumping performance on the robot's hybrid air/ground dynamics, and analyses how relative jumping performance and power requirements of different actuation strategies change at different as a function of mass, gravity, stiffness and forcing amplitude. To contrast with the dynamics of jumps on hard ground (in which the unyielding ground supplies

the necessary normal force to counteract downward motion), we study a relatively simple deformable medium: dry granular media, which can exhibit both solid and fluid-like dynamics. Through the simultaneous analysis of both the robot and granular dynamics during jumping, our study reveals not only actuation principles crucial to jumping on complex media, but also new granular physics [2], like an added mass effect induced by a jammed granular cone beneath the robot's foot. Additionally, in collaboration with the Professor Aaron Ames' group at Georgia Tech, we incorporate these granular dynamics into a motion planning optimizer to produce optimal open loop controlled jumps.

Within this framework, this Chapter (I) provides an overview of previous work on jumping animals, robots and theoretical models as well as granular modeling. Chapter II presents research on hard ground jumping, Chapter III presents our research on jumping on granular media, and Chapter IV concludes and proposes future directions.

1.2 Hard Ground Jumping

1.2.1 Biological Jumping

Jumping is an important and common behavior among legged terrestrial locomotors in nature. Animals jump to escape predators and conversely as a predatory behavior [107][140], to reach higher ground, and even as a primary means of locomotion. As such, many animals have become specialized in jumping. Cats, bushbabies, frogs, and a variety of insects are some of the best jumpers (Fig. 1).

There has been considerable interest over the years in understanding the mechanisms of jumping that maximize performance [90]. At the most basic level, jumping involves a transient burst of motion in which the muscles of an animal's grounded appendages shorten and lengthen, interacting with bone and connective tissue to generate a force that propels the body away from the ground, generating lift. Size, relative muscle mass used for jumping, and relative limb length are factors that can

affect jumping performance [227][52]. Yet in various animals, the overall power output of a jump is many times greater than the maximum power provided by muscles used for jumping [29][66][31]. The following sections provide an overview of research on the mechanisms that affect the jumping performance of animals.

We note that there are many metrics used in literature to quantify jumping performance. For example, Wilson et al. [215] considered take-off velocity, jump distance, maximum power, average acceleration, and contact time in studying how jumping performance changed with body mass amongst striped marsh frogs. These metrics scaled differently among different species and groups, and the jump performance metrics vary amongst different studies. In our research on the dynamics of a simple jumping robot[3, 2], we only considered one dimensional vertical jumping. We used jump height as the performance metric, which is directly related to take-off velocity. In many biological studies, the notion of jump "ability" was used, in which, jump height or distance was compared against the animal's size (typically snout-vent length) [227, 174]. A similar nondimensionalization is made later in our analysis in which jump height is scaled with forcing amplitude (for a single cycle of sinusoidal forcing), which may be analogous to leg length.

Figure 1: Various jumping animals: *Felis catus*, *Galago senegalensis*, *Craugastor fitzingeri*, *Homo sapiens*, *Petrogale xanthopus*, and *Pulex irritans*. Michael Jordan photo courtesy of NBA, other images courtesy of Wikipedia.

1.2.2 Effects of Size and Morphology

Organisms that are adept at jumping exist over a large range of sizes, from fleas to kangaroos. Larger animals typically have more muscle mass and produce higher jump height (Fig. 2(a)). There have been numerous studies in which this scaling effect has been examined directly within specific animal species. Zug [227], for example, studied the jumping performance of 84 different species of frogs. The amphibians were tested in rectangular arenas in the laboratory, and their jump distances were recorded.

Within a species, jumping distances increased with body size, characterized by snout-vent length (head to tail). Similar results were found in Wilson's study of striped marsh frogs when comparing differences in mass to various performance metrics, all of which correlated positively with increases in mass [215]. In a study comparing the jump performance of 15 species of *Anolis* lizards, jump distance increased with increasing snout-vent length. Demes compared the kinematics of 4 species of Malagasy lemurs of varying body mass [59]. Since the animals were observed jumping in their natural habitat, jump heights were not systematically measured. However, it was observed that acceleration times increased with increasing body mass.

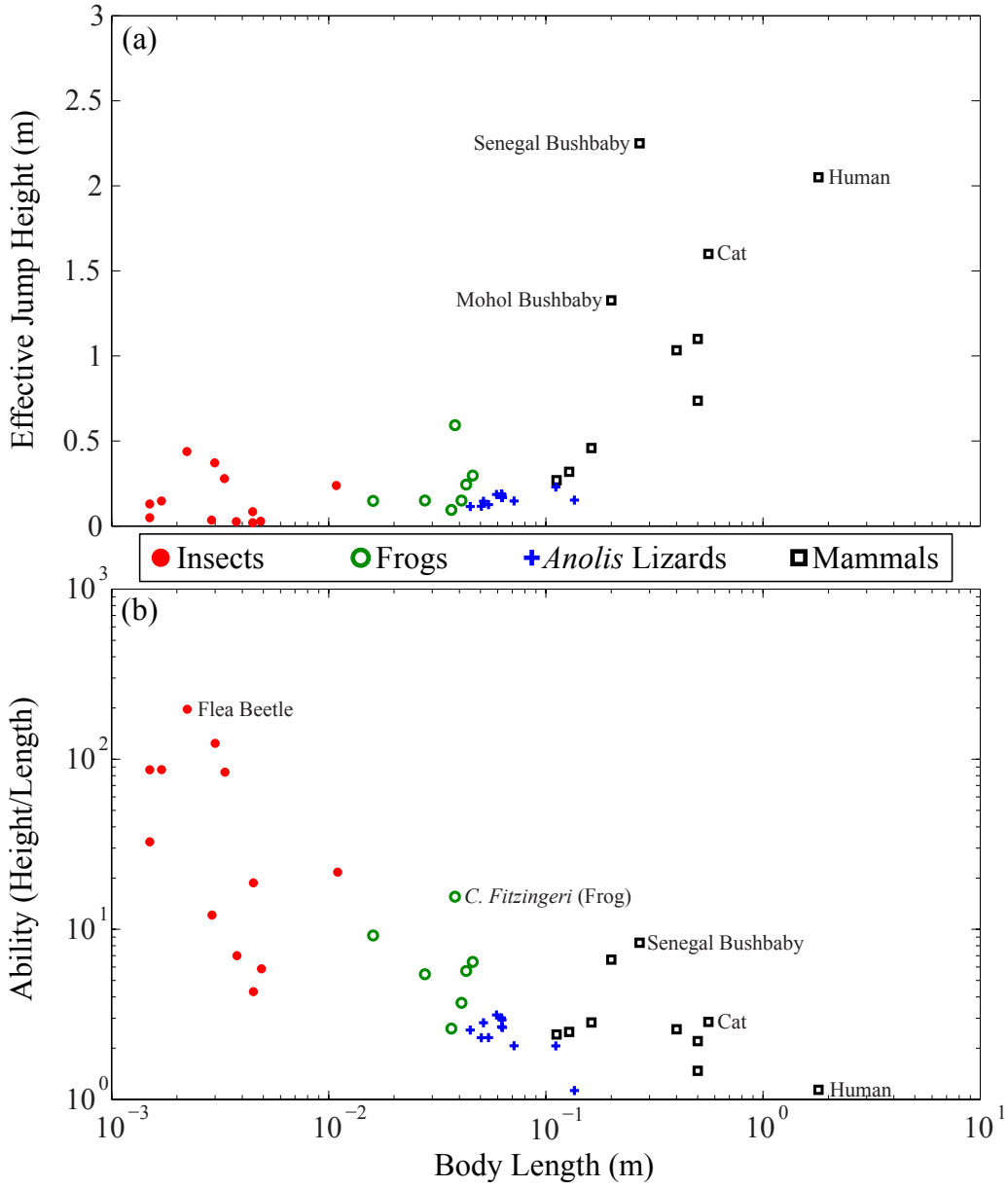

Figure 2: Comparing the jump performance of different sized animals. (a) Jump height vs. size. (b) Jumping ability vs. size. Biological jump height data compiled from numerous studies [84, 29, 70, 94, 44, 174, 175, 227, 52, 53, 179, 130, 206, 219, 91, 88, 60, 59, 197, 1, 97, 120, 56, 42, 208, 123, 100, 116, 68, 143]. Note: Values shown for frogs were reported as distances rather than heights; angles of take-off vary, but are approximately around 45° [139].

Many studies have demonstrated that, when considering jumping ability (jump height relative to body size), the relationship is inverse to body size (Fig. 2(b)). Among six species of Anurans (frogs), size was inversely correlated to relative jumping distance [174]. Similarly, Zug also found that, while absolute jumping distance of frogs increased with increasing snout-vent length, relative jumping ability decreased with increasing snout-vent length [226][227]. The values related to this inverse relationship varied among different species. Particularly, amongst different species, performance differed depending on leg morphology. Rand's findings revealed a positive correlation between relative hind limb length and jumping ability; arboreal frogs had moderately long legs relative to body size and high jumping ability, whereas the terrestrial frogs possessed the shortest legs and poorest jumping ability [174]. Further evidence supporting the effects of morphology on jumping performance in frogs was found in a set of take-off experiments with seven Anuran species [53]. Both relative leg muscle mass and relative hind leg length, which together characterized contractile potential, correlated positively with take-off velocity. Some studies found no correlation between hind limb length and jump performance [65][108]. Additionally, amongst the arboreal species, high tree jumpers under-performed animals that jumped on grass reeds. For primates, branch compliance may be too large to be advantageous in locomotion, and instead increases energy cost of arboreal locomotion [12]. Similar principles may apply with grass reed dwelling frogs, requiring them to compensate with increased muscle mass.

Jump performance is also affected by morphology in other animals. Both hind limb length and lean extensor muscle mass relative to body mass have strong positive correlations with take-off velocities in cats [91]. In *Anolis* lizards, hind limb length, forelimb length, and tail length all correlated with jumping distances in 15 different species [130]. Yet, since there were also strong correlations in these morphological traits with body size for these species, a phylogenetic and statistical analysis was

performed which found that the evolution of hind limb length was associated with the evolution of jumping ability regardless of body size.

1.2.3 Elastic Energy Storage

Animals have been observed to amplify the power output of their muscles during jumping [66]. Fleas, for example, jump by generating impulsive forces that have a duration of only 0.75 ms, while the latency in the muscle is on the order of 3 ms, making it impossible to generate sufficient power and propel the jump through means of conventional muscle forcing [29]. Similarly, in locusts, maximum power output of each extensor tibiae muscle is 36 mW, while the max power output of the jump is about 0.75 W, or a tenfold power amplification [28]. The *Galago senegalensis* (bush baby) has an excellent jump capability of 2.25 m or six body lengths. Assuming constant acceleration during push off, Bennett-Clarke [28] estimated a power output of 2350 W kg^{-1} for the bush baby. He inferred that, due to the fact that this value was far higher than typical values for theoretical maximum powers in muscles (such as 371 W kg^{-1} in frog hind limb muscles [132]), power amplification occurred in bush babies [30]. This was later confirmed through experimental measurements [87]. Thus, many animals must use power amplification mechanisms to propel their jumps.

Power amplification in jumps result from energy storage in elastic elements in the appendages responsible for jumping. In vertebrates, this elasticity is largely found in the tendons, which tend to have uniform properties among many mammalian species, with a nearly constant tangent modulus of elasticity of 1.5 GPa for stresses greater than 30 MPa [32]. The tangent modulus of elasticity is an estimate of Young's modulus where the stiffness used in the modulus calculation has been approximated from force vs. displacement curves of tensile loading tests on tendons. Tendons have low energy dissipation. When tendons recoil, they dissipate only 7% of the work done when stretched as heat [11]. The energy that can be stored from tendons has been

well documented in other animals [146] and was found to be up to 52 J in humans while jogging [98].

The muscle-tendon complex, such as that of the main extensor of the human foot, also stores elastic energy [98]. Hof's study used strain gages, a potentiometer, and a piezo-electric accelerometer to measure moments and angular displacements on 12 humans that bent their ankles in an ergometer. A muscle-tendon complex model was considered that identified two elastic components, one in series (SEC) with the contractile element and one in parallel (PEC). The SEC was identified as the Achilles tendon. Using this model, the measurements of moment and angular displacement were converted to values of stiffness. The effective stiffness in the complex was calculated to be 306 Nm rad^{-1} at a muscle moment of 100 Nm, which agreed well with Hooke's law estimates using data on Young's modulus and cross sectional areas of the Achilles tendon. Azizi and Roberts found that the muscles of frogs are more compliant than those of mammals, which improves the muscles' force production during jumping [24].

The role of elastic energy storage improves jump performance by amplifying power output [11]. Muscles are restricted in the amount of power that they can produce, which is determined by the product of muscle force and shortening speed. As the shortening speed increases, the force available decreases [96], with the shortening speed being optimal at around 30% of the max shortening speed [216], and since tendons can recoil at a faster rate than muscles shorten, they can act to amplify power.

This power amplification is evident in dramatic fashion in insects like the flea, which possess a catapult mechanism that slowly coils and tenses elastic material known as resilin, while a catch mechanism keeps the legs locked in a flexed position until maximally tensed and then releases all the stored energy at once [29]. This is a similar concept to flicking your fingers. Bennett-Clarke found the jump height of a

rabbit flea to be 4.9 cm, or over 30 body lengths, and a human flea (*Pulex irritans*) of comparable mass was recorded jumping to a height of 13 cm and considered capable of up to 20 cm jumps [29], making fleas among the best jumpers in the world in terms of jumping ability. Similar catapult mechanisms have been found in other insects such as click beetles, flea beetles, and locusts [70][44][94]. And while frogs do not have a catch mechanism similar to insects, their own weight is considered to be a catch mechanism [179, 23]. A frog's hind limb muscles are uncoupled from whole body movement, and as such are able to shorten their muscles and pre-stretch their tendons and store elastic energy before any movement occurs, doing so at a slower rate than if whole body movement and muscle shortening were coupled [179]. This effective catapult mechanism in the frog makes its jumping strategy more similar to insects than to other squat jumping vertebrates.

Other vertebrates, however, have not evolved such catch mechanisms which enable the release of stored elastic energy as a catapult, and must instead rely on specific inertial movement strategies to fully leverage power amplification through elastic energy storage. A study [77] of a theoretical model consisting of a muscle, compliant element and inertial load in series demonstrated how such a system could experience power amplification with tendon recoil. The model revealed that power amplification is primarily influenced by the amount of inertial loading.

The two most common methods for jumping are countermovements and squat jumps. A countermovement is characterized by starting upright, and then quickly squatting and pushing upward. A squat jump is characterized by starting from rest in a squatting position. Alexander developed a theoretical bipedal model of jumping that predicted that animals that produce insect-like ground forces (characterized by high ground forces relative to body weight, $58mg$, m for mass and g for gravity) would benefit exclusively from catapult jumping, which has been found to be a common method of jumping in insects [8]. For animals that produce bush baby-like ground

forces ($12mg$) or human-like ground forces ($2.3mg$), countermovements and catapults would both achieve greater jump heights than squat jumps, catapults more so in bush baby type forces. The countermovement causes elastic energy storage to occur through passive inertial loading during the preparatory phase, which pre-stretches the muscles and tendons that then recoil and amplify power during the push-off phase.

The performance of countermovements and squat jumps has been compared in humans in a number of studies [123][208][120]. The countermovement always performs better than the squat jump. In fact, more than twice as much energy is stored in the tendons during a countermovement than a squat jump [208]. A similar result was found in a study of jumping in *Anolis* lizards, in which the species that performed the countermovement produced a greater muscle mass specific power output than the species that performed a regular squat jump [206]. Many prosimian primates, like the bush baby (*Galago senegalensis*), have also been observed performing countermovements [88][60][59][1]. In bush babies, elastic energy storage occurs both during the preparatory phase of the jump and during the early push-off phase. The energy is then suddenly released at take-off. Thus the bush baby likely performs some combination of a countermovement, squat jump and catapult [1]. The countermovement is so pervasive among prosimian primates that it is performed regardless of substrate. It was observed in vertical jumps in both natural environments on compliant branches [59] as well as in a laboratory setting on rigid force plates [88], and even by clingers that jump horizontally off of tree trunks to other trunks [60].

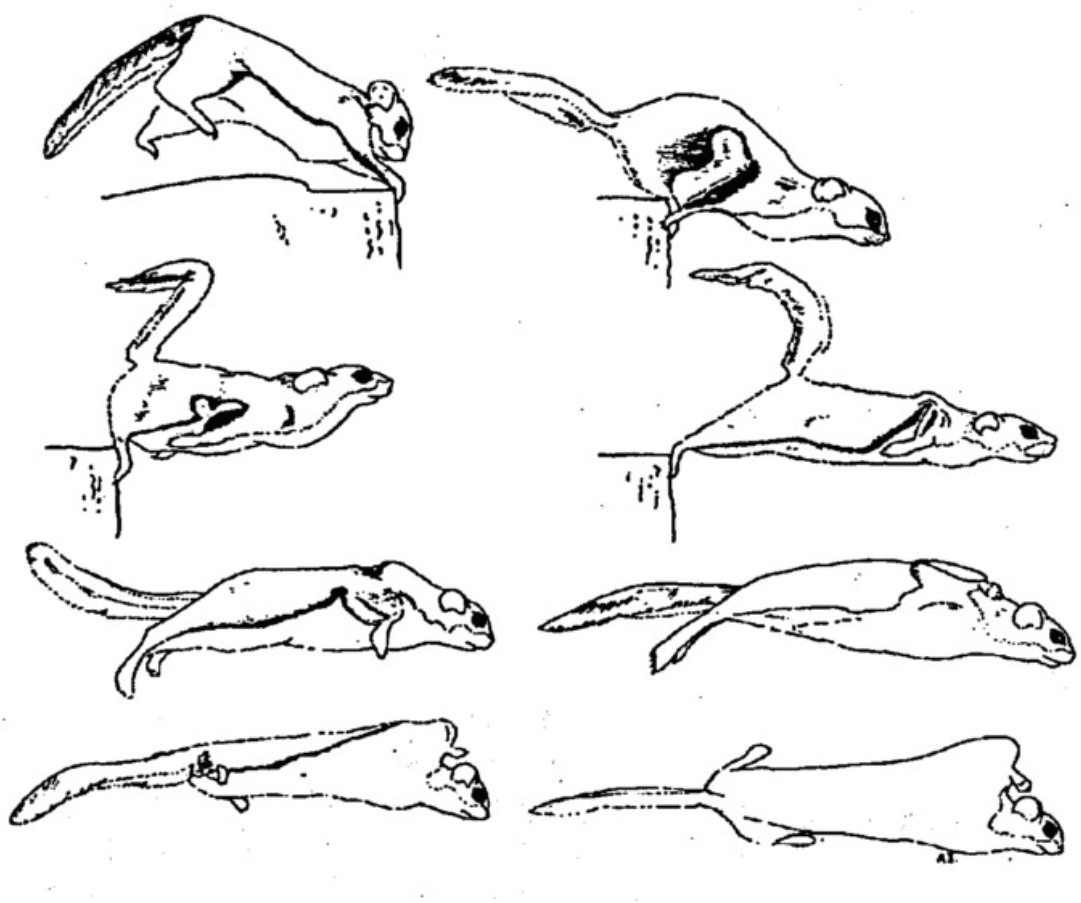

Figure 3: Illustration of the jump sequence of a flying squirrel [116].

Similar principles of elastic energy storage have been used to explain the efficient hopping gait of various marsupials [34][117][10][35]. A preparatory hop preceding the countermovement is a particularly interesting version of the countermovement that has been observed in some species. In this dissertation, we call this maneuver a stutter jump. Demes' study reported this behavior for all four species of lemurs observed [59]. In Gunther's study, this was observed in the *Galago moholis* jumps [88]. The stutter jump was also observed in flying squirrels, chipmunks and red squirrels prior to take-off from the edge of a pine board [68][116](Fig. 3). The stutter jump in the animals was so consistent that it was referred to as a "stereotyped preliminary hop". Bush babies may on occasion produce a movement similar to the stutter in

which a jump occurs "out of previous forward motion", which, though not clear, likely suggests a running start, similarly introducing additional momentum to the start of the countermovement [197]. In comparison of jumping versus steady state hopping in wallabies, a "moving jump" was utilized by the animal in which a short-lived hopping gait to the force plate preceded the jump to an elevated platform [143]. The forward velocity of the hopping gait did not differ between steady hopping and jumping.

Table 1: Various animals and their observed jumping strategies

Animal	**Jump Types**	**Stutter?**
Insects (fleas, click beetles, locusts, flee beetles) [84][29][70][94][44]	Catapult	No
Frogs [174][175][227][52][53][179]	Squat / Catapult	No
Anolis Lizards [130][206]	Countermovement, Squat	No
Cats [219][91]	Squat	No
Lemurs (*Avahi laniger, Indri indri, Propithecus diadema, Propithecus verreauxi*) [88][60][59]	Countermovement	Yes
Senegal Bushbabies [197][1]	Countermovement / Squat / Catapult	Yes
Mohol Bushbabies [88]	Countermovement	Yes
Humans [97][120][56] [42][88][208][123][100]	Countermovement, Squat	Yes (Volleyball)
Rodents (Chipmunk, Red Squirrel, Flying Squirrel) [116][68]	Countermovement	Yes
Yellow footed rock wallabies [143]	Hop	Yes

In humans, drop jumps, which have similar qualities to the stutter jump, have been compared with the performance of regular countermovements. The drop jump is a countermovement preceded by a drop from a slightly higher platform. In general, the performance of a drop jump is comparable to the countermovement [42], and is better than the squat jump [120]. But whether the drop is better than regular

countermovements is under debate and seems to vary among men and women as well as males of varying athletic ability[120]. In volleyball, two different jumping techniques are used: a "hop jump", which is a quicker stutter jump while using both feet at the same time, and a step close approach, which is more of a skip, with one foot after the other. Both jumping techniques produced comparable jump heights, though the hop jump, which is the quicker and more impulsive approach, required greater muscle effort [56]. Another drop jump study uncovered how a proper prelanding angular velocity of the knee joint in which a larger knee flexion just before landing would produce a bouncing type drop with greater take-off velocity [100] (Fig. 4). These findings suggest that the movements involved in the stutter jump must be precisely timed to achieve a mechanical and energetic advantage over a regular countermovement.

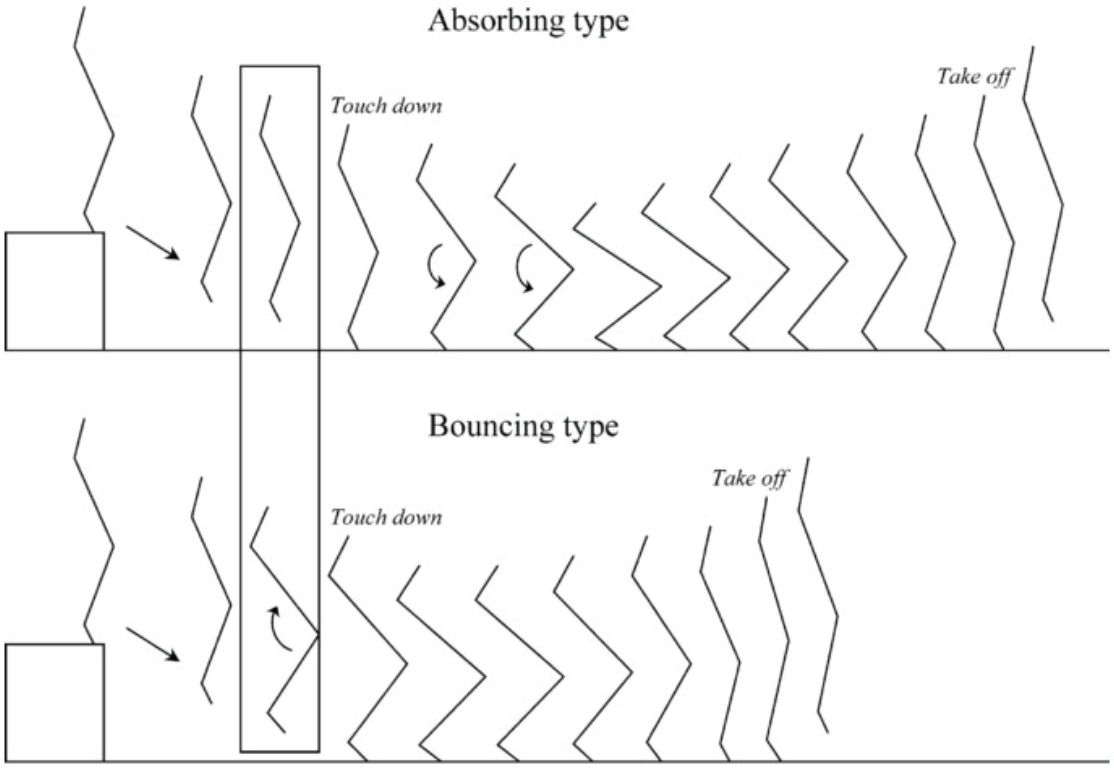

Figure 4: Illustration of two type of drop jumps [100].

1.3 Jumping Robots

1.3.1 Biological Inspiration

In robotics, biologically inspired designs have resulted in machines that are able to traverse diverse terrain. Animals are regularly tasked with maneuvering complex environments, and it can be argued that they have evolved to become adapted to these challenging environments in ways that conventional technologies cannot yet rival. Particularly, wheeled vehicles are the accepted standard of terrestrial locomotion using conventional technology. Wheeled locomotion is effective at traversing smooth terrain, but can fail when confronted with large obstacles.

Armour et al. [20] and Sayyad et al. [183] provide extensive reviews of robots that researchers have created which utilize hopping and jumping strategies. Sayyad et al. highlight the advantages as well as the challenges with using hopping gaits versus wheeled solutions in robotic locomotion. They argue that legged locomotion can be superior, allowing for active body suspension, isolated footholds, and generally dealing less damage to the environment than wheeled vehicles [183]. Most importantly, however, legged robots are capable of more complex maneuvers and thus have increased adaptability to uneven and complex terrain.

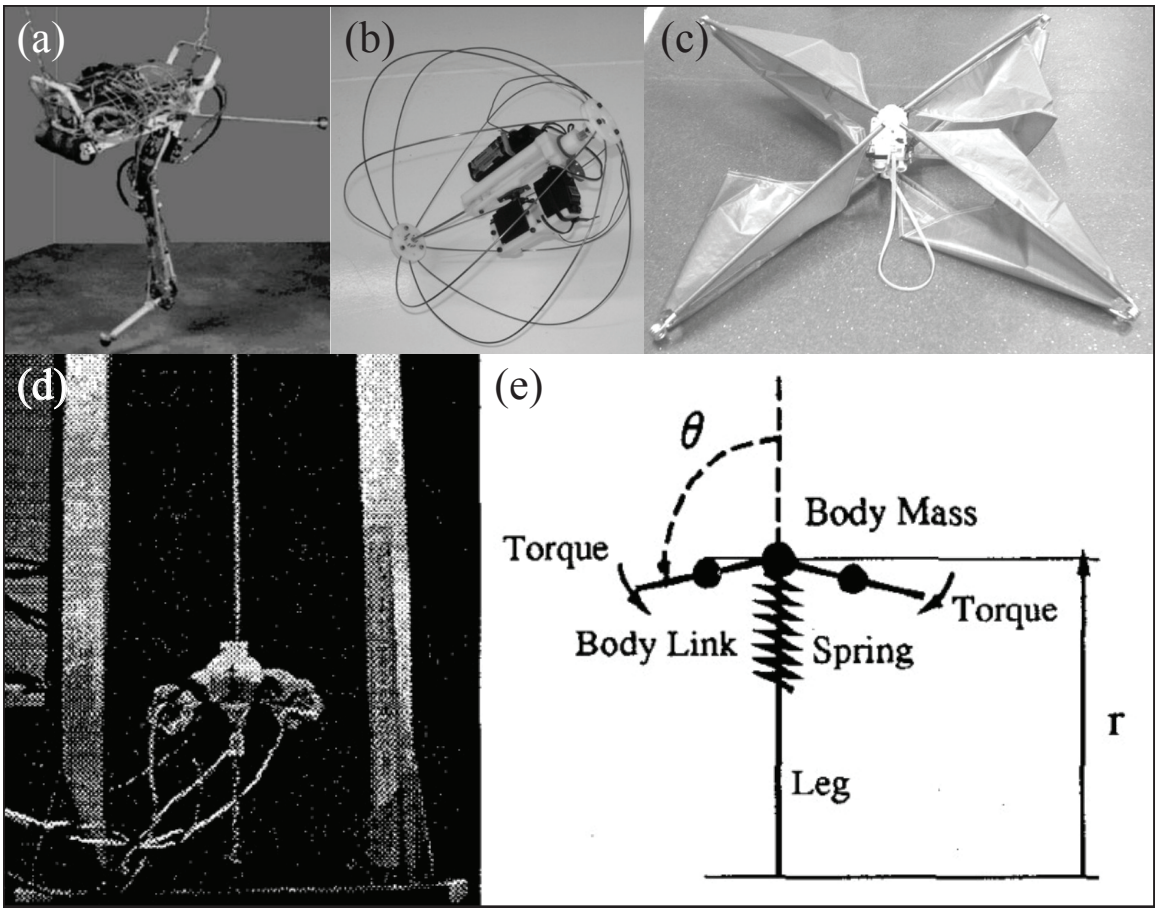

Figure 5: Biologically inspired jumping robots. (a) Uniroo [221]. (b) Jollbot and (c) Glumper [20]. (d)(e) Arm swinging robot [156].

Researchers have developed interesting robotic interpretations of animal jumping and hopping mechanisms. The Uniroo was a 3-leg-link hopping robot based on kangaroo locomotion, with a soleus spring arrangement [221] (Fig. 5(a)). Using hydraulic actuators, the hopper achieved over 40 hops in a given trial. Armour and researchers developed two jumping robots that utilized the catapult jumping mechanism: Glumper and Jollbot [20] (Fig. 5(b,c)). As the name would suggest, the Jollbot, was inspired not only by the catapult jumping mechanisms seen in various insects and frogs, but also the rolling ability of certain organisms like the web-toed

salamander and tumbleweed. It used a combination of jumping and rolling for locomotion, in which the rolling mechanism also worked to orient the direction and angle of jumping. The Glumper, inspired by the gliding capabilities of flying squirrels, consisted of four legs surrounding the top and bottom of its exterior body with two leg links each to perform a catapult jump. The Glumper could also glide using the air resistance on the sails attached to the legs. The Glumper performed better than the Jollbot, jumping nearly 2 m high. One interesting adaptation to hopping robots was the addition of two rotating symmetric arms with masses attached, similar to how humans use arm swing to improve jump height [156] (Fig. 5(d)). The robot was able to perform high jumps while hopping in place.

1.3.2 An Engineer's Perspective

Legged robots that can adapt to complex environments also have more complex dynamics than wheeled vehicles, with distinct phases and gaits creating nonlinear behavior. This can pose a challenge to engineers to control these robots. Also, wheeled vehicles can carry larger payloads relative to their weight, and in legged robots, greater carrying loads require larger actuators which in turn increases the carrying load. However, while there may generally be increases in the complexity in legged robots versus wheeled vehicles, the hopper constructed by NASA's Jet Propulsion Laboratory (JPL) (Fig. 7) was developed with the premise that wheeled vehicles for celestial exploration can have a large number of actuators and linkages, increasing complexity of control and chance of failure [89]. The resulting robot was able to reduce the number of actuators and jump via a catapult mechanism using a six bar linkage, and also had self-righting capabilities after landing.

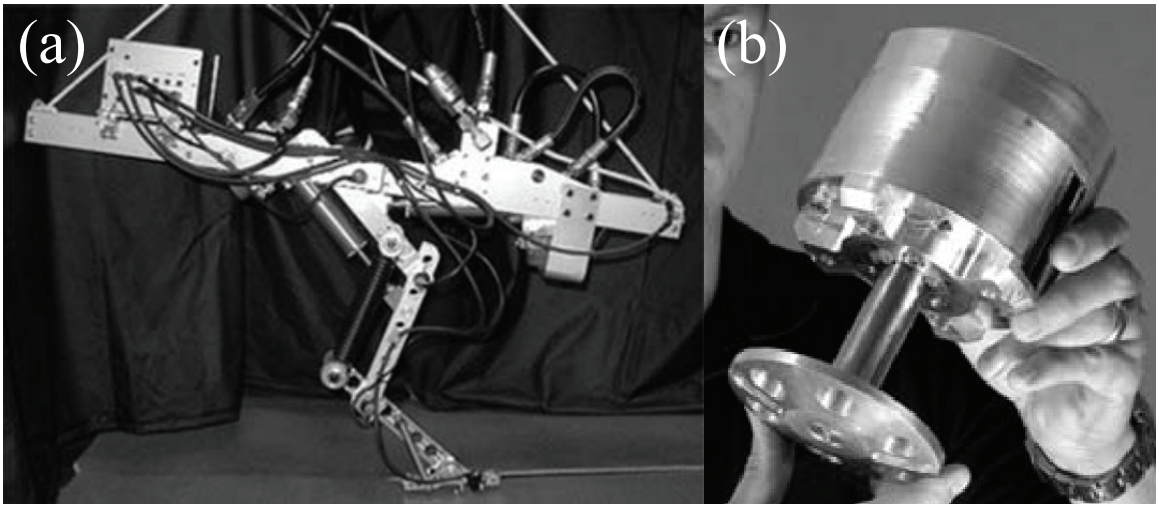

Figure 6: Hopping robots of varying complexity. (a) Kenken [104]. (b) Sandia Hopper [78]

Hopping robots have typically been built with an engineering approach to the challenges intrinsic to legged locomotion. The intent has not only been to apply a biologically observed physical principal of jumping or hopping, but also to improve designs by tackling these challenges. For example, one of the initial improvements to the design of hopping robots was to change actuation technologies from pneumatic [173] and hydraulic [221] to electric actuators such as small DC electric motors [5]. Such motors were chosen as the cleaner, safer and less expensive alternatives while still having high torque-weight ratio [183].

Researchers have also developed hopping robots with increased mechanical complexity (e.g. more articulated links). Such an increase in complexity can be seen in Kenken [104], which was a hopping robot based a bio-inspired articulated 3-link leg (Fig. 6(a)). Hyon and researchers argued that there are practical advantages to an articulated leg such as large clearance between foot and ground, and while there is added complexity compared to a telescopic leg, the structure is simple to build, since it connects two link ends with a rotary joint. Hoppers such as Kenken as well as Uniroo [221], Zhang's Uniped [225], and Berkemeier and Desai's robot had more leg

links than most other hoppers [33]. However, complexity, does not necessarily correlate to performance, as evidenced by Sandias simple telescopic hopper, which was capable of hopping 20 feet in height and about 100 hops on one tank of fuel [78](Fig. 6(b)).

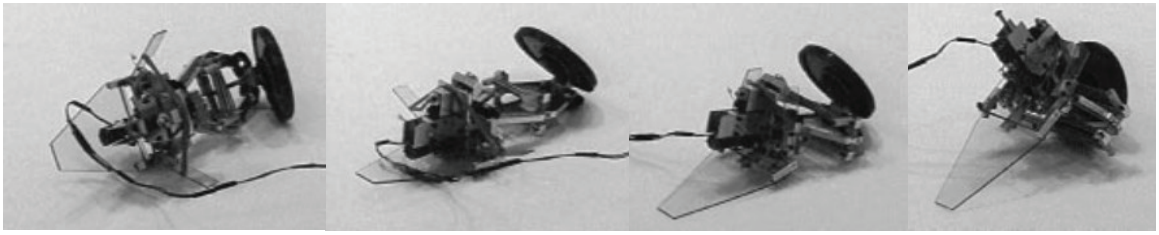

Figure 7: Self-righting sequence of the JPL Hopper V2 [89].

Researchers have worked to make robots that are functional and autonomous. These robots are not necessarily made as experimental platforms to learn the fundamental physics behind animal jumping. Thus, relatively few robot jumpers are treated as simple experiments constrained to only move in the vertical direction [156][147][204][168]. Jumping robots typically are allowed to move in 3D [20][184][154], or 2D with a planarizer [160][225][136][33][47]. Even the simplest one-legged, one-link, hoppers have both active [173] and passive [178] balancing strategies. And some robots even have self-righting or orienting capabilities [20][89](Fig. 7). In contrast, this dissertation presents a robophysics approach (the pursuit of principles of locomotion [4]) to study the mechanics of jumping, whereby a simple one-dimensional spring-mass hopper is automated to perform jumps at systematically varied parameters of actuation and substrate properties (in the case of jumping on granular media, see Chapter III). This methodological approach combined with analysis and simulation revealed fundamental principles of jumping.

1.3.3 Robotic Jumping Strategies

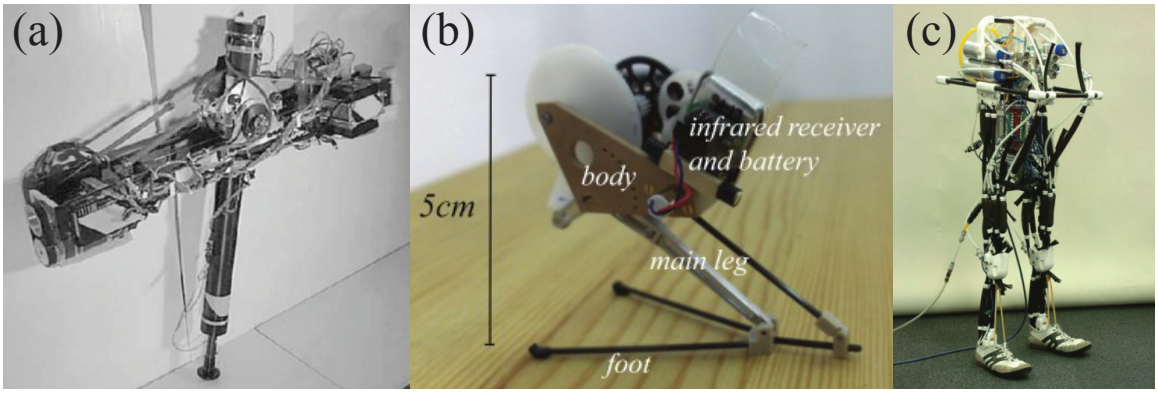

Figure 8: Robots with various jumping methods. (a) Hopping in ARL Monopod II [5]. (b) Catapult in the miniature 7g robot [122]. (c) Squat jump in Niiyama's bipedal robot [153].

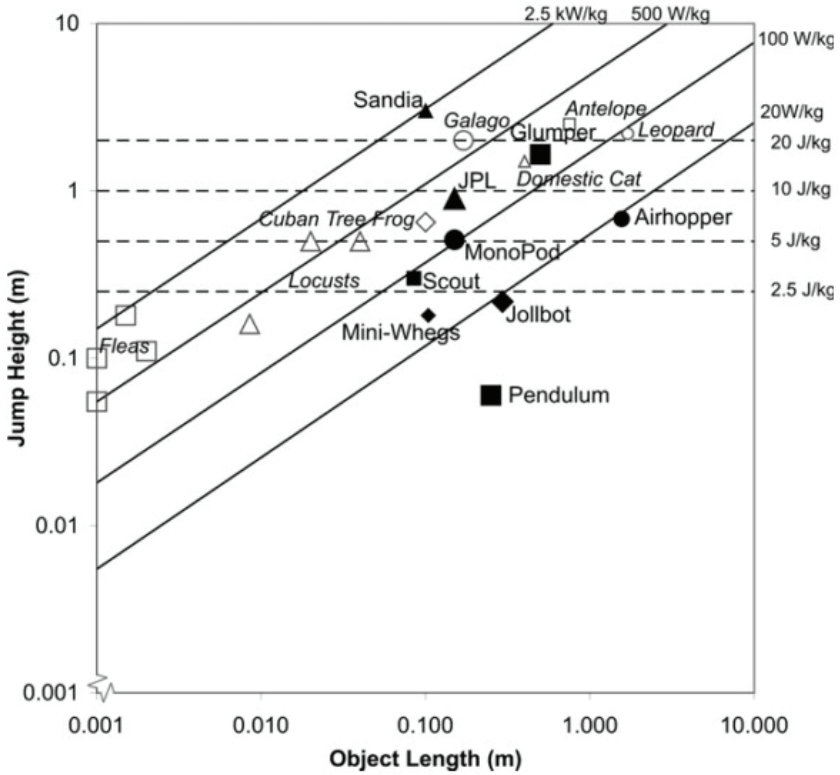

Figure 9: Jump height versus size of various catapulting robots compared with animals [20]

The jumping strategies employed in robots are generally classified as hopping, catapult or squat jump, the last two of which are forms of maximum height jumping (Fig. 8). There are many designs that use the catapult mechanisms often seen in insects [191][200][20][184][89][16][150][122]. The jump heights of many of these catapulting robots have been compared with animals (Fig. 9) and have a similar positive correlation with body size as shown in Figure 1. The large majority of the jumping robots that exist are hoppers (Table 2). Hopping is a qualitatively different mode of locomotion than maximum height jumping, since maximum height jumping produces much higher power output than in hopping gaits [143]. While the work of this dissertation focuses on maximal height jumping, it is important to highlight hopping robots, since the hopping gait stores tendon elastic energy through body movements like the squat jump and countermovement. Additionally, hopping robots tend to have simpler and smaller designs than the squat jumping robots, which can be bipedal and have as many as 4 leg links, based on animals such as humans and dogs [153][154][25]. These simple designs can be beneficial to consider for an experimental study on the fundamentals of jumping.

1.4 Theoretical jumping models

1.4.1 Introduction

Researchers have proposed a variety of theoretical models used to describe and understand different kinds of jumping such as hops and vertical jumps. Mathematical models have been used to express the fundamental locomotor and structural features of jumping. These models range in complexity. Simple models can often explain the underlying properties of jumping in specific manners using fundamental physical principals with a reduced number of parameters. These models make numerous assumptions of the leg structure and physics involved, and as such constrain the models

Table 2: Various robots and their jumping strategies

Jumper	Number of Leg Links	Actuator Type	Jump Type
Balancing Robot [141]	1	Electric Solenoid	Hopping
Raibert Hopper [173]	1	Hydraulic	Hopping
Prosser and Kam [168]	1	Electric	Hopping
Mehrandezh [147]	1	Electric	Hopping
Okubo [156]	1	Electric	Hop in Place
Ringrose Monopod [178]	1	Electric	Hopping
Bow-Leg [47]	1	Electric	Hopping
ARL Monopod II [5]	1	Electric	Hopping
Wei Monopod [213]	1	Electric	Hopping
Sandia [78]	1	Internal Combustion	Hopping
Peck [161]	1	Electric	Hopping
Pendulum [93]	1	Electric	Momentum Based (arm swing)
Takeuchi [194]	1	Pneumatic	Hopping
Uno [204]	1	Electric	Hopping
Scout [191]	1	Electric	Catapult
Akinfiev [6]	1	Electric	Hopping
Dashpod [51]	1	Pneumatic	Hopping
Slip Hopper [182]	1	Electric	Hopping
Rescue Bot [200]	1	Pneumatic and Solenoid	Catapult
Jollbot [20]	1	Electric	Catapult
Grillo [184]	1	Electric	Catapult
Lee Monopod [126]	2	Hydraulic	Hopping
Papantoniou [160]	2	Electric	Hopping
Olie [136]	2	Electric	Hopping
JPL Hopper V2 [89]	2	Electric	Catapult
Luxo [7]	2	Electric	Hopping
Allison Monopod [16]	2	Electric	Catapult
Mini Whegs [150]	2	Electric	Catapult
Airhopper [118]	2	Pneumatic	Hopping
Acrobat-Like [125]	2	Pneumatic	Hopping
Ohashi [155]	2	Electric	Hopping
Glumper [20]	2	Electric	Catapult
Miniature Hopper [122]	2	Electric	Catapult
Uniroo [221]	3	Hydraulic	Hopping
Zhang Uniped [225]	3	Electric	Hopping
Berkemeier [33]	3	Electric	Hopping
KenKen [104]	3	Hydraulic	Hopping
Niiyama [153]	3	Pneumatic	Squat Jump
Mowgli [154]	4	Electro-pneumatic	Squat Jump
Biarticular Bot [25]	4	Electric	Squat Jump

to describe a particular type of jumping. Such models are not only useful in describing locomotion in animals, but also serve to simplify control of biologically inspired robots [39]. For example, the spring-mass model used to describe running and hopping in animals can be utilized in robotics such that the running gate stabilizes in the presence of disturbances without having to sense and actively adjust for such disturbances [39]. Simple models are often called templates (Fig. 10) and can be used in more elaborate fashion by treating them as individual features of a body such as legs and leg links to improve modeling accuracy [76]. More complex models have also been studied to solve problems that cannot be considered with a single telescopic leg or 2-link articulation [9] and have also been used to understand the role of specific muscle groups [157][205].

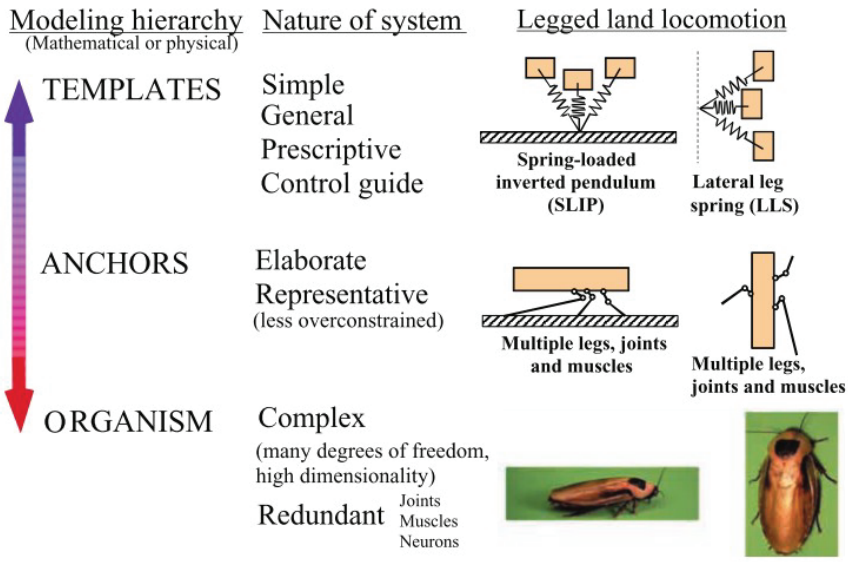

Figure 10: Illustration of template models [76]

Physical models can also be useful to both verify mathematical models and perform experiments that are not feasible in animals [9]. For example, McGeer verified the predictions of his mathematical model of bipedal walking by constructing a physical passive walker, which showed that, when put on a slope, the model would enter

a stable un-actuated walking gait [142]. Most models used in jumping are described by mathematical differential equations, such as the spring-loaded inverted pendulum (SLIP) model. However, while engineers have employed this SLIP model in the design of hopping robots [183], the robots themselves are not generally treated as physical or robotic models, rather more as functional robots.

1.4.2 Hopping

To describe hopping in animals, the model most commonly used is the planar spring-mass model, or the spring-loaded inverted pendulum (SLIP). This model is comprised of a point mass connected to a massless spring in series (Fig. 11). Raibert was among the first researchers to consider the SLIP model for hopping and developed theoretical models and prototype hopping robots [172] that inspired a plethora of one-legged robots [183] as well as further research into the SLIP model. To analytically study Raibert's SLIP hopper, Koditschek and Bühler [119] constrained the planar SLIP model to the vertical dimension and considered the task of maintaining a stable and recurring hopping height through actuation. They analyzed the model using both a linear and a nonlinear spring. Both models clearly demonstrated unique solutions for a stable state in which the domain of attraction is nearly every state. Interestingly, the nonlinear spring model also produced a period-two "limping" gate.

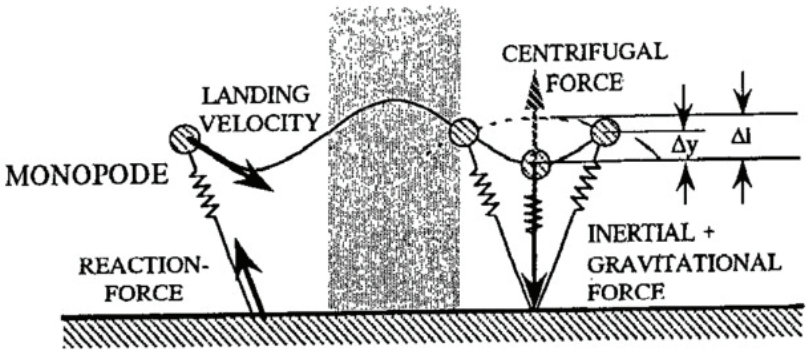

Figure 11: Illustration of the SLIP model [38]

Blickhan used a similar model to study dynamics of both hopping in place as well as hopping with forward motion [37]. He characterized hopping and running based on how measures such as step frequency, contact time, ground reaction forces, and specific power of such gates changed with forward speed. In hopping, the stride frequency remained constant and within a narrow band regardless of forward speed, whereas stride frequency during running gaits increased with increasing speed. Additionally, ground forces were greater during hopping than in running, and these ground forces increased with increasing velocity. The model showed that even with active forces, bouncing and running systems behave in a similar manner to a simple mass-spring arrangement.

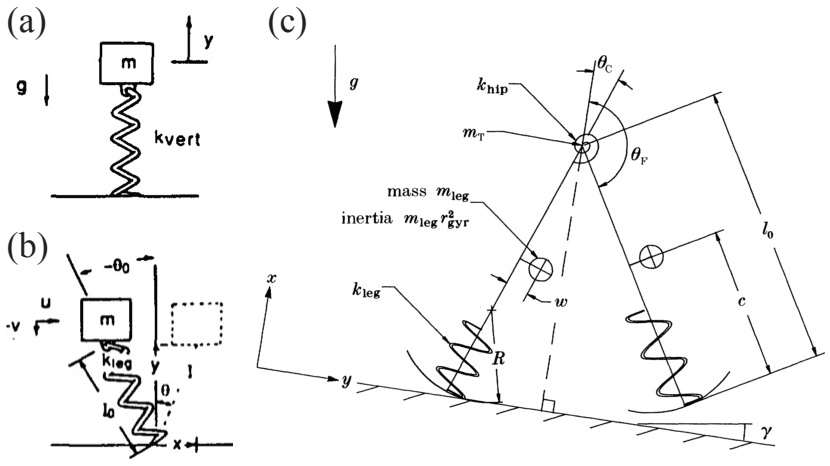

Figure 12: Theoretical hopping models. (a) SLIP as interpreted by McMahon and Cheng [144]. (b) Running biped [142]

McMahon and Cheng also presented a simple spring mass model of running and hopping in animals and made predictions of how stiffness coupled with speed, comparing their predictions with animal data [144]. In a different study, Cavagna et al. argued that, during running, elastic energy was stored during mid-step in stretched tendons [50]. With this principle in mind, a model consisting of a mass with a spring leg was presented (Fig. 12(a)) that bounced on the ground according the initial

conditions of the system and stiffness of the leg. Two versions of the model were considered, one in which the model hopped in place, and another in which the model was given a forward velocity. From these two models, two effective stiffnesses were calculated, the actual leg or spring stiffness, k_{leg}, and the vertical stiffness, k_{vert}, where k_{vert} was a fraction of the vertical component of the change in ground reaction force and the change vertical displacement. When hopping in place, both values were the same, while when hopping or running forward, the leg landed at an angle, θ_0, and $k_{vert} > k_{leg}$ for any finite θ_0 not equal to 0. The model was iteratively integrated to find the required k_{leg} to maintain a stable hopping gate. Given the parameters for initial forward and vertical velocity and θ_0, k_{leg} needed to create a gait in which final velocities and θ exiting the ground phase were identical to initial conditions. The parameter space was swept within values reasonable for animal comparison. When compared with animal data of dogs, a rhea and a human, assuming constant leg stiffness, the model accurately described how stride length and step length increased with speed in bipeds and quadrupeds.

A number of researchers have used and elaborated on the SLIP model to compare the one-legged SLIP model with multi-legged organisms. McGeer elaborated on the simple mass spring system for bipedal running by adapting the model with two legs (Fig. 12(b)), each with a mass and spring in series and a curved foot connected to the bottom end of the springs [142]. These legs were connected at a hip joint with a point mass and a torsional spring. Running was a passive mode in this model. Blickhan and Full compared the planar spring-mass monopode model to the dynamics of the hop, trot and running gates in a diverse cross-section of animals with varying numbers of legs [38], and found that the simple model provided a good approximation of those dynamics. Increasing pairs of legs acting simultaneously increased the whole body stiffness in the virtual monopode, increasing natural frequency and stride frequency.

Raibert considered the control algorithms for the one-legged SLIP model for generalizing to multi-legged systems [171]. Four-legged gaits that step with one foot at a time could use the single-leg SLIP algorithms for each leg. Gaits that use two feet simultaneously such as trots, paces, and bounds were represented with a virtual leg.

1.4.3 Maximal Jumping

This section discusses all non-hopping jumping models in which the goal of the jump is maximal height or distance. Many of the models focus on various types of athletic jumps performed by humans, and are all generally more complex than the SLIP model used for hopping. For example, Yeadon's model of the human body was considerably more complex than the telescoping SLIP model [218]. This model was used to explain the twisting and somersault moves in divers and trampolinist athletes. It comprised of 11 segments and 10 joints, requiring 66 equations of motion. Hatze presented another complex 2D human model to study long jumping composed of 17 segments controlled by 46 major muscle groups [92]. The control scheme for long-jumping was optimized in this study. A high jumping model [101] was also developed which, in this case, was actually fairly simple. The goal was to find the minimum kinetic energy requirement to clear a given height in which every point on the body clears the height. The model was a long rectangular rod (Fig. 13(a)), mimicking the size of a human body. The result of this study was an expression that described the height cleared by an object based on its initial conditions as well as its shape size and inertial parameters. They found that, for a given initial amount of energy, the maximum height cleared would be less for objects with larger moments of inertia.

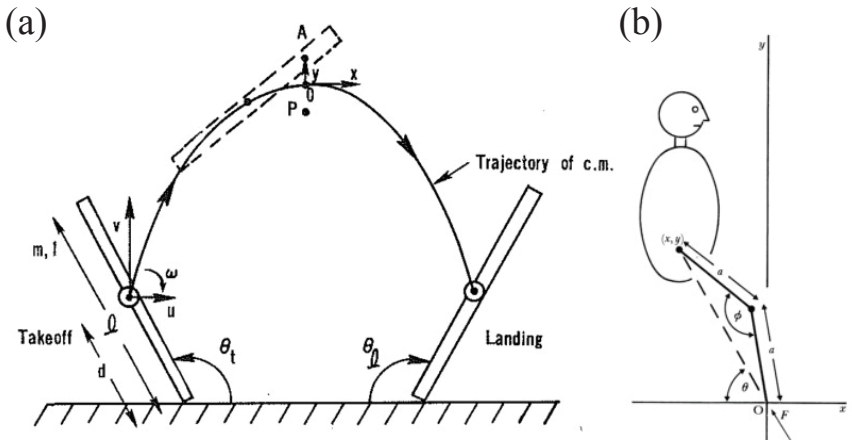

Figure 13: Theoretical high jumping models. (a) Hubbard and Trinkle [101]. (b) Alexander [14]

Alexander introduced a model of jumping that was used to study both long jumps and high jumps [14]. The model consisted of a rigid trunk connected to a two-segment leg that bends at the knee (Fig. 13(b)). He used Hill-type muscles [96] for actuation of extensor muscles that were in series with compliant tendons. With this model, he made predictions for the optimal movement methods for take-off to achieve both high jumps and long jumps: high jumpers must approach the jump with moderate speed and land the take-off foot at 45° to the horizontal, while long jumpers should approach their jump at the highest speed possible at a steeper angle. Seyfarth et al. expanded upon Alexander's model by incorporating a more realistic version of the muscle-tendon complex for the knee extensor muscle [187]. The muscle had in-series tendon compliance as well as compliance in parallel to the muscle actuation. The muscle also had the Hill-type force-velocity relationship in addition to eccentric forces, or forces due to lengthening contraction that work to decelerate a moving joint. The performance of the jump benefited from the enhancement of eccentric forcing, and was in agreement with experimental jumping performances.

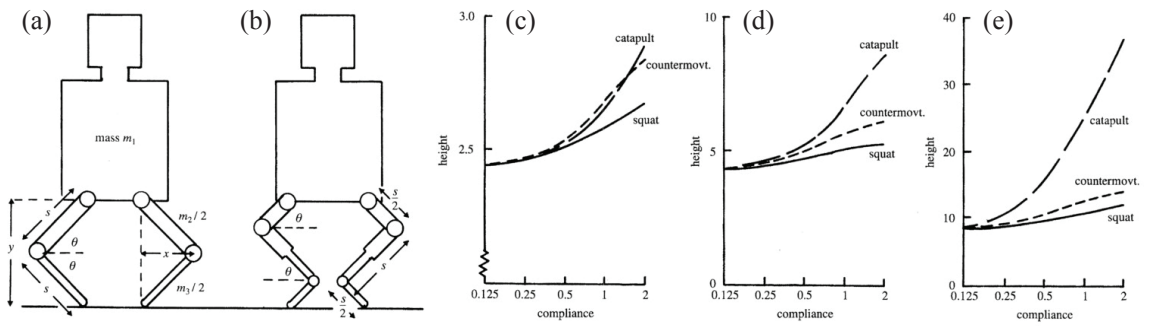

Figure 14: Theoretical model of standing bipedal jumps [8]. (a) Two-link model. (b) Three-link model. Comparison of different jump strategies with (c) human-like, (d) bushbaby-like and (e) insect-like isometric forces.

Alexander also developed a model to study the performance of various types of standing jumps [8]. In this relatively simple model, a main body mass was connected to two symmetric legs at the hips (Fig. 14(a,b)). Alexander considered both two-link and three-link legs. As in the high jumping model, Hill-type muscles were used with series compliant springs. The parameters chosen resembled values in animals ranging in size from locusts, to bush babies to humans. Parameters such as relative leg masses were also considered. Alexander varied parameters such as compliance and muscle-shortening speed as well as legs with 2 and 3 links. Chief among the results of this study was the comparison of the jumping performance using different jump strategies in animals that produce insect-like forces, bushbaby-like forces and human-like forces (Fig. 14(c-e)). Amongst all animals, the squat jump was the worst jump regardless of compliance value. For animals that produce insect-like forces, the catapult was the best overall jump. For human-like forces, the catapult and countermovement performed comparably. Animals that produce bushbaby like forces benefit the most from catapults, then countermovements. It has been suspected that the Senegal bushbaby performs a combination of catapult, countermovement and squat to produce its jump [1].

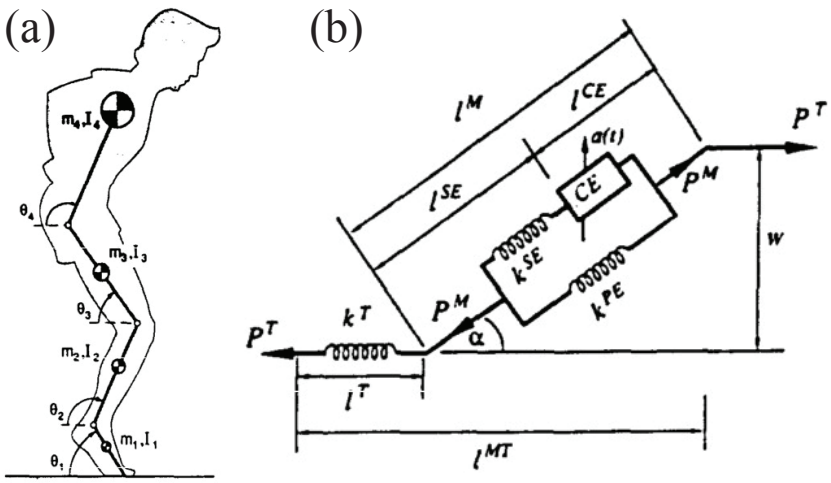

Figure 15: Maximum height jumping model [157]. (a) Schematic of 4-link jumping model. (b) Schematic of muscle-tendon complex model.

Pandy's model [157] for maximum height jumping is more realistic than Alexander's model. The model is planar, consisting of 4 articulated segments driven by 8 skeletal muscles modeled by Hill-type force laws with series and parallel elasticity and elastic tendons (Fig. 15). The purpose of this study was to use numerical methods to find an optimal control method for maximum height jumping. The optimal strategy discovered by the model was a countermovement. However, unlike in experimental human jumping results in which the countermovement was pronounced [158], the model's optimized countermovement nearly resembled squat jump, since the initial downward phase was subtle. Pandy and researchers hypothesized that this incongruence was a result of the model's inability to produce strong enough hip moments. A similar model was used by Soest *et al.* [205] to understand the role of the biarticularity of the gastrocnemius muscle (GAS) in maximum height jumping. Bobbert used this model to understand how the elasticity of series elastic elements (SEEs) in the triceps surae affected the performance of maximum height jumping [41]. He found that longer more compliant tendons allowed for greater power output and thus greater jump height.

1.5 Impulsive interaction with granular media

1.5.1 Introduction

Jumping models have been primarily developed with an assumption or objective of hard ground jumping. However, many situations [127, 149] exist where animals perform fast locomotion in more complex substrates like dry granular media, mud, soil and leaf litter. Performance is typically reduced in sand as compared to hard substrates. Toads, for example, achieve greater jump distances on a grassy lawn (300 to 575 mm) than on sand (150 - 375 mm) [174]. The yielding properties of sand produce a dissipative effect during maximal human jumps; on average, volleyball players achieved 64% of hard ground jump heights while utilizing more energy [151]. This damping effect is beneficial for plyometric training on sand to improve jumping and sprinting performance with less muscle soreness than athletes that trained on grass [105]; training on sand was superior to training on grass in improving the countermovement jump.

While many jumping robots have been designed and tested for hard ground, a minimalist hopper by Burdick and Fiorini [48] with a six-bar geared spring as well as self-righting and steering capabilities was designed with a focus on robustness during celestial exploration (where sandy environments are common). Furthermore, the ability of sand and other soft substrates to yield has been considered in the design of a jumping robot that can simultaneously roll and jump [20], where the design of the robot's outer surface reduced contact pressure with the ground such that the robot would be enabled to travel over yielding substrates without significantly sinking or getting stuck. However, a systematic analysis of the performance and dynamics of robotic interaction with granular media during impulsive actuations such as jumping had not been considered. And since such substrates are commonly found in a wide variety of environments, understanding the dynamic interactions in these situations is also robotically relevant for applications such as search and rescue operations [46, 224]

or the exploration of planets and other celestial bodies [49].

Aside from being a ubiquitous substrate commonly found on beaches, deserts and celestial bodies, dry granular media stands out among complex substrates as an excellent system to illustrate the challenge of analyzing complex environments. Dry granular media displays a rich variety of behaviors in response to forcing and occur in environments (deserts, dry regions of beaches) and regimes (small inertial number, see discussion in [18]) encountered by robots. Such properties (especially homogeneity and lack of moisture) allow for precise experimental controllability of granular states. However, granular media (ubiquitous and studied though it may be) is not fully understood. No fundamentally derived theoretical models (like Navier Stokes in fluids) exist and thus cannot be solved analytically or in computer simulation (although progress has been made to this end with the use of plasticity theory [21], discussed more in Section 1.5.3). Thus, a robophysical approach becomes essential when trying to understand robotic movement in such environments, whereby easily controllable robots behave as "physical simulations" of locomotion, and complementary theoretical models and simulations are used for further insight.

While no Navier Stokes-like theory yet exists for granular media, simplified models (sometimes empirical) of granular forces describing bulk behavior have been utilized. Further, such materials are relatively simple to model computationally at the grain level: they can be described as an ensemble of individual particles whose emergent interactions are dominated by repulsive dissipative contact forces. Thus, while underlying principles of granular interaction may be difficult to intuit from individual particle iterations, modeling such interactions can nonetheless be performed with computer simulations which need only account for colliding spheres. In fact, such numerical simulation of individual grain particles, known as discrete element method (DEM), is a common solution when fundamental continuum models are unavailable.

Here we provide a brief overview of DEM. We then provide an overview of continuum models and bulk force models that have proven useful for the analysis of robotic interactions with granular media.

1.5.2 Modeling granular media: DEM

Discrete element method (DEM) computer simulations model granular media as multiple particles interacting under Newton's laws and collisional forces. DEM is simple to implement for small numbers of spherical particles. However efficient simulation of granular media is not trivial, particularly in modeling grain-grain contacts. A common method for modeling contacts in hard ground simulations is to formulate the contact process into a linear/nonlinear complementarity problem (LCP/NCP). During collision, non-penetration constraints are imposed [131, 138, 148] and integrated into the Newton-Euler equations of motion together with other bilateral constraints (e.g., from joints). In the absence of friction, the equations can be linear in either acceleration [27, 159] or velocity [19, 189, 190] (with proper discretization in time). Unknown constraint forces/impulses (from contacts of joints) can then be determined from optimization techniques (e.g., successive over relaxation, gradient descent). Frictional (Coulomb-like) forces introduce nonlinear constraints into the system. To re-cast as a linear complementarity problem, these forces can be discretized.

However, for large scale problems like dense granular flow with millions of particles, using the LCP formulation as is done for hard ground becomes untenable. The LCP iterative solver is of order N^2 in time (where N is the number of contacts and is proportional to the number of grains in the system) for each iteration. Furthermore, the solver needs to be called at every time step to resolve the collisions. In contrast, DEM uses compliant particles (the "regularization method" [82]) instead. Combined with a grid partition scheme for collision detection, the time scaling can be reduced to order N for many practical problems.

The accuracy of DEM for dense granular flow is well established and reliable [165, 176], provided collision force parameters (typically more than two but fewer than 6) are tuned correctly and the time step is small enough. These parameters (restitution, friction coefficients,etc.) can be empirically tuned such that simulated forces on intruders moving in a granular medium (e.g., a rod dragged horizontally) match experimental measurements [134, 62]. DEM allows one to obtain information such as forces and flow fields of the granular media that are difficult to measure in experiment. Particularly when coupled with a multi-body dynamic simulator, DEM has been useful in describing body-media interactions during locomotion, facilitating parameter variation and the development of locomotor principles [135, 170, 224].

To demonstrate the efficacy of this approach, we briefly discuss the work of our group (Goldman Lab [134, 135]) coupling DEM to a multibody solver, Working Model 2D, to simulate both the subsurface locomotion of an undulatory robot and the animal (sandfish) that inspired the design of the robot. The simulation has two phases at each time step. In the first phase, DEM computes the interaction forces between the robot body and every particle it contacts; the state (position, velocity, orientation) of the particles are also integrated using the contact forces. In the next phase, the multibody solver updates the state of the robot, based on the constraints, controls and the accumulated interaction forces. When the contact model parameters are calibrated against physical experiments (impact and drag in the specific granular media), the combined DEM-Multibody approach was able to accurately predict the undulation efficiency of the robot for all undulation frequencies ($1-4$ Hz) and all wave amplitudes tested. The sandfish simulation also matched the animal experiment and indicated that the sandfish targets an optimal undulation strategy that maximizes its speed.

Qian et al. [170] used DEM coupled with MBDyn [79] (a 3D multibody simulator) to investigate how a lightweight robot, the DynaRoACH [99], could achieve

high locomotion performance on granular media. The DynaRoACH's speed in both laboratory experiments and DEM simulation agreed well, and exhibited a transition in locomotor mode from walking at low frequencies to running at high frequencies (Fig. 16c). Measuring ground reaction forces in simulation (which were impossible to measure in the experiment), Qian et al. found that low frequency walking where the robot used the quasistatic "rotary walking" mode [169, 128], relied on the penetration depth-dependent hydrostatic-like forces. In contrast, high frequency gaits induced speed-dependent hydrodynamic-like forces resulting from inertial drag, allowing the robot to achieve rapid running on the leg-fluidized substrate. Zhang et al. [224] also demonstrated the capabilities of DEM simulation for parameter variation by varying the coefficients of particle particle friction, particle leg friction, and leg width over a wide range, and tested the effects of these parameters on robot locomotion performance. The particle friction parameters are difficult to vary continuously and independently of other parameters in experiment.

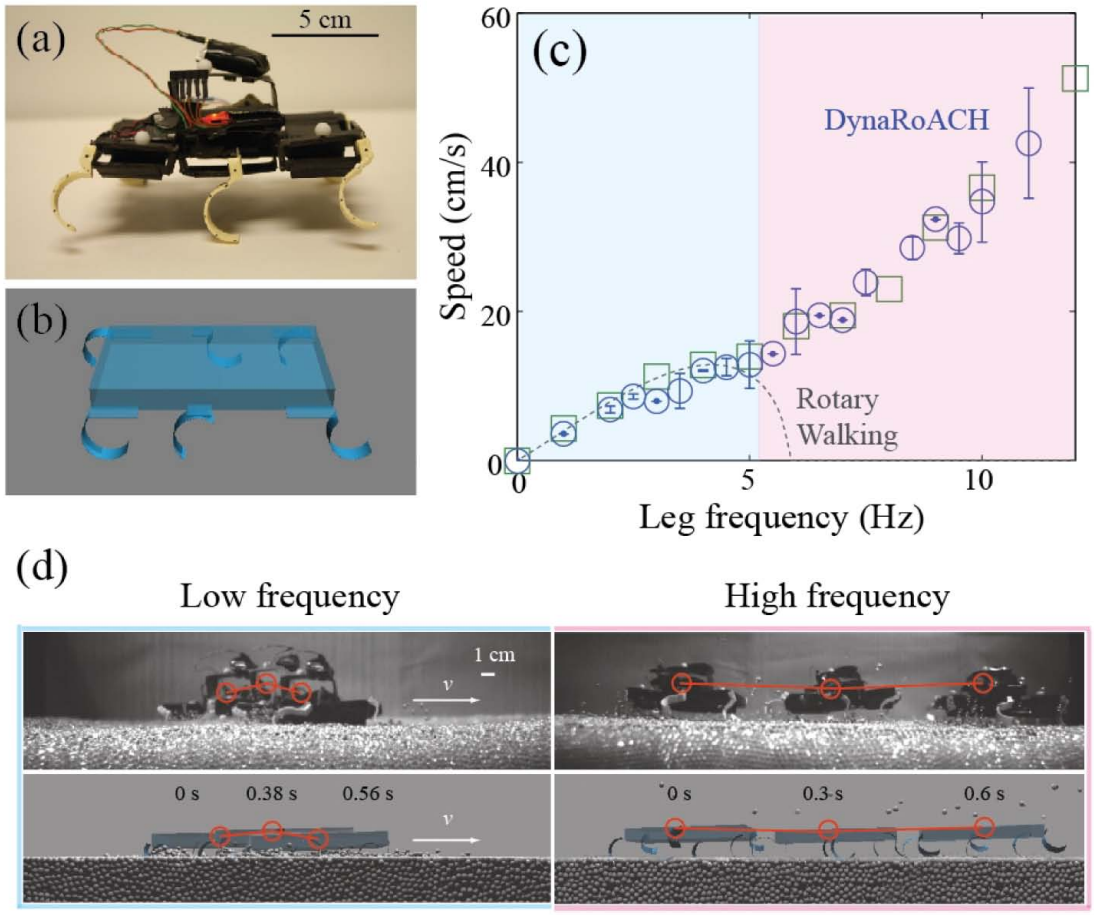

Figure 16: A small, lightweight robot (DynaRoACH, 10 cm, 25 g), with size comparable to fast-running animals, can use two distinct propulsion mechanisms for effective locomotion on granular media: a low frequency walking mode (shaded light blue in (c)) and a high frequency running mode (shaded pink). (a) The lightweight, hexapedal DynaRoACH robot. (b) The simulated DynaRoACH robot in MBDyn [79]. (c) Average robot CoM forward speed vs. leg frequency. Blue circles represent experimental data and green circles represent simulation data. Grey dashed curve represents rotary walking model prediction derived using a heavier robot (SandBot, 30 cm, 2500 g). (d) Time sequences of the two locomotion modes observed for DynaRoACH moving on 3 mm glass particles. Adapted from [170].

The future of direct granular simulations looks promising; the cone complementarity problem (CCP) formulation proposed by Tasora [196] (which is also being used in Chrono::Engine) uses a matrix-free iterative solver with time proportional to N for each iteration. Compared with the DEM method, where the time step needs to be much smaller (due to grain stiffness), the non-smooth dynamic (complementarity) approach can potentially use larger time steps and remain stable. However, CCP remains under development, and substantial validation and application and results have not yet appeared.

1.5.3 Modeling granular media: Force models and continuum descriptions

While DEM simulations are effective at simulating granular kinematics during locomotor interaction, to gain an intuitive understanding, it is useful to analyze bulk dynamic responses to locomotor intrusions. Yet, even in this well-studied system, little is known about such dynamics, particularly during active impulsive interactions such as those that occur during jumping. In the generalized 3D case, continuum equations for granular media in the so-called "rapid flow regime" in which particles do not experience enduring contacts (i.e., the system does not exist in solid-like states) have a long history [109] and have shown predictive power in shock formation in complex 3D systems [43]. However, their efficacy has not been tested in situations relevant to locomotion, in which solid-like and fluid-like states coexist.

Thus, during such high speed locomotor interactions with granular media, which can induce complex inertial reaction forces from the substrate[114, 203, 198], direct particle simulation has often been the solution of choice. However, in the simplified 1D intrusion case, many studies of fixed-shape (non-locomoting) objects impacting and penetrating dry granular media have revealed reaction forces (F_{GM}) on the objects that can be described by

$$F_{GM} = F_p(z) + \alpha v^2, \tag{1}$$

where v and z are the object's velocity and depth, respectively [114, 199, 203]. The hydrodynamic-like term, αv^2, results from momentum transfer to the grains (significant during high speed impact[69, 164, 180, 26, 15, 73]), where α is the inertial drag coefficient. This inertial drag term has its origins in the study of ballistics that date back to the time of Euler [69] and Robins [180], where they sought to understand the principles of drag on ballistics through various media, homogeneous granular media included. They described the resistance to penetration as a constant value independent of speed to produce a negative acceleration: $-dv/dt = \gamma$, where γ is constant. Though suggested by Euler, credit has typically been granted to Poncelet who later described such drag as the summation of γ and αv^2, where α is constant. Allen et al.[15] performed experiments of ballistic impact in sand at speeds greater than the sand's speed of sound and discovered that one could fit data with a more generalized form, $-dv/dt = \alpha v^2 + \beta v + \gamma$, or a form that follows $-dv/dt = \beta v^2 + \gamma$ for low speeds or $-dv/dt = \alpha v^2$ (where $\alpha < \beta$) for speeds greater than a speed (about 100 m/s) associated with the sand's speed of sound.

The dynamics of lower speed impacts (much less than the granular speed of sound) have been of more recent interest to the granular physics community with respect to the mechanics and energetics of impact cratering [202, 152, 54, 212, 58, 199]. Ciamarra et al. performed 2D impact experiments as well as DEM simulations of the impact cratering events of a disk and revealed that an impact event's kinematics can be qualitatively divided into the initial impact phase, the penetration phase, and the collapse phase where the crater fills in. For the majority of the trajectory, they observed a constant drag force that was proportional to the impact velocity. During such impact events one must consider also the hydrostatic-like force $F_p(z)$, which results from gravitational pressure and grain-grain Coulomb frictional forces. $F_p(z)$ is typically considered to scale as kz for submerged or flat intruders[199] for slow intrusions, where k characterizes the medium's penetration resistance, although it has

been described as constant [58] as well as in exponential form [17] for shallow spherical impacts. Katsuragi and Durian [114] combined this hydrostatic term with the inertial term, αv^2, by experimentally measuring projectile dynamics for low speed impacts and determining that forces can be described as Equation 1. However, Umbanhowar and Goldman [203] experimentally examined the dynamics of granular spherical impact at various volume fractions, ϕ, and found that the inertial drag coefficient, α, was independent of intrusion depth only at the critical packing state, ϕ_c. Volume fraction, ϕ, which approximately ranges from 0.55 to 0.64 [110] is the ratio of the collective volume of individual grains vs the volume the grains occupy in bulk. The qualitative behavior of granular media under shear is determined by ϕ, whereby, at low values, the granular substrate tends to consolidate under shear and reach a higher volume fraction, and high values causes a dilation effect under shear and reduces ϕ. The ϕ that remains constant and neither dilates nor consolidates is the critical volume fraction , ϕ_c [185]. This value can be determined in various substrates by measuring the change in volume after impact events [203, 83], whereby the volume change at ϕ_c is 0 (the volume change is negative a low ϕ and positive at high ϕ).

While inertial drag must be considered to describe the dynamics of low speed impacts, the Goldman group has discovered that, in many relevant granular locomotion scenarios that are relatively slow (low inertial number [166, 74, 18]), we can forego both DEM (surprisingly avoiding many of the challenges of hard ground and fluid modeling) and the consideration of inertial drag. Over the past few years, Daniel Goldman's group has developed a granular resistive force theory (RFT) to describe thrust and drag forces on an intruder moving within granular media, which is essentially an extension of the hydrostatic-like term, $F_p(z)$, beyond 1D forces and intrusion directions. Such work has helped explain the kinematics of slow moving locomotors[129, 135, 133]. This approach was inspired by the early theoretical modeling of swimming of microorganisms in fluids. In the presence of complex moving

boundaries, full Navier-Stokes equations for complex flows often could not be solved (without CFD). Instead, pioneers made simpler approximations in viscous fluids. The best known of these, called Resistive Force Theory (RFT) [85], assumes that the deforming body can be partitioned into segments, each experiencing drag, and that the flow/force fields from these segments are hydrodynamically decoupled and do not influence the fields of other segments. Therefore, the normal and tangential forces on a small element depend only on the local properties, namely, the length of the element ds, the velocity $\mathbf{v}$ and the orientation $\hat{\mathbf{t}}$ (the fluid is homogeneous so position dependence is dropped). The net force on the swimmer is then computed from the integral

$$\mathbf{F} = \int (d\mathbf{F}_{\perp} + d\mathbf{F}_{\parallel}) = \int ds(f_{\perp}(\mathbf{v}, \hat{\mathbf{t}})\hat{\mathbf{n}} + f_{\parallel}(\mathbf{v}, \hat{\mathbf{t}})\hat{\mathbf{t}}), \tag{2}$$

where the functional forms of $f_{\perp}$ and $f_{\parallel}$ can in principle be determined from the Stokes equations. The characteristics of $f_{\perp}$ and $f_{\parallel}$ are different between viscous fluids and granular media. For low speed motion in fluids, RFT forces are velocity dependent both in direction and magnitude, whereas forces in granular media are independent of the velocity magnitude. Additionally, unlike in fluids, grain-grain friction and gravity lead to a depth dependence in granular RFT forces.

To determine fluid RFT forces, experiments are often needed, because analytical solutions to the Stokes equations cannot be easily obtained even in simple cases (e.g., a finite length cylinder moving in the axial direction). Similarly in granular media, where there is no constitutive law, $f_{\perp}$ and $f_{\parallel}$ has primarily been determined from experiment or DEM simulation. Most recently in a study by Askari and Kamrin [21], however, a friction-based continuum model known as plasticity theory has been shown to reproduce experimental granular RFT measurements when simulated with FEA techniques. Moreover, the study was able to analytically uncover how, even though RFT was originally developed to simplify the analysis of viscous fluid interactions, the superposition of RFT forces is more predictive in granular media than in fluids.

Through the analysis of granular RFT, they have a developed an analytical criterion that determines which types of substrates will observe the assumptions necessary for RFT (chief among them the ability to perform a linearly independent superposition of resistive forces acting on different surface elements of an intruder). Through the use of this criterion, they have discovered that certain cohesive media such as gels, pastes and muds comprise a new class of RFT-analyzable substances.

RFT has exhibited predictive power for legged locomotion on granular media in the quasistatic locomotor regime [129, 133] (Fig. 17). Using a small RHex type robot, Xplorer, the forces on the foot during slow walking modes have been found to be reproducible with the continuum equations of RFT [223]. RFT was also extensively used to investigate various aspects of sand swimming in both artifical [135] and biological [64, 63] locomotors. For example, granular RFT was used to model how neuromechanical phase lag (NPL) (a phenomenon observed in many undulatory animals during which the wave of muscle activation progresses faster than the wave of body bending [188]) emerges. Ding et al. [63] used RFT to explain the source of NPL during sand swimming in the frictional (non-inertial) regime. The timing of torque onset (which corresponds to muscle activation), computed from RFT, agreed well with experimentally observed electromyography signals in a sandfish lizard, indicating that NPL may depend strongly on details of the environmental interactions.

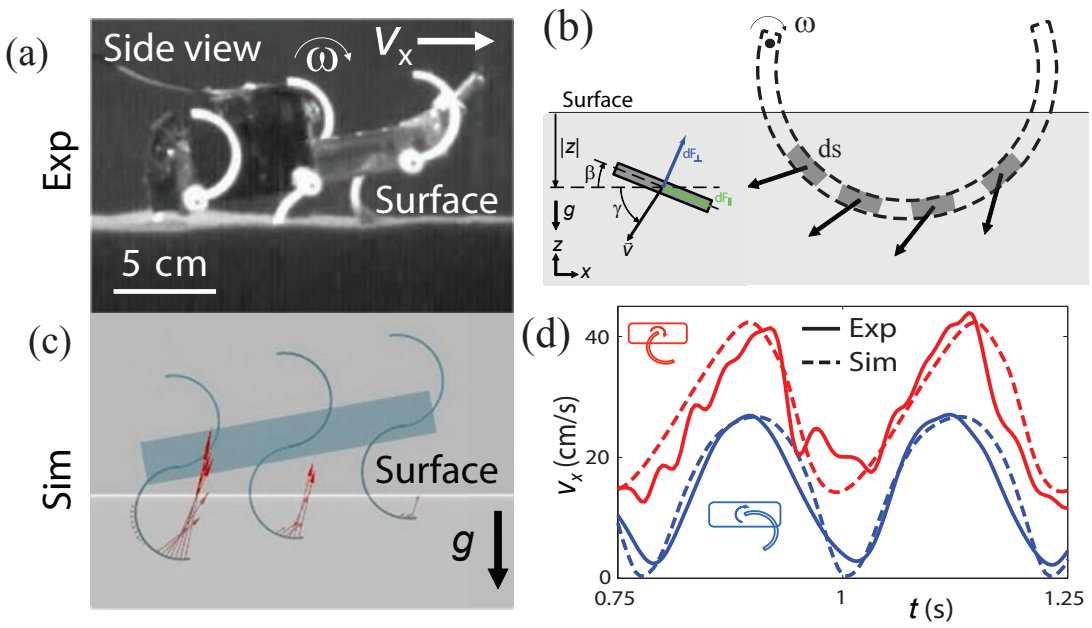

Figure 17: Resistive Force Theory applied to legged locomotion on dry granular media. (a) RHex-like robot (Xplorer) robot during alternating tripod gait locomotion. (b) Illustration of the basic idea behind Resistive Force Theory (RFT) for movement of a RHex c-leg into granular media. Each infinitesimal element ds on the intruding leg is characterized by its tangent direction $\hat{\mathbf{t}}$ (or normal direction $\hat{\mathbf{n}}$) and its velocity $\mathbf{v}$; each element experiences a force $d\mathbf{F}_{\perp,\parallel}$. In true fluids, these forces can be described by Stokes law, while for granular media, they are measured in experiment. (c) Simulation of Xplorer locomotion using RFT. Red arrows indicate granular reaction forces at each segment. (d) Comparison of forward speed vs time between an experimental robot and corresponding RFT simulation using c-legs and reversed c-legs. Adapted from [129] (Note: Forces were measured in $d\mathbf{F}_{z,x}$instead of $d\mathbf{F}_{\perp,\parallel}$ as shown in (b))

However, during fast locomotion, RFT alone is an insufficient descriptor of locomotion dynamics in granular media; such a granular model does not account for grain-based inertia effects. For example, the performance of the DynaRoACH's high

speed gaits [170] deviated from the rotary walking model, which, similar to RFT, assumes quasistatic interactions. This deviation implies that hydrodynamic-like granular inertial effects contributed significantly to the reaction force, making quasistatic continuum equations like RFT ineffective. Recent studies of free impact in dense cornstarch solutions [211] and dry granular media [115] as well as rapid lightweight robot running on granular media [224] have shown the importance of hydrodynamic-like effects during high-speed interactions. One such effect includes added mass, which effectively increases the inertia of an intruder displacing material (see [45] for a review of added mass in fluids). Added mass can contribute to a shear-thickening response in dense suspensions [211]. In the realm of actively forced impacts, added mass effects contribute to the impulse developed during the slap phase of a basilisk lizard running on water[80]. In fact, the term in Equation 1 defining inertial drag during granular impact, αv^2, is derived from what was considered a classical aerodynamics equation for penetration forces [81], $-mdv/dt = \frac{1}{2}CA\rho v^2$, where m is the projectile's mass, A is the projected surface area, ρ was fluid density and C is a scaling constant. Poncelet attributed this term to the momentum change associated with colliding inelastically with a virtual mass [164], which accumulates when the impactor accelerates surrounding material, $\frac{d(m_a v)}{dt} = \frac{dm_a}{dt}v + m_a a$. Added mass for an intruder impacting a fluid has been approximated by the hemispherical volume of liquid accelerated forward in front of the intruder, consistent with the velocity change imparted by an inelastic collision with a mass equal to the added mass[177, 210].

Insight into high speed granular locomotion will improve by extending this reactive forces, or dynamic RFT, for 3D motion. This will require a careful study of granular kinematics and dynamics during a variety of high speed locomotor interactions. We posit that it may be possible to integrate such theory with the continuum methods treating fast deforming granular media as a dense gas [109], perhaps using methods like those developed in [113], which focus on steady flow. Additionally recent work by

Askari and Kamrin [21] suggests that a continuum model based on plasticity theory, which has shown effectiveness in explaining quasistatic RFT forces in granular media, may be of use at the high speeds observed during robotic jumping.

CHAPTER II

HARD GROUND JUMPING DYNAMICS

2.1 Summary

Jumping is an important behavior for many animals and robots. Unlike periodic gaits such as hopping or running, whereby energy generated in previous cycles can be leveraged to efficiently sustain motion, jumping relies almost purely on a transient burst of activity to produce take-off from rest. While bioinspired robots have utilized some jumping mechanisms revealed from numerous biological studies, there have been few systematic studies of the dynamics of these transient behaviors. We performed a study which characterized the dependence of jumping performance on the robot's hybrid dynamics [3].

In this Chapter, we discuss the results and analysis of these jumping experiments [3] as well as other experiments which probed the role of vibrational resonance in producing lift-off. Further, we expand on this work by examining - primarily through simulation - how various nondimensional parameters pertaining to the inertially forced spring-mass model influence the relative performance and optimal frequency of different jumps. Through simplifications and an analysis of the stutter jump's kinematics, we also develop predictive formulas for the optimal frequency of the stutter jump based on a small number of system parameters. Interestingly, we can make predictions of how jumping performance changes based on gravity, useful for robotic applications during the exploration of celestial objects.

2.2 Methods

2.2.1 Automated Robotic Jumping Apparatus

Hard ground jumping experiments were conducted with a robot consisting of a linear actuator (Dunkermotoren ServoTube STA11) (Fig. 18(c)) with a series spring rigidly attached to the bottom end of the actuator's lightweight thrust rod. The ServoTube STA11 provides a force proportional to the current delivered. Similar to rotational electric motors, the linear motor has a stator and a rotor, except in the linear motor configuration, the stator and rotor is unrolled to produce a linear force instead of a torque. In the STA11, the thrust rod acts as the stator, encasing rare-earth magnets, and the exterior case constitutes the rotor that receives current to produce an electromagnetic force on the rod. Encoders allow for feedback control of the rotor's position relative to the thrust rod.

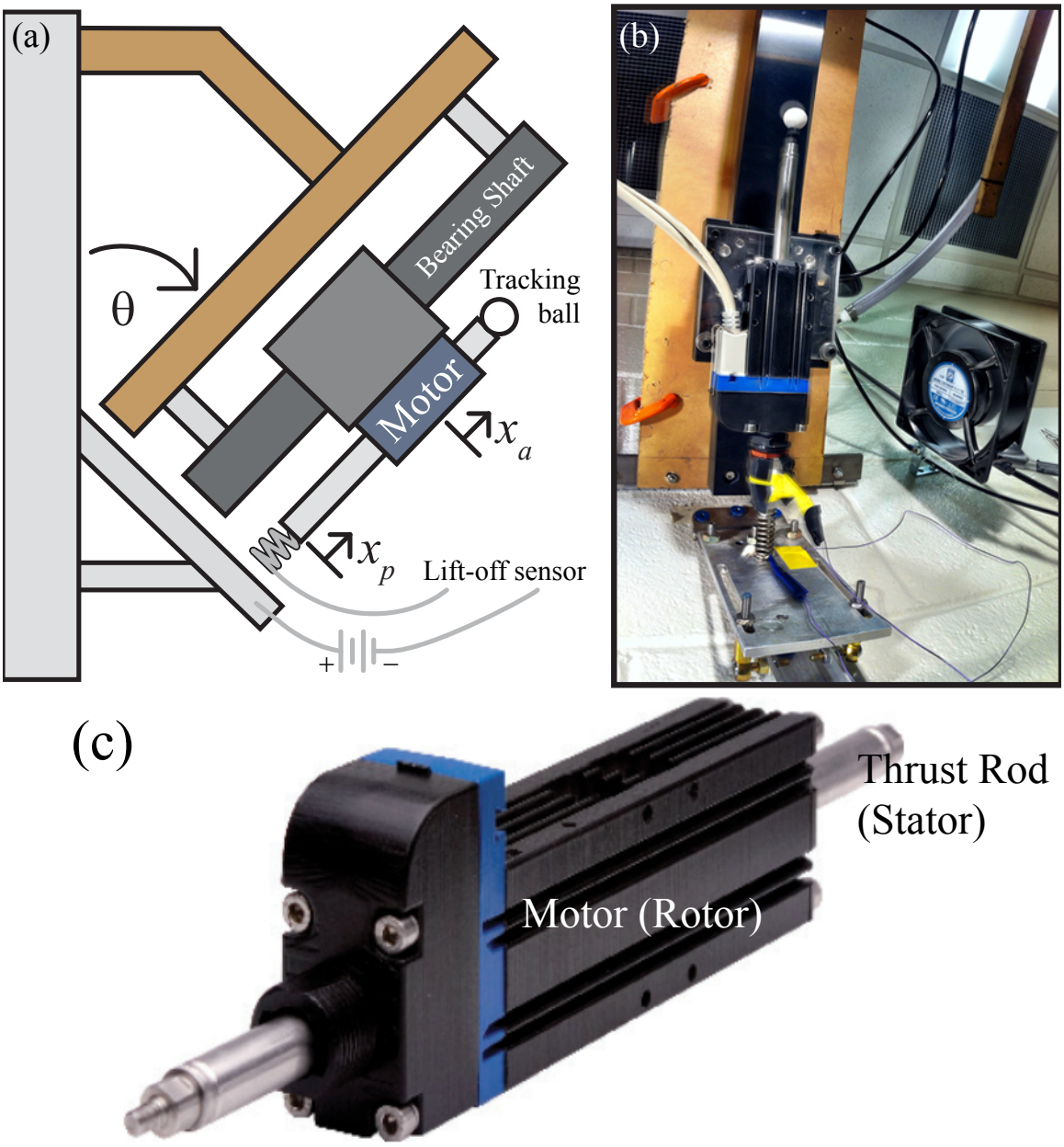

Figure 18: The hard ground robot apparatus. (a) Diagram of robotic apparatus, robot was oriented to $\theta = 75°$ to reduce motor strain from force of gravity. (b) Picture of robot setup. (c) Close up of the Dunkermotoren ServoTube STA11 motor, image courtesy of Dunkermotoren.

The actuator is mounted to an air bearing for nearly frictionless 1D motion (Fig. 18(a,b)). The air bearing carriage adds significant weight to the robot. To mitigate

overheating in the motor, the bearing is oriented to 75° relative to the vertical axis, reducing gravity to $0.276g$. We control the motor position with a feedback/feed forward control scheme (Fig. 19(a-c)). Reducing the value of the position feedback gain to 6% of the value for optimal control damps the entire system. This allows for faster automation of experiments by eliminating spring vibrations after a jumping experiment. Most gain values supplied are sufficient to control the motor trajectory with the exception of the position proportional gain, which is tuned manually. Figure 19(c) illustrates the commanded versus actual positions as collected from the amplifier for a relevant range of forcing frequencies while the robot is suspended.

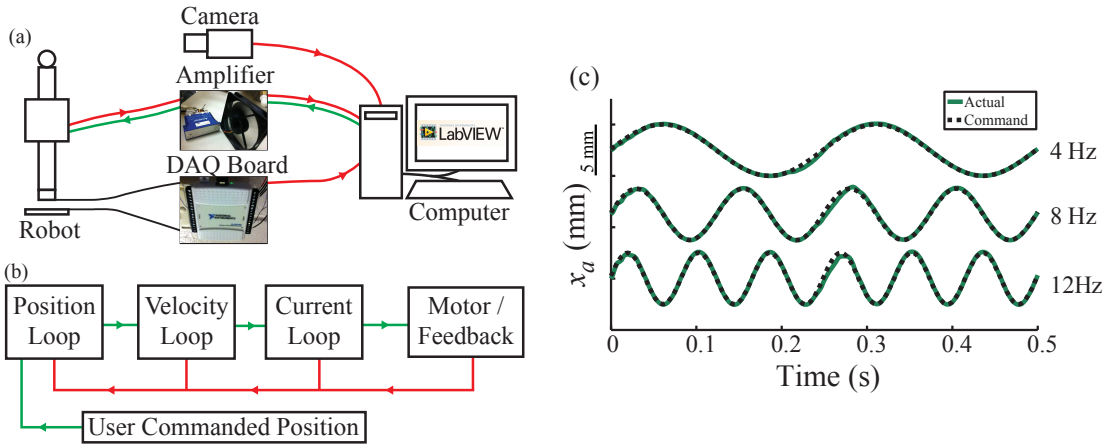

Figure 19: Motor Control and Data Acquisition. (a) Schematic of data communication to and from computer. Labview logo courtesy of National Instruments. (b) High level block diagram of feedback motor control loop. (c) Commanded vs. actual relative actuator position x_a as measured from encoders. The motor was controllable for a wide range of forcing frequencies.

To detect lift-off, we attached a continuity sensor to the bottom end of the spring (Fig. 18(a)). The sensor consists of a wire coiled around the bottom of the spring and wire connected the metal base that the robot jumped on. These wires are connected to a USB DAQ board (National Instruments NI-USB-6009) that supplies a 2.5 V load and measures the voltage of the circuit. When the spring leaves the ground and disconnects from the metal base, the resulting open circuit causes a change in voltage. The sensor operates at 1000 Hz, allowing the detection of metrics such as

time to lift-off from the onset of motor activation and time of flight to 1 millisecond resolution.

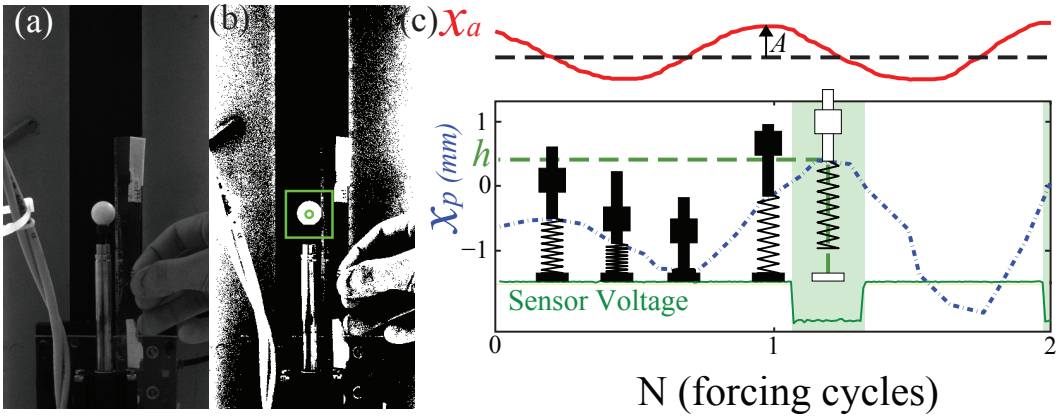

Figure 20: Data collection. (a) Raw image take for video tracking. (b) Sample threshold image. Green rectangle indicates initial tracking window; green circle indicates white space centroid location. (c) Actuator position x_a and video tracked position of the thrust rod x_p, and the lift-off sensor voltage with a sinusoidal forcing amplitude of $A = 0.30$ mm in which the robot lifts off.

Time of flight was used to measure jump height (Fig. 21), derived from the equations of projectile trajectory. Vertical position vs. time, $x(t)$, of an airborne object is $x(t) = x_0 + \dot{x}_0 t + \frac{1}{2}at^2$, where the initial position is $x_0 = 0$, and the acceleration, a, is gravity, $-g$. The velocity of the object at maximum height, which occurs at time, t_h, is $\dot{x}(t_h) = \dot{x}_0 - gt_h = 0$. Thus, the initial velocity, $\dot{x}_0 = gt_h$, can be substituted into the position equation, which is at maximum height at time, t_h, $x(t_h) = h = gt_h^2 - \frac{1}{2}gt_h^2$. Since the time at maximum height, t_h, is half of the total flight time, t_f, the equation of jump height can be expressed as $h = \frac{1}{8}gt_f^2$. A Labview routine automated data collection and robotic control for multiple successive jumping experiments, whereby jumping metrics such as time of flight or time to lift off were measured for systematically varied actuation parameters.

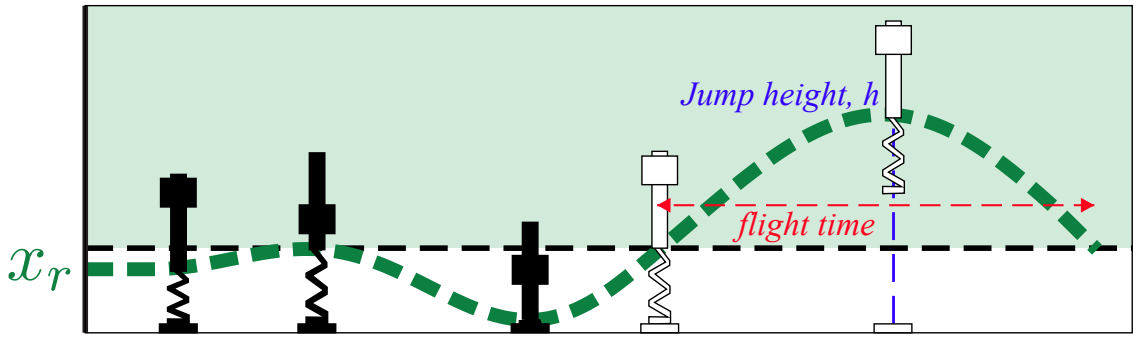

Figure 21: Illustration of the measurement for jumping height using flight time.

While the continuity sensor was used to measure jump height for the hard ground experiments, a 200 FPS Point Gray camera was additionally used for real-time tracking of a 15 mm diameter white plastic ball attached to the thrust rod (Fig. 20(a,b)). Video tracking of the robot became essential during jumping experiments on granular media (see Chapter III), where the continuity sensor could not be used. A threshold-based tracking routine in Labview calculated the centroid pixel position of the ball. Oscillations smaller than 30 microns were detectable. An example of the coordination of video-tracking, lift-off sensing, and motor control is illustrated in Figure 20(c).

Video tracking was also used to characterize the damping of the spring (Fig. 22). From rest, with the relative motor position remaining constant, the robot was excited by a tap while on the ground, and the high-speed camera captured the resulting spring vibrations. Camera tracking was also used to determine the coefficient of restitution (0.8 ± 0.06) from ground collisions.

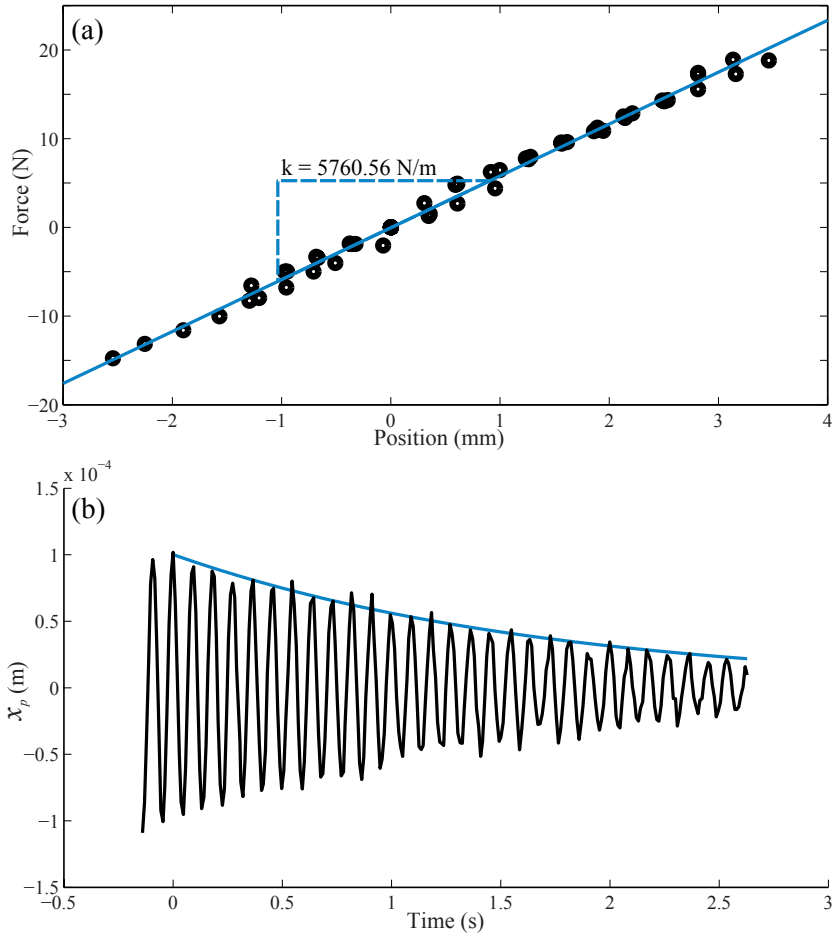

Figure 22: Measuring spring stiffness and damping. (a) Force vs. position data of spring compression (black circles). Stiffness was found to be $k = 5760.6$ N/m (linear fit in light blue). (b) Thrust rod position, x_p, during free spring oscillations vs. time (black). Position re-centered about zero to determine decay equation of oscillation peaks (light blue, $x_{p,peaks} = 0.00015e^{-\zeta\omega_0 t}$), where $\omega_0 = \sqrt{k/m}$, and damping ratio $\zeta = 0.0083$.

We found the damping ratio to be $\zeta = 0.0083$ by determining the exponential decay of the oscillation peaks. The natural frequency, $\omega_0 = \sqrt{k/m}$ or $f_0 = \frac{\sqrt{k/m}}{2\pi}$, was determined by the overall mass, $m = 1.178$ kg, and the spring stiffness, $k = 5760.6$ N/m, which was determined from force vs. displacement measurements taken by

compressing the spring with 6-axis robot arm fitted with a force sensor.

2.2.2 Simulated Jumping Model

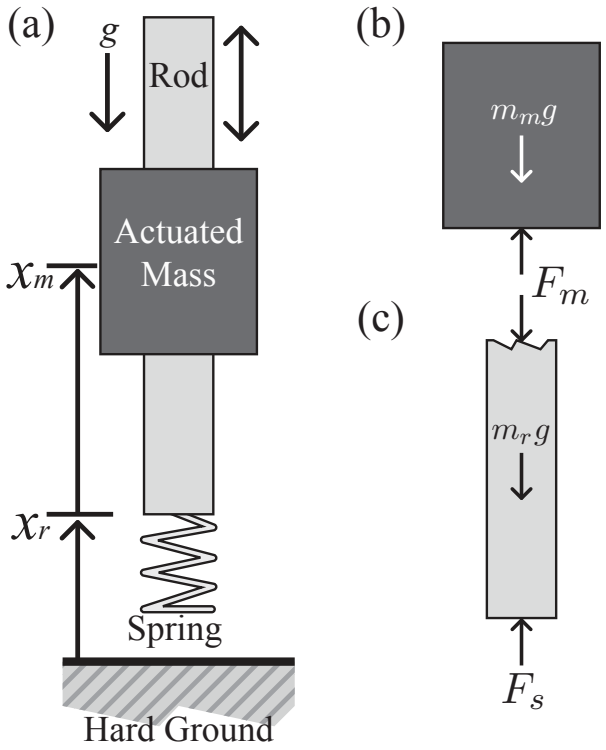

Figure 23: Diagram of the theoretical model on hard ground. (a) Overall hard ground model. Free body diagrams of the (b) actuated mass and (c) rod.

To compare with experiment and further analyze the model, we numerically integrated a Simulink (Matlab, ODE45 integrator) model of the robot (comprised of a linear motor and thrust rod) in series with a spring jumping on hard ground according to the following equations of motion:

$$m_m \ddot{x}_m = -m_m g + F_m, \tag{3}$$

$$m_r \ddot{x}_r = -m_r g - F_m + F_s, \tag{4}$$

the subscripts, m and r corresponding to motor and rod quantities, respectively. The rod and motor equations were combined as

$$M \ddot{x}_r = -Mg + F_s + m_m \ddot{X}_m, \tag{5}$$

Table 3: Empirically Measured Robot Properties

Property	**Units**	**Value**
Total Mass, m	kg	1.178
Motor Mass, m_m	kg	1.003
Rod Mass, m_r	kg	0.175
Stiffness, k	N/m	5760.6
Damping Ratio, ζ	-	0.0083
Damping Coefficient, c	Ns/m	1.368
Natural Frequency, f_0	Hz	11.130
Resonant Frequency, f_r	Hz	11.129

where $M = m_m + m_r$, and the $\ddot{X}_m = \ddot{x}_r - \ddot{x}_m$. The spring force, F_s, followed Hooke's law for the spring between the rod and foot: $F_s = -kx_r - c\dot{x}_r$, where the damping coefficient, $c = 2\zeta\sqrt{km}$. Table 3 shows the parameter values used when making direct comparisons with experiment.

The robot was considered in the grounded phase when $x_r \leq 0$, such that a negative value of x_r indicated that the spring was compressed. Otherwise, the robot was aerial, and $F_s = 0$. A challenge of numerically integrating a 1D damped bouncing system (even on hard ground) is mitigating Zeno effects, in which the number of bounces approaches infinity in finite time [111]. This leads to significant simulation errors which scale with time-step size in detecting the transition between ground and aerial phases. To reduce such inaccuracies, we used Matlab's ODE45 integrator, which has a variable time step that is adjusted according the current system stiffness, thus accurately detecting hybrid transitions.

2.3 Minimum Amplitude Experiment

During the exploratory phase of the hard ground jumping project, we examined how to quantify jumping performance in relation to various actuation parameters. Our initial experiment measured the minimum forcing amplitude required to achieve lift-off, given that the robot starts from rest and the relative position of the actuator along the thrust rod, X_m, was prescribed to move with a sine-wave trajectory, $X_m =$

$A \sin(2\pi f t + \phi)$. For a fixed frequency, f, amplitude, A, and phase offset, ϕ and number of forcing cycles, N, we determined the minimum amplitude, A_{min}, required to achieve lift-off. After N cycles, we used the lift-off sensor to determine if lift-off occurred at any point. If no lift-off was detected, we selected a higher A for the next run, and vice-versa for when lift-off was detected. We iteratively repeated this procedure in the form of a binary search algorithm that determined A_{min} to within 0.00625 mm, the resolution of the actuator's encoder. We determined A_{min} for a range of values of f from 3 to 16 Hz in steps of 0.125 Hz, such that A_{min} vs. f could be plotted and an optimal f could be determined based on the frequency that produced the smallest A_{min}. A total of 8 plots of $A_{min}(f)$ were generated for $N = 1$ and 5 cycles, at $\phi = 0, \pi/2, 3\pi/4$, and π radians (Fig. 24).

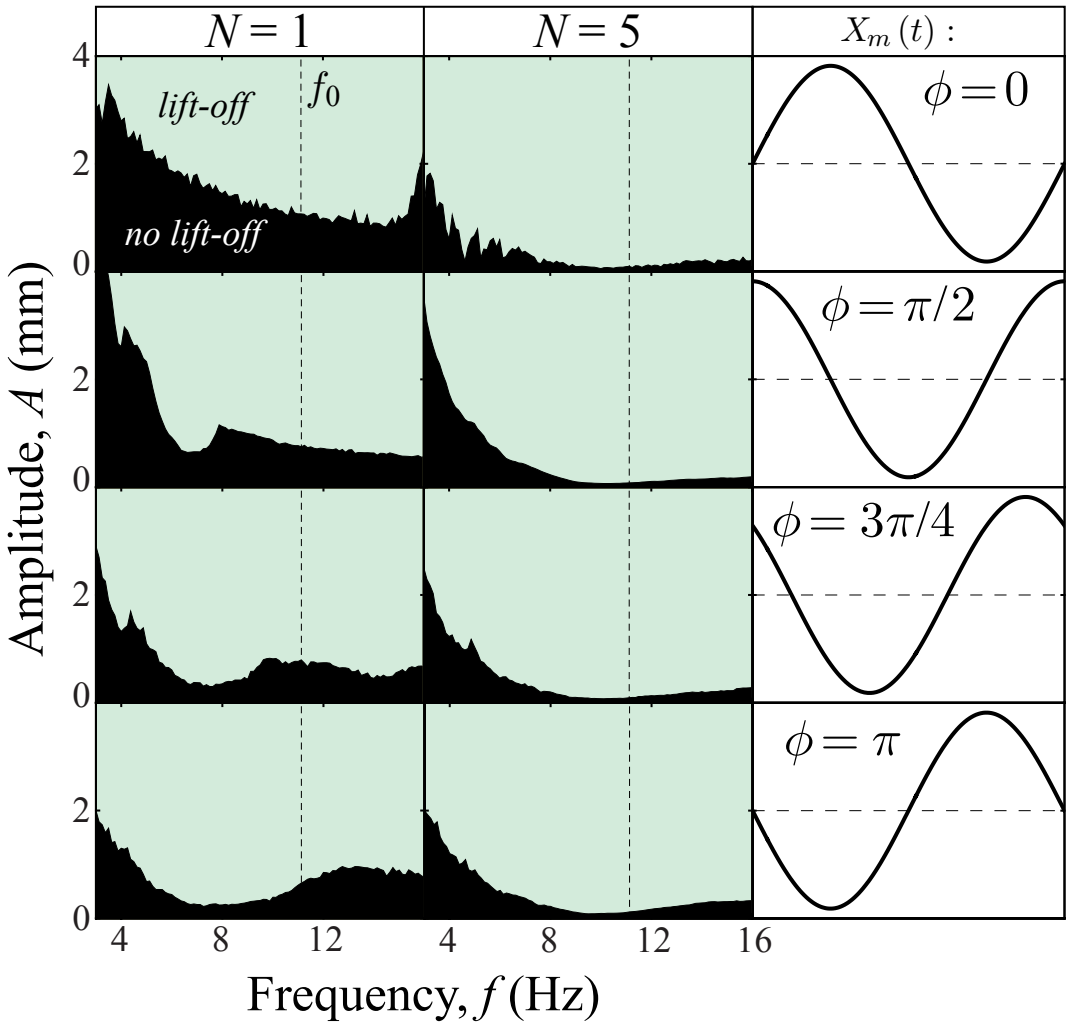

Figure 24: Minimum forcing amplitude. Left and middle columns are plots in the $A - f$ plane that indicate regions lift-off (light blue) and no lift-off (black) when the robot is forced for N = 1 cycle (left column) and N = 5 cycles (middle column) at varying phase offsets, ϕ, indicated by row in the right column. Vertical dashed lines indicate resonant frequency, f_0.

When we forced the motor for 5 cycles, the optimal f to achieve lift-off was nearly f_0. However, when the motor was only prescribed to oscillate for 1 cycle, the optimal frequency to achieve lift-off was a function of the initial phase offset. To further examine this minimum amplitude, we measured the time to lift-off (Fig.

25) by oscillating the actuator for a maximum of $N = 100$ forcing cycles. The continuity sensor measured time to lift-off in units of forcing cycles. This experiment was performed for different phase offsets ($\phi = \pi/2$, and $3\pi/2$ shown in Fig. 26) and over 30,000 different combinations of f and A (ranging from $0.27f_0 \leq f \leq 1.51f_0$, and $0 < A \leq 6$ mm).

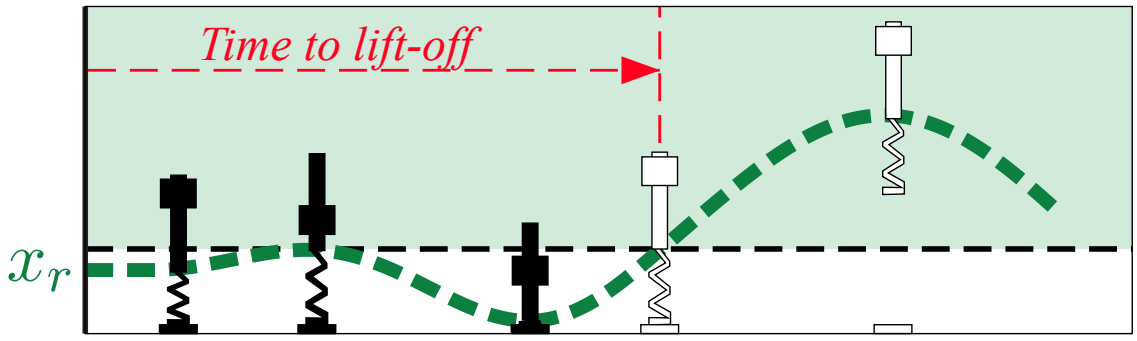

Figure 25: Illustration of the measurement for time to lift-off.

As A was decreased, there was a monotonic increase in the cycles to lift-off until a limiting A below which the robot was unable to achieve lift-off within 100 cycles (Fig. 26, data is plotted with a threshold time of 5 cycles). As f approached a frequency near the natural frequency, f_0, this limiting amplitude reached a minimum. The frequency, f_{100}, at which this minimum amplitude occurred, was defined as the optimal frequency to achieve lift-off within 100 cycles with the lowest amplitude possible. This experiment was also repeated in simulation with excellent agreement with experiment (Fig. 26 insets), although the experimental f_{100} was slightly less than the theoretical natural frequency, f_0, calculated from $f_0 = \frac{1}{2\pi}\sqrt{k/m}$, whereas the simulated $f_{100} = f_0$. We suspect that the discrepancy is attributed to untuned PID feedback gains in the control of the actuator, which produced unintended damping in the robot. Taking into consideration only the characterized damping of the spring, $\zeta = 0.0083$, one can assume that the robot's natural frequency, f_0, is approximately equivalent to the resonant frequency, $f_r = \frac{1}{2\pi}\sqrt{k/m}\sqrt{1-2\zeta^2}$. However, we suspect

that the unintended damping from the untuned feedback parameters resulted in a non-negligible decrease in the resonant frequency. In all further experiments, the control gains were tuned for optimal positional tracking and minimization of damping not associated with the robot's spring. Between jumping experiments, this damping effect was exploited by reducing feedback gains to more rapidly slow the robot to rest upon collision, accelerating automation times. This was especially useful for jump height experiments (Section 2.4) which produced large bounces and vibrations.

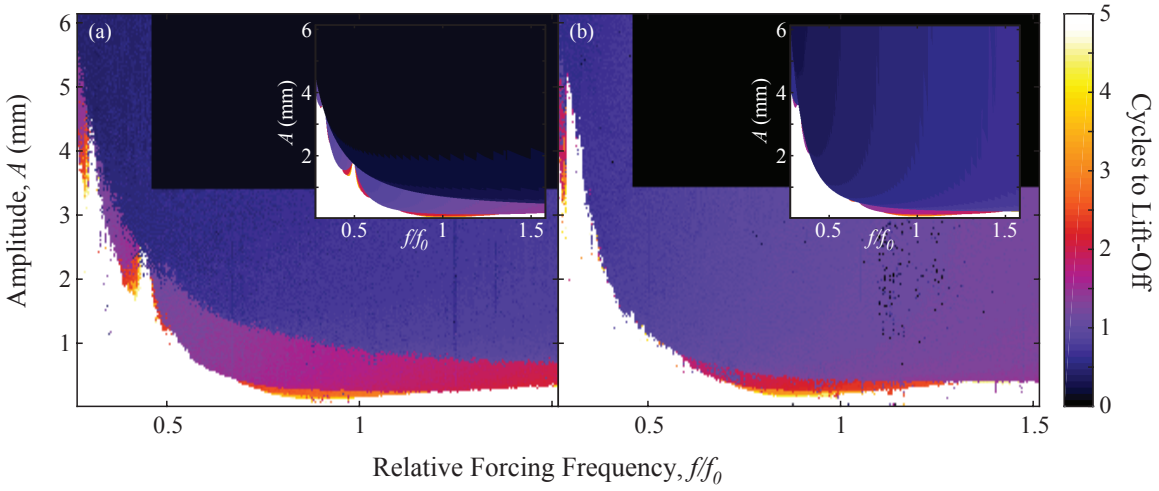

Figure 26: Experimental time to lift-off in number of forcing cycles versus amplitude and frequency for (a) $\phi = \pi/2$ and (b) $\phi = 3\pi/2$. Insets are the respective simulation results. Time to lift-off was not measured experimentally for parameters $A > 3.5$ mm and $f/f_0 > 0.5$, as preliminary low resolution experiments indicated that such actuations were not necessary to examine optimal frequencies.

Regardless, due to resonance, f_{100} was always f_0 regardless of ϕ. Lowering the cut-off cycle time, the minimum A increased, and the optimal frequency remained at resonance, $f_N = f_0$, down to approximately $N = 2$ cycles. As N approached 1 cycle, the optimal frequency deviated from resonance and became dependent on ϕ. Due to this deviation from resonance, we hypothesized that the optimal frequency for maximal jump height, h, at a given A and ϕ would also be off resonance, since typical amplitudes desired for meaningful jump heights, i.e. $h > A$ or $h >> mg/k$, produced lift-off times of 1 cycle or less, making jumping a more transient process.

2.4 Jump Height and Motor Power

To test the hypothesis that optimal frequency during jumping is off resonance, the next experiment involved measuring the robot's jump height for numerous 1-cycle jumps. Here we provide an overview of the experimental results from Aguilar et al. [3]. The actuator was commanded to move from rest in all experimental runs with a sine wave position trajectory relative to the thrust rod at a fixed frequency, f, amplitude, A, and phase offset, ϕ. Keeping A constant at 4 mm, a total of 6720 combinations of (f, ϕ) for $0.4f_0 \leq f \leq 1.4f_0$ (where f_0 is the robot's natural frequency) and phases $0 < \phi \leq 2\pi$ were tested, with 3 trials averaged for each set of parameters for a total of 20160 experiments (Fig. 27(a)).

To verify the theoretical model, we recreated the experiment in simulation with a MATLAB Simulink model that integrated Equation 4. MATLAB integrated the model with a 1000 x 1000 data point resolution, which yielded good agreement with experiment (Fig. 27(b)). We then used the model to generate other measures in the experiment such as number of jumps to execute the final jump (Fig. 28), lift-off time, and internal deformation power, P_{def}, which is defined as the power generated by internal forces required to control x_a excluding external forces such as gravity and spring forces (Fig. 27(d)).

The data in each pixel of the experiment (Fig. 27(a)) represents a jump height averaged over three trials. The variation from jump to jump was small, with the standard deviation being less than 0.5 mm, or approximately 1% of mean h, for frequencies higher than approximately 4 Hz. In a few phases, certain fractions of f_0 below this 4 Hz exhibited significant variance due to small multi-jumps that occurred as a result of sub-resonant harmonics. This occurred in a fairly complex region in the $\phi - f$ plane labeled "MJ" for multi-jumps in Figure 27(a,b). These regions, delineated by white lines, were extracted from simulation (Fig. 28). While this complex region is labeled multi-jumps, the model shows how this region periodically produced up

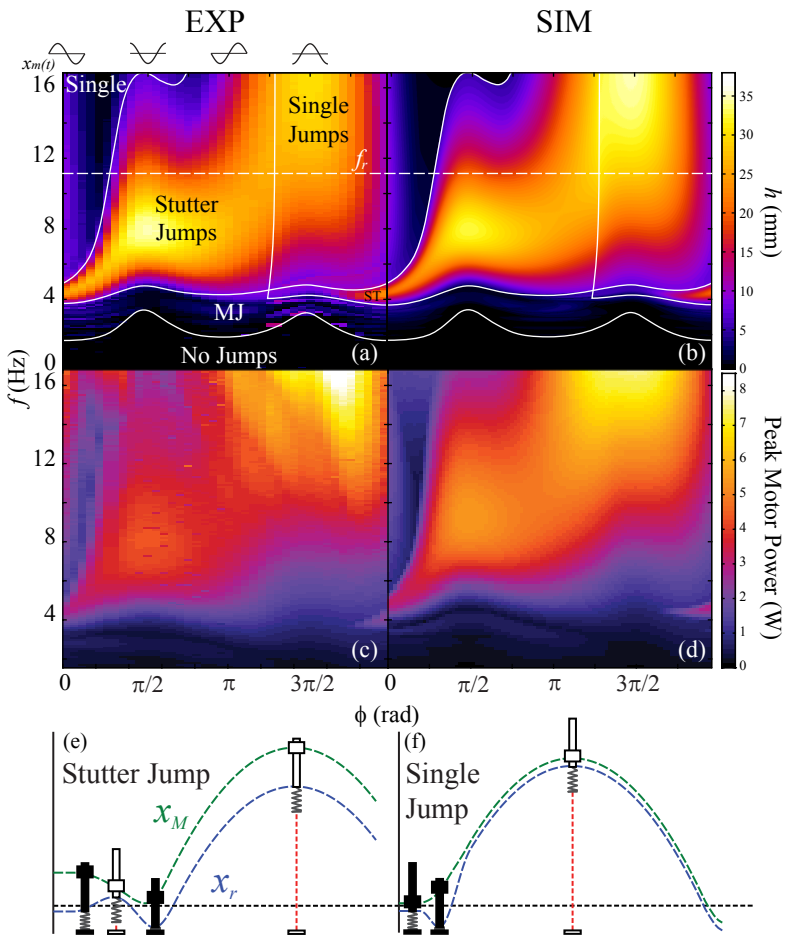

Figure 27: Experimental hard ground jumping results vs simulation. Color maps of (a,b) jump height and (c,d) peak motor power for (a,c) experiment and (b,d) simulation vs frequency and phase offset. Areas were stutter jumps and single jumps (illustrated in e and f, respectively) occur are outlined by white lines in (a).

to 5 small jumps while the motor was still oscillating, which was also evident in the experiment.

The maximum jump heights, h, for a given ϕ were similar amongst phase offsets, ranging approximately as $20 \leq h \leq 35$ mm or $5A \leq h \leq 8.75A$ (Fig. 27(a,b)). However, two broad peaks in jump height occurred at $\phi = \pi/2$ and $3\pi/2$, and the optimal frequencies, f_o, at these phase offsets were off resonance, as predicted from the lift-off experiment. At $\phi = 3\pi/2$, $f_o > f_0$, which corresponds to a single jump, in which the motor's initial relative position was near the bottom of the thrust rod

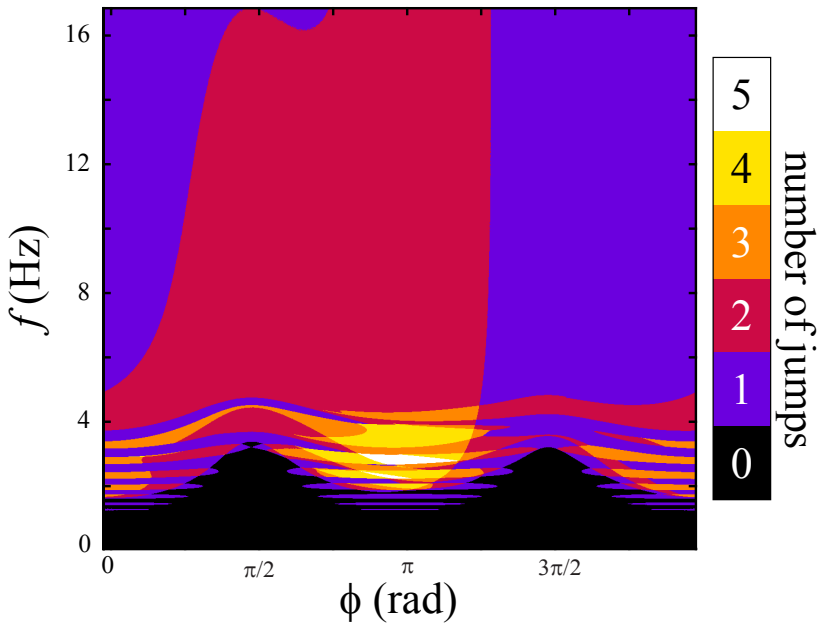

Figure 28: Number of jumps in the phase-frequency plane. Model simulation for number of jumps in the phase-frequency plane using experimental parameters. Single jumps are one jump, stutter jumps are two jumps.

and began its trajectory by immediately pushing the rod downward to compress the spring against the ground. At $\phi = \pi/2$, $f_o < f_0$, which corresponds to a stutter jump, in which the robot pulled the rod into the air for an initial hop, and then pushed the rod back into the ground during landing to compress the spring and produce a second, faster lift-off. These results were verified in simulation.

2.4.1 Understanding off-resonant optimal frequency

At first glance, Equation 4 looks completely tractable. Unfortunately, the discontinuity associated with the aerial phase rendered the equation "piecewise linear", which is to say nonlinear. Indeed, simulations of Equation 4 showed a wide variety of behaviors (including bifurcations, hysteresis, chaos). The situation is reminiscent of other piecewise linear dynamical systems which display complex dynamics, including the tent map [86] and the bouncing ball [201]. Nevertheless, using analysis and numerics, Equation 4 allowed us to gain insight into the experimental observations. In a later

section, we will discuss how both of these tools – numerics and analytical derivation – allowed us to expand this work and understand how optimal frequency was affected by changing system parameters. We were particularly interested in why optimal jumps occurred only off resonance.

Single Jump – Consider first the peak labeled S in Figure 27(a), representing the highest single jumps. This peak occurred at actuator phases near $\phi = 3\pi/2$. For a relatively slow thrust rod mass, jump height is proportional to the square of the absolute motor velocity, $\dot{x}_m(t) = \dot{x}_r + \dot{X}_m$, at take-off, where $\dot{X}_m(t) = A\omega\cos(\omega t + \phi)$. Assuming $m_r << m$ and no damping, we can obtain $\dot{x}_m(t)$ by analytically solving the differential equation of the system (Equation 4) while grounded for $\phi = 3\pi/2$.

$$\dot{x}_m(t) = \frac{A\omega^2}{\omega_0^2 - \omega^2}\omega_0\left(\frac{\omega_0}{\omega}\sin(\omega t) - \sin(\omega_0 t)\right), \tag{6}$$

where $\omega = 2\pi f$ and $\omega_0 = 2\pi f_0$. Thus $\dot{x}_m(t)$ is a prefactor times the sum of two opposing sinusoids (the one at frequency f_0 represents the transient response, which mixes with the steady state contribution). The prefactor generally favors f near f_0, but destructive interference suppresses $\dot{x}_m$ close to resonance. Moving off resonance, the prefactor favors higher f over lower, so the optimum f lies somewhat above f_0. Thus the single jump will be optimized at a frequency, $\omega > \omega_0$, or $f > f_0$. Additionally, while the prefactor favors a higher f over frequencies lower than f_0, the optimal frequency is also upper-bounded, since a higher f produces a faster time to take-off, which limits the time available to amplify power. While this argument holds regardless of A, a consequence of increasing A is that lift-off will occur even faster, potentially increasing the optimal frequency.

Stutter Jump – Understanding the presence and optimal frequency of the stutter jump was more complicated than the single jump; the existence of two jumps introduced nonlinearities due to the piece-wise nature of the system, making it difficult to dissect analytically. However, the emergence of the stutter jump could be understood through a conceptual analysis. Consider, for example, the case of $\phi = \pi/2$, so that

the initial actuator acceleration is negative. This causes the less massive thrust rod to be accelerated upward before moving down to compress the spring and lift off again.

Interestingly, the stutter jump was observed for phases somewhat larger than π, in which the initial actuator acceleration was expected to progress positively from 0. This phenomenon can be explained by the actuator's physical constraint. Regardless of phase offset, the actuator must start from rest. Any phase offset corresponding to a non-zero initial actuator velocity caused an initial impulse acceleration to the intended initial velocity. This resulted in an initial actuator trajectory that was not an ideal sine wave. For a phase such as $\phi = \pi$, the initial relative actuator acceleration was large and negative (Fig. 29), which briefly caused a large upward acceleration in the rod, causing an intermediate hop.

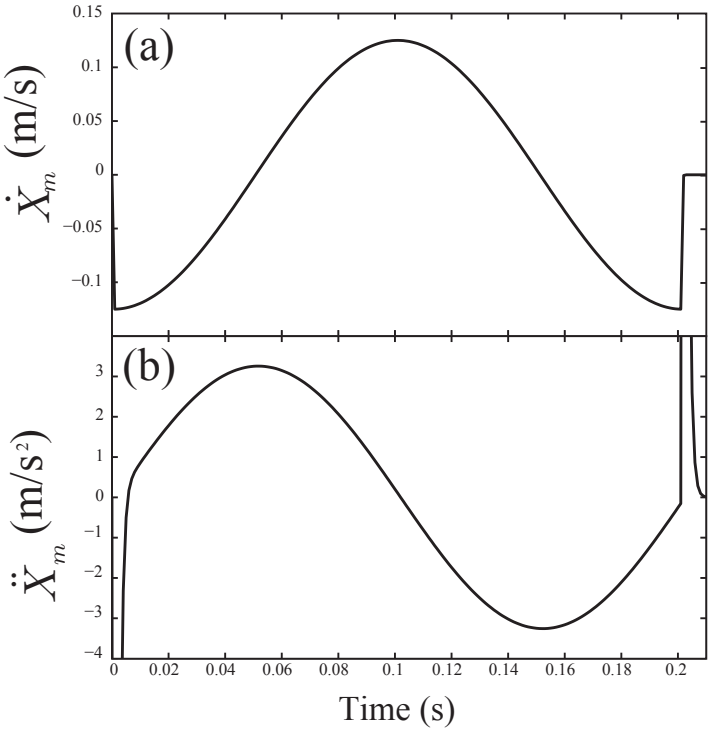

Figure 29: Simulation of an initial actuator impulse. $\phi = \pi$.

The key to understanding the optimization of the stutter jump was to consider the system energetics and the conditions that maximize the total work done during

the forcing cycle. The instantaneous power input is $P = F_{ext} v_m$, where the F_{ext} is the total external force, which includes gravity and spring forces, and v_m is the velocity of the center of mass of the robot, which can be approximated as $\dot{x}_m$, since $m_r << m_m$. The total work done be external forces is maximized when $\dot{x}_m$ both is large in magnitude and has the same sign as F_{ext}.

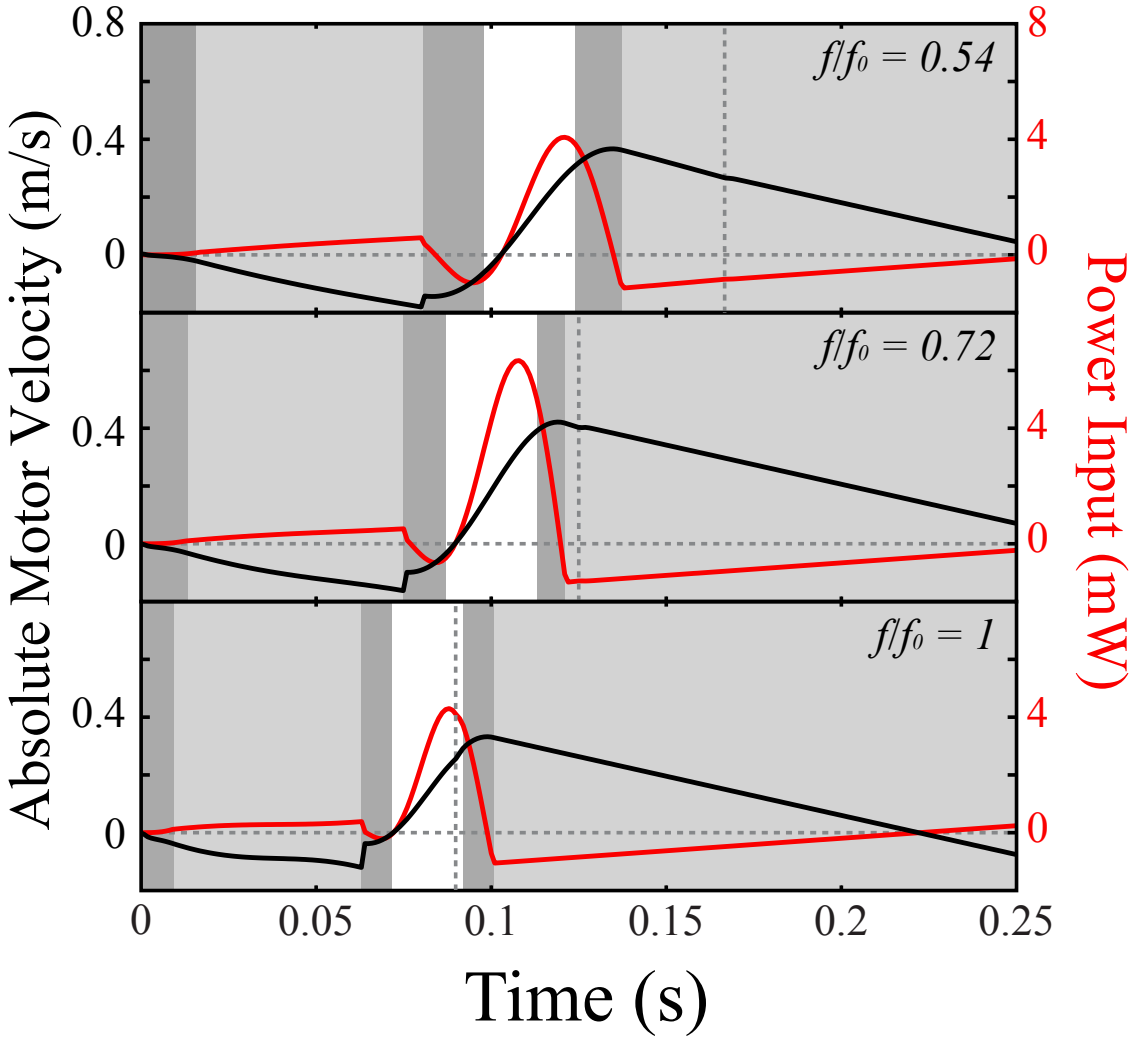

Figure 30: Simulated input power and motor velocity at different f. Absolute actuator velocity (black) and power input by external forces (red) for $f/f_0 = 0.54$, 0.72 (optimal) and 1, at $\phi = \pi/2$. The vertical dotted line indicates the time past which $\dot{x}_m = 0$. Light grey areas indicate the aerial state ($x_r > 0$); dark grey indicates negative force ground state ($mg/k < x_r <\leq 0$); white represents positive force ground state ($x_r \leq (mg/k)$).

Figure 30 illustrates this situation for $\phi = \pi/2$, which is when the stutter jump

is optimal. At $f = f_0$ (lower panel), the actuation is too fast and the actuator's relative motion is finished well before lift-off. At a low f (top panel), the actuation is too slow, causing the actuator to stop after lift-off. This results in much of the power stroke being wasted in the air. The optimal driving frequency (middle panel) lies somewhere in between the previous two frequencies, in which the motor is forced until lift-off occurs, maximizing the proportion of the stroke that benefits from elastic power amplification while on the ground.

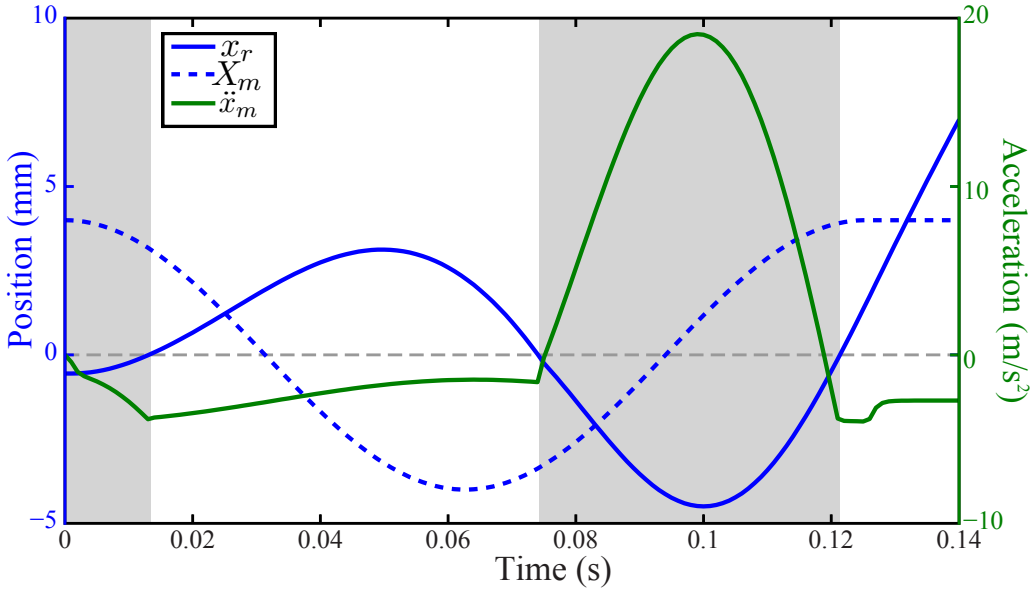

Figure 31: Simulated trajectory of the optimal stutter jump. $\phi = \pi/2$, $f = 7.98$ Hz. Grey areas indicated the grounded state; white areas indicate the aerial state.

Figure 31 illustrates the trajectory of this optimal frequency. The motor starts at the top and moves down then back up relative to the rod (countermovement). Just milliseconds before making contact with the ground, the motor begins to move upward along the rod, pushing the rod down towards the ground. Interestingly, this subtle pre-landing movement has been observed to benefit human jumping during drop jumps [100]. Once on the ground, the spring is eventually compressed maximally due to a combination of momentum from falling and motor forcing. When the spring reaches

maximum compression, both $\dot{X}_m$ and $\ddot{x}_m$ are at maximal values. The combination of these two maximizations causes optimal power amplification of the motor stroke and an explosive acceleration during push-off, maximizing $\dot{X}_m$ at lift-off.

Thus the optimality of the stutter jump not only depends on the phasing of competing sinusoids while on the ground, but also on the proper timing of aerial and ground states. The latter does not generally occur at f_0. The frequency range in which stutter jumps are optimal is more narrow than for single jumps, which can be explain by the additional sensitivity to proper timing. Another consequence is a strong dependence of optimal f with respect to the forcing amplitude, A. A larger A produces lower optimal f, and a smaller A results in a higher optimal f. This strong amplitude dependence is in direct contrast to the single jump mode, which does not show a strong dependence to A. In a later section (Section 2.5), the effect of A (and the more generalized nondimensional scale $\alpha = mg/kA$) will be discussed. We will illustrate how simplified descriptions of the stutter jump's trajectory simultaneously provide intuition into how the timing of the air and ground phases affect optimal frequency at different scales as well as equations that predict optimal frequency vs α.

In summary, the non-intuitive result of an off-resonant optimal frequency was explained by the transient nature of the jump; for the single jump, the spring-mass system does not have time to fully leverage resonance build-up. Thus, the optimal frequency is more dominantly determined by the competing sinusoidal homogeneous and particular terms of the ODE solution for the robot's position trajectory. For the stutter jump ($\phi = \pi/2$), the piece-wise linear nature of the jump does not allow for the same ODE analytical study, however, the robot being airborne is an indicator that the natural frequency is not the only time scale involved; there must be proper timing between air and ground phases to achieve optimal jump height.

2.4.2 Peak Motor Power

In addition to jump height, we also extracted the robot's motor power vs. time by recording the motor's relative velocity and current from the motor's amplifier and encoder, where the current is directly proportional to the force. Motor power was then calculated by $P = FV$. While the jump heights of the optimal stutter jump ($\phi = \pi/2$ and $f_O = 0.78f_0$) and single jump ($\phi = 3\pi/2$ and $f_O = 1.4f_0$) were comparable, the peak motor power required for the single jump was 66% greater than that required for the stutter jump (Fig 27(c)), confirmed in simulation (Fig 27(d)). This was due to the difference in relative motor velocities of the two velocities. While the magnitudes of peak forces were similar between the two jumps, with the stutter only producing 25% greater peak force (and consequently jumping slightly higher), the peak velocity of the single jump was 100% greater than that of the stutter jump. The stutter jump – which was observed to simultaneously produce slightly higher jumps than the single while requiring less peak power in our jumping robot – is a maneuver which has been observed in nature in the jumps of lemurs [59], the *Galago moholis* bushbaby [88], and rodents [68, 116].

2.5 Nondimensional Scale Analysis

The results of our robotic experiments, however, only apply to specific parameter values of mass, m, gravity, g, spring stiffness, k, and forcing amplitude, A. Excluding damping (assuming damping is small) and the mass of the thrust rod and spring relative to the total mass, we can describe the behavior of the robot in terms of the non-dimensional variable $\alpha = mg/kA$. The analysis of previous experiments and simulations examined the minimum forcing amplitude to achieve lift-off (Section 2.3) and the effect of the amplitude, A, on the optimal frequency of the stutter jump (Section 2.4.1). These experiments have hinted at the influence of α (since, changing A while keeping other parameters constant changes α).

To confirm observations made in Section 2.4.1 about the effect of A on f/f_0 for the stutter jump, we extended the simulations performed in Section 2.3 to measure jump height vs f/f_0 and A for both single jumps ($\phi = 3\pi/2$) and stutter jumps ($\phi = \pi/2$) (Fig. 32(a,b)). The protocol for these simulations mirrored those of the jump height experiments, whereby, instead of oscillating for $N = 100$ cycles as in Section 2.3, the jumping model was simulated to oscillate for $N = 1$ cycle, after which jump height was measured in terms of the robot's maximum center-of-mass position. The phases $\phi = \pi/2$ and $\phi = 3\pi/2$ were chosen, because simulations confirmed that, for all α, the highest stutter and single jumps based on center-of-mass height always occurred at $\phi = \pi/2$ and $\phi = 3\pi/2$, respectively. The white outlines in Figure 32(a,b) represent the minimum amplitude required to achieve lift-off, and mirror the structure observed in the time to lift-off simulations (Fig. 26). As was found in our analyses in Section 2.4.1, optimal frequency increased with increasing A for the single jump and decreased with increasing A for the stutter jump (Fig. 32(a,b), black lines).

These effects can be considered in terms of the non-dimensional variable α. In simulation, we studied how non-dimensionalized jump height, optimal frequency and power changed vs. α (Fig. 32(c,d)). We performed the same parameter sweep of relative frequency, f/f_0 (for low damping, the natural frequency, $f_0 \approx f_r$) and phase offset, ϕ, as in our original experiment.

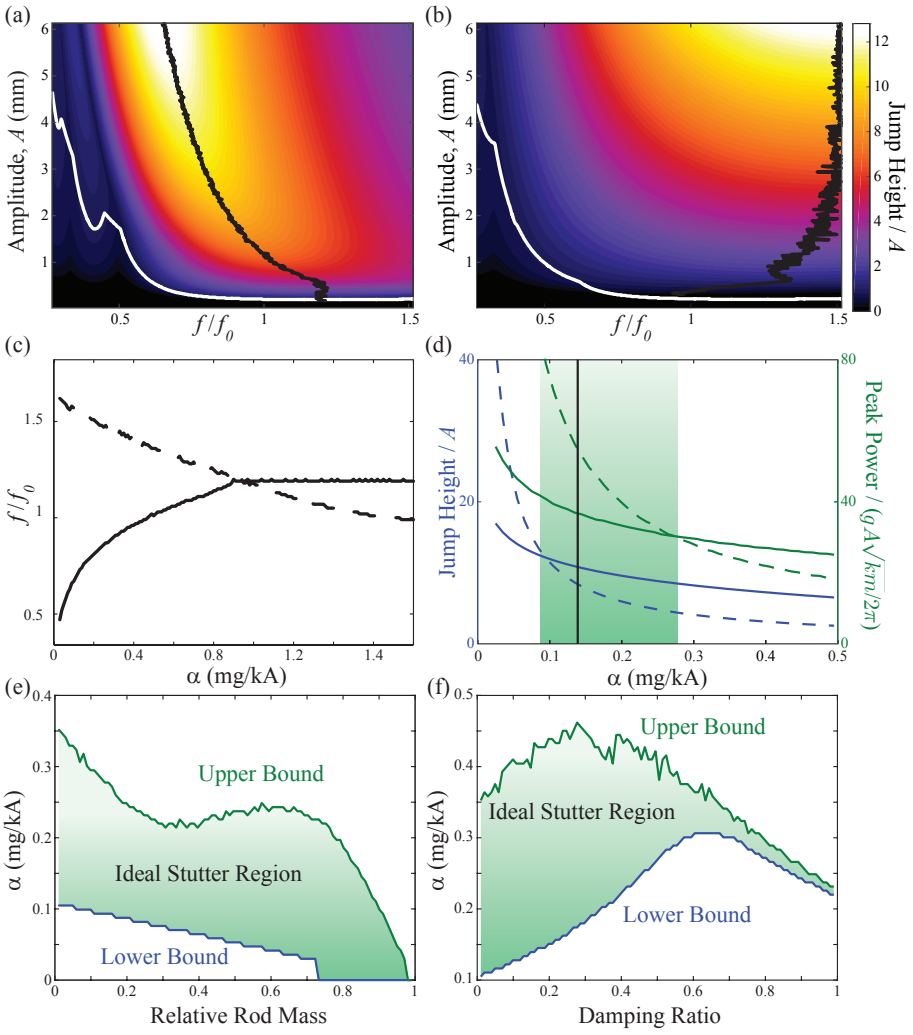

Figure 32: Influence of scaling parameters on relative jumping performance of the single jump and stutter jump. (a,b) Simulated jump height / amplitude of (a) stutter jump and (b) single jump vs forcing frequency and amplitude. White lines indicate minimum amplitude to achieve lift-off. Black lines indicate forcing frequency that yielded the highest jump for given amplitude. (c) Optimal frequency vs α of stutter jump (solid) and single jump (dashed). (d) Jump height (blue) and peak power (green) of single jump (dashed) and stutter jump (solid). Green shaded region indicates ideal stutter region. Black line indicates α of experimental robot. Ideal stutter jumping region (α range, green shaded) vs (e) relative rod mass and (f) damping ratio.

As $\alpha \to 0$, jump heights and peak motor power of both jumps exponentially increased. Jumping with high α (i.e. $\alpha >> 0.1$) resulted in poor jumping performance, particularly evident when jump height was normalized by the equilibrium position, mg/k. For low α ($\alpha < 0.1$), the single jump had a greater jump height and required a higher peak power than the stutter jump, however, the stutter jump height and power both surpassed that of the single jump at $\alpha = 0.09$ and $\alpha = 0.28$, respectively (Fig. 32(d)). For our experimental robot, $\alpha = 0.13$, which is within this ideal regime in which the stutter jump's height is greater than the single jump, and has a lower power requirement. Regardless of α, however, the power efficiency of the stutter jump, height/power, was always greater than that of the single jump.

We also examined the effect of increasing the mass of the rod relative to the total mass as the effect of changing the spring's damping. Increasing these parameters reduced the jumping performance of both jumps. Increasing these parameters also produced non-trivial changes to the α range of the ideal regime for stutter jumping defined by lower power and higher height stutter jumps (Fig. 32(e,f)). Increasing relative rod mass shifted this region to lower α values. Increasing the damping ratio, ζ, produced a positive shift in the ideal α regime until stutter jump became so ineffective as compared to the single jump that the region began to narrow and then shift negatively for higher ζ.

2.5.1 Influence of α on optimal frequency

Increasing α decreases the forcing amplitude, A, relative to the spring-mass equilibrium position, which, in turn, increases the portion of time the robot spends on the ground before final lift-off. An increasing α causes the optimal frequency f_{opt} to approach f_0 for the single jump and nearly f_0 for the stutter jump (Fig. 32(a)). What follows is an analytical understanding of f_{opt} versus α.

For the stutter jump, a low α results in $f_{opt} < f_0$ with increasing f_{opt} as α increases

until $\alpha \approx 0.9$, at which point $f_{opt} \approx 1.2 f_0$ for all $\alpha \geq 0.9$. It is interesting to note that f_{opt} of both jump types (single and stutter) are nearly identical at this point. The stutter jump exhibits qualitatively different dynamics depending on whether $\alpha < 0.9$ or $\alpha \geq 0.9$. As such, each case has a unique analytical treatment.

We focus on developing an understanding the optimal frequency of the stutter jump. For the case of $\alpha < 0.9$, the stutter jump exhibits hybrid dynamics (both ground and air phases), making it difficult to extract analytical solutions for optimal frequency through standard means of integrating the differential equations of the robot (as was done for the single jump [3]). However, making some conceptual simplifications, one can still attain an estimate of the optimal stutter frequency and understand why it is optimal below the natural frequency. Below are a few different estimates of f_{opt}/f_0 vs. α. We assume no spring damping and a massless rod.

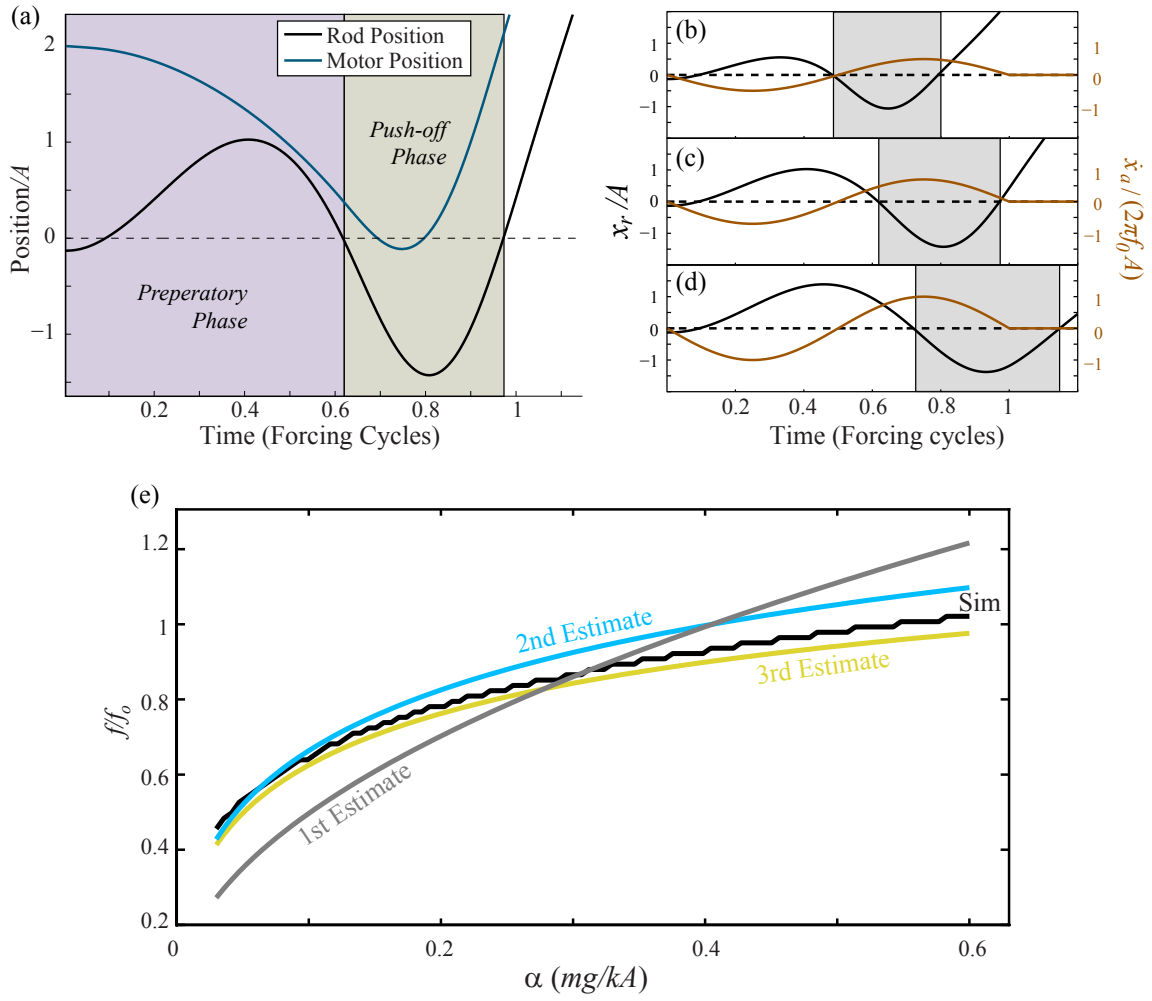

Figure 33: Stutter jump simulation analysis. (a) Typical stutter jump kinematics at optimal forcing frequency. Global motor position was offset by $2A$ to clearly see its trajectory. (b-d) Comparing optimal stutter jump rod position (black) and relative motor speed (brown) (b) below, (c) at, and (d) above the optimal frequency. (e) Optimal stutter jump frequency vs α, including simulation and analytical estimates.

1st Estimate: A half cycle of falling – During the stutter jump, the rod is pulled off the ground and the robot begins to fall (Fig. 33(a)). Thus, for the first estimate, we approximate that the robot starts airborne, falls a distance of about $2A$ with an acceleration of g and lands approximately half way through its forcing cycle. Applying

kinematic equations to this argument leads to the following relation.

$$0 = 2A - \frac{1}{2}gt^2, \tag{7}$$

where t is half of the forcing period. Thus forcing frequency relative to the natural frequency, $f_0 = \sqrt{k/m}/2\pi$, is calculated as

$$\frac{f}{f_0} = \frac{\pi}{2}\sqrt{\alpha}. \tag{8}$$

While not accurate (Fig. 33(e)), the derivation of this first guess provided basic intuition for how the optimal frequency is broadly influenced by how much time the robot spends in the air versus on the ground before final lift-off. This is more clearly illustrated by the 2nd estimate of optimal frequency.

2nd Estimate: Lift-off at end of forcing cycle – Contrary to the assumption used in the first estimate, the timing of the preliminary hop's landing relative to the forcing cycle depends on α. However, a consistent observation from simulation independent of α is that, due to the phasing required to maximize output energy, the robot reached final lift-off near the end of the forcing cycle when forced at f_{opt}. The motor transfers energy to the robot while the spring is in contact with the ground ($x_r < 0$), which is primarily during the push-off phase (Fig 33(b-d)).

Motor energy is calculated by integrating the motor power, $P_m = F_m\dot{x}_m$, during push-off. For low damping and low relative rod mass, F_m is dominated by the spring force, F_s, which is proportional to the rod position (or spring compression) by k. Thus, $P_m \propto x_r\dot{x}_m$, where x_r during push-off can be approximated by a half sine wave at f_0, and $\dot{x}_m$ is also a sine wave. As a result, the integration of P_m is maximized by keeping the second half cycle of the motor's velocity trajectory approximately in phase with the spring-mass oscillation, leading to the robot lifting off near the end of the forcing cycle.

Revising the first estimate, the *full* cycle consists of the time spent falling and the time spent on the ground. The time on the ground, dominated by the spring's

dynamics, is estimated as a half period of the natural frequency, thus

$$t = 2\sqrt{\frac{A}{g}} + \pi\sqrt{\frac{m}{k}}, \tag{9}$$

where t is now the full period of forcing. Taking the inverse of t and dividing by f_0, the relative optimal forcing frequency is then estimated as the following:

$$\frac{f}{f_0} = \frac{1}{\frac{1}{2} + \frac{1}{\pi}\sqrt{\frac{1}{\alpha}}}. \tag{10}$$

While this estimate is more accurate than the first (Fig. 33(e)), it still produces a simple expression that more directly illustrates the competition between the grounded and airborne timescales. In fact, this competition of timescales is embedded within the expression for the dimensionless variable, $\alpha = mg/kA$, which can be rewritten as

$$\alpha = T_{ground}^2/T_{air}^2, \tag{11}$$

where $T_{air} = \sqrt{A/g}$ is the airborne timescale, and the grounded timescale, $T_{ground} = \sqrt{m/k}$, is proportional to one period of oscillation at the natural frequency ($2\pi\sqrt{m/k}$). If gravity is decreased or the forcing amplitude is increased (which corresponds to a lower value of α), the robot will spend more time falling in the air (i.e. the preliminary hop) relative to the time spent on the ground, thus reducing the optimal frequency to a value lower than the natural frequency.

3rd Estimate: Consideration of the first lift-off – To achieve higher accuracy, we now consider the time spent on the ground before the *first* lift-off, since, during the initial pull-up phase, the spring must fully decompress from equilibrium before initial lift-off. As α increases, more time is spent on the ground and less time in the air before final lift-off. In this estimate, the full forcing cycle is a combination of the time to first lift-off, air time, and a half period at f_0.

To estimate time to first lift-off, we first establish the rod's equation of motion during this initial phase. The trajectory of the massless rod is approximately driven by

the motor forcing trajectory (assuming the effect of gravitational acceleration on the trajectory is negligible during this small amount of time). A convenient simplification is to consider a constant acceleration profile instead of sinusoidal forcing. We chose the acceleration required to travel a distance of 2A starting from rest in a half period of forcing:

$$a_r = 16Af^2$$

The thrust rod is accelerated at a_r from rest from an initial equilibrium position of $-mg/k$. Thus the equation defining the time to reach a position of 0 is as follows:

$$0 = -\frac{mg}{k} + 8Af^2 t_{FirstLift}^2$$

Rearranging, we get:

$$t_{FirstLift} = \frac{1}{f}\sqrt{\frac{\alpha}{8}}$$

To determine the next component of the motor's forcing period, the time the motor spends falling during the preliminary hop (t_{air}), we find the roots of the equation describing the motor's motion during falling. Since we assume a massless rod, the motor's downward acceleration is determined by gravity, g:

$$x_m = x_0 + v_0 t - \frac{1}{2}gt^2$$

where x_m is the global position of the motor, and x_0 and v_0 are the initial position and velocity of the motor at $t_{FirstLift}$. Thus the roots are

$$t_{air} = \frac{v_0}{g} \pm \frac{\sqrt{v_0^2 + 2gx_0}}{g}.$$

Since v_0 is negative (the motor is falling) and the rooted term will always be larger in magnitude than v_0 ($|v_0| < \sqrt{v_0^2 + 2gx_0}$, assuming x_0 is positive), we only consider

the positive root:

$$t_{air} = \frac{v_0}{g} + \frac{\sqrt{v_0^2 + 2gx_0}}{g}$$

Unlike in the previous estimates, a consequence of considering $t_{FirstLift}$ is that the motor has already descended some distance and has a non-zero initial velocity at $t_{FirstLift}$. To find x_0 and v_0, we require motor's acceleration before first lift-off. This is obtained from the force balance equation for the rod and motor while the robot is grounded (assuming a massless rod):

$$-kx_r - mg = m\ddot{x}_m$$

The rod's position, $x_r = 8Af^2t^2 - mg/k$, is obtained from the rod's acceleration, a_r, which was used to find $t_{FirstLift}$. Plugging x_r into the above equation, the motor acceleration is as follows:

$$\ddot{x}_m = -\frac{k}{m}8Af^2t^2$$

We integrate and find the velocity and position:

$$\dot{x}_m = -\frac{k}{m}\frac{8}{3}Af^2t^3$$
$$x_m = 2A - \frac{k}{m}\frac{8}{12}Af^2t^4 - \frac{mg}{k}$$

Plugging in the expression for $t_{FirstLift}$, we find the initial conditions of the motor at moment, $t_{FirstLift}$, in which the motor begins to free-fall.

$$v_0 = -\frac{g}{6\sqrt{2}}\frac{\sqrt{\alpha}}{f}$$
$$x_0 = 2A - \frac{mg}{k} - \frac{\alpha g}{96f^2}$$

Plugging x_0 and v_0 into the equation for t_{air}, we get:

$$t_{air} = -\frac{1}{6\sqrt{2}}\frac{\sqrt{\alpha}}{f} + \sqrt{-\frac{\alpha}{f^2}\frac{1}{144} + \frac{2A}{g}(2-\alpha)}$$

As before, the time of the last ground phase is approximated as half of an oscillation cycle at the natural frequency:

$$t_{ground} = \pi\sqrt{\frac{m}{k}} = \frac{1}{2f_0}$$

Adding all of the components of the cycle, we arrive at an expression for the time of the total cycle:

$$t_{total} = t_{FirstLift} + t_{air} + t_{ground} = \frac{1}{f} = \frac{1}{f}\sqrt{\frac{\alpha}{18}} + \frac{1}{f}\sqrt{\frac{2A}{g}f^2(2-\alpha) - \frac{\alpha}{144}} + \frac{1}{2f_0}$$

Multiplying this equation by f and rearranging the terms, we get a quadratic equation to solve for the relative optimal frequency, f/f_0.

$$\left(\frac{1}{4} - \frac{2-\alpha}{2\alpha\pi^2}\right)\left(\frac{f}{f_0}\right)^2 - \left(1 - \sqrt{\frac{\alpha}{18}}\right)\left(\frac{f}{f_0}\right) + \left(1 + \frac{\alpha}{16} - 2\sqrt{\frac{\alpha}{18}}\right) = 0$$

Solving the above quadratic equation, we find an expression for relative optimal frequency with respect to α:

$$\frac{f}{f_0} = \frac{1 - \sqrt{\frac{\alpha}{18}}}{\frac{1}{2} - \frac{2-\alpha}{\alpha\pi^2}} - \frac{\sqrt{\left(1 - \sqrt{\frac{\alpha}{18}}\right)^2 - 4\left(\frac{1}{4} - \frac{2-\alpha}{2\alpha\pi^2}\right)\left(1 + \frac{\alpha}{16} - 2\sqrt{\frac{\alpha}{18}}\right)}}{\frac{1}{2} - \frac{2-\alpha}{\alpha\pi^2}}. \tag{12}$$

This formulation, unwieldy as it may be, produces the most accurate estimate (Fig. 33(e)). It emphasizes the competition of ground and air timescales by also considering the initial grounded phase. A decrease in α implies a relatively smaller amount of time spent on the ground before the first lift-off, either by increasing the rate at which the rod is accelerated to the zero position (increasing amplitude, A) or by reducing the rod's initial distance to the zero position (i.e. reducing the absolute value of the equilibrium position, mg/k), which further produces an optimal frequency less

dominated by the natural frequency. Of note is how accurate these estimates get without the use of sinusoidal forcing functions, suggesting that the stutter jump's timescale dynamics discussed here are largely independent of the shape of the motor's periodic forcing trajectory.

When $\alpha \geq 0.9$, the entire forcing trajectory occurs while the robot is grounded; thus, $f_O \approx 1.2 f_0$ can be explained by solving the system's ordinary differential equation for the center of mass position and velocity trajectory and maximizing the total energy after one forcing cycle, or $t = 1/f$.

The differential equation for the stutter jump is

$$\ddot{x}_m + 2\zeta\omega_n \dot{x}_m + \omega_n^2 x_m = -\frac{m_m}{m}\omega^2 A\cos\omega t - g,$$

where $\omega = 2\pi f$, $\omega_n = \sqrt{k/m}$, m_m is the actuator mass, and x_m is the actuator's position. Assuming no damping, the differential equation is solved as

$$x_m(t) = \frac{A\frac{m_m}{m}\omega^2}{\omega_n^2 - \omega^2}[\cos\omega t - \cos\omega_n t] - \frac{mg}{k}.$$

The position of the rod is found as $x_r(t) = x_m(t) - A\cos\omega t$, and thus the COM position is $x(t) = (m_m x_m(t) + m_r x_r(t))/m$. The total energy equation is obtained as the sum of the kinetic energy, potential gravitational and potential spring energy.

$$E(t) = \frac{1}{2}m\frac{dx(t)}{dt}^2 + mgx(t) + \frac{1}{2}kx_r(t)^2$$

We are interested in the energy of this system after the robot has completed one full cycle of forcing, or $t = 1/f = 2\pi/\omega$. The energy equation as a function of relative frequency, $\bar{\omega} = \omega/\omega_r = f/f_r$, where $f_r = f_0$ in the case of zero damping, is

$$E(\bar{\omega}) = \frac{\bar{\omega}^4}{(1-\bar{\omega}^2)^2}(1 - \cos\frac{2\pi}{\bar{\omega}}). \tag{13}$$

The above equation is maximal at $\bar{\omega} = 1.2$. The above equation is a simplified form that excludes constant additive terms and outer constant scaling terms that do not

affect the location of the maximum value. Note that, in this $\alpha \geq 0.9$ case, the $\phi = \pi/2$ jump is no longer technically a stutter jump by the definition of having a preliminary air phase, and is merely a counter movement with one lift-off. While our current jumping protocol of only one forcing cycle results in $f_O \approx 1.2 f_0$ for $\alpha \geq 0.9$, it can be shown that a multiple cycle protocol does result in $f_O \to f_0$ for increasing α.

2.5.2 Interactive demonstration of jumping dynamics and real-world comparisons

To illustrate the jumping dynamics discovered in [3] (and, in particular, to provide an instructive demonstration of both the stutter jump and single jump), we developed an interactive online simulator of the 1D jumper (Fig. 34). This demo also allowed the user to change the robot's parameters, giving some ability to directly visualize how changing α influences jumping dynamics.

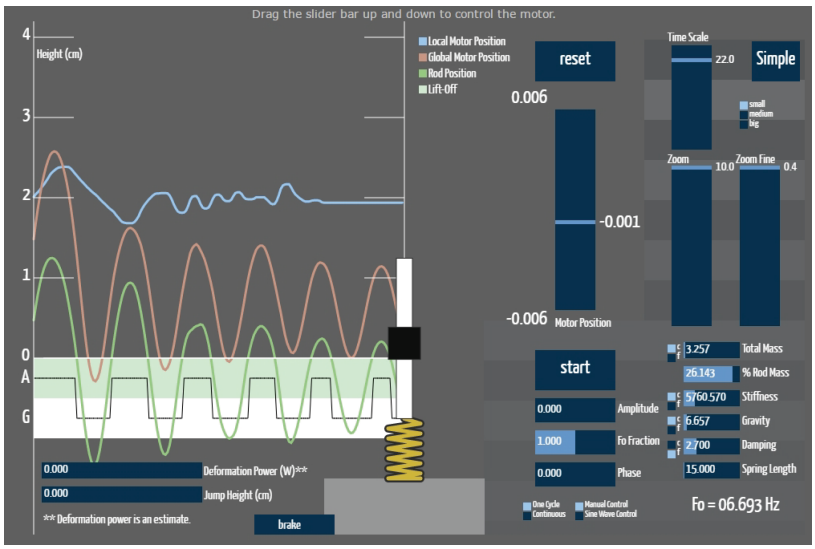

Figure 34: Interactive jumping demonstration. Developed with Processing programming language. Users are able to manually control the motor's relative position or play a sine wave trajectory with specific actuation parameters. Fine control of robot parameters and space and time scales were also provided. Available at http://crablab.gatech.edu/pages/jumpingrobot/Demo.html.

It is also useful to examine parameter values of real-world jumping systems. As a baseline, our own experimental jumper had an α value of 0.14 when performing

the jumps in our study in Section 2.4, placing the robot within the range of α values which are doubly ideal for the stutter jump in terms of both jump height and peak motor power. A simple spring mass model has been used to describe hopping and bouncing gaits in humans [72, 145]. However, obtaining values such as α for biological jumpers such as humans can be quite difficult due to the fact that humans are far more complex than our simplified robophysics jumping model, making it challenging to find equivalent values for k and ζ. Moreover it has been found that humans can alter their effective stiffness at different stride frequencies during running [71]. However, even broad parameter estimates can be instructive in approximating what types of jumps may be optimal in humans.

Such an attempt was made in a study [222] that had subjects stand on a force platform while their vertical center of mass position was perturbed in a random fashion. Using force and position data from these trials, a system identification routine determined human values for $k_h = 28500$ N/m and $c_h = 950$ Ns/m, which equates to $\zeta_h \approx 0.32$ for an assumed average human mass, $m_h = 78$ kg. If we approximate that half of a human's vertical stroke during maximal jumping would yield $A_h \approx 0.5$ m, then $\alpha_h \approx 0.05$. This would indicate that humans lie just outside the ideal range for the stutter jump (in terms of jump height, and more so given the high damping, where the model predicted about 2 m stutter jump and about a 5 m single jump). However, at lower α, the power requirements of producing the ideal single jump rapidly eclipse that of the stutter jump. Thus, one could postulate that a stutter jump may still be preferable depending on the power limitations of muscles, particularly when muscles are fatigued, which further reduces muscle power [106].

Extrapolating from human estimates for α and jumping performance, we also compared the performance of other organisms over a wide range of length scales. Assuming that the effective stroke amplitude, A, (which we approximate is proportional to one dimension of an animals body size, i.e. their body length, l) is the only

parameter that changes with body length would yield an increasing value of α for decreasing values of body length. In this case, we expect jump heights relative to body length, l, (or A) to decrease with decreasing body length. However, biological observations illustrate the opposite trend (Fig. 35). While morphology and structure in organisms produce scaling relationships that are allometric (i.e. deviations from isometric scaling) [36], even simplified isometric scaling arguments [207] can be helpful to obtain an intuitive understanding of how α scales with body size.

Assuming mass scales proportionally with volume, mass will scale with body length cubed ($m \propto l^3$). To obtain a scaling for stiffness, k, we assume animals (particularly vertebrates) have elements contributing to an effective elastic mechanism (i.e. tendons and muscles) with similar mechanical properties. We furthermore describe these elastic members as a bundle of series and parallel spring-like elements. In such a case, an isometric scaling would dictate that k scales proportionally with body length ($k \propto l$). Using human parameter estimates [222], we arrived at a scaling relationship (Fig. 35 inset) for α vs l:

$$\alpha = \frac{m_h g}{k_h A_h} \frac{l}{l_h}, \tag{14}$$

where we used an average human height, $l_h = 1.8$ m. Thus, as body size increases, so does α.

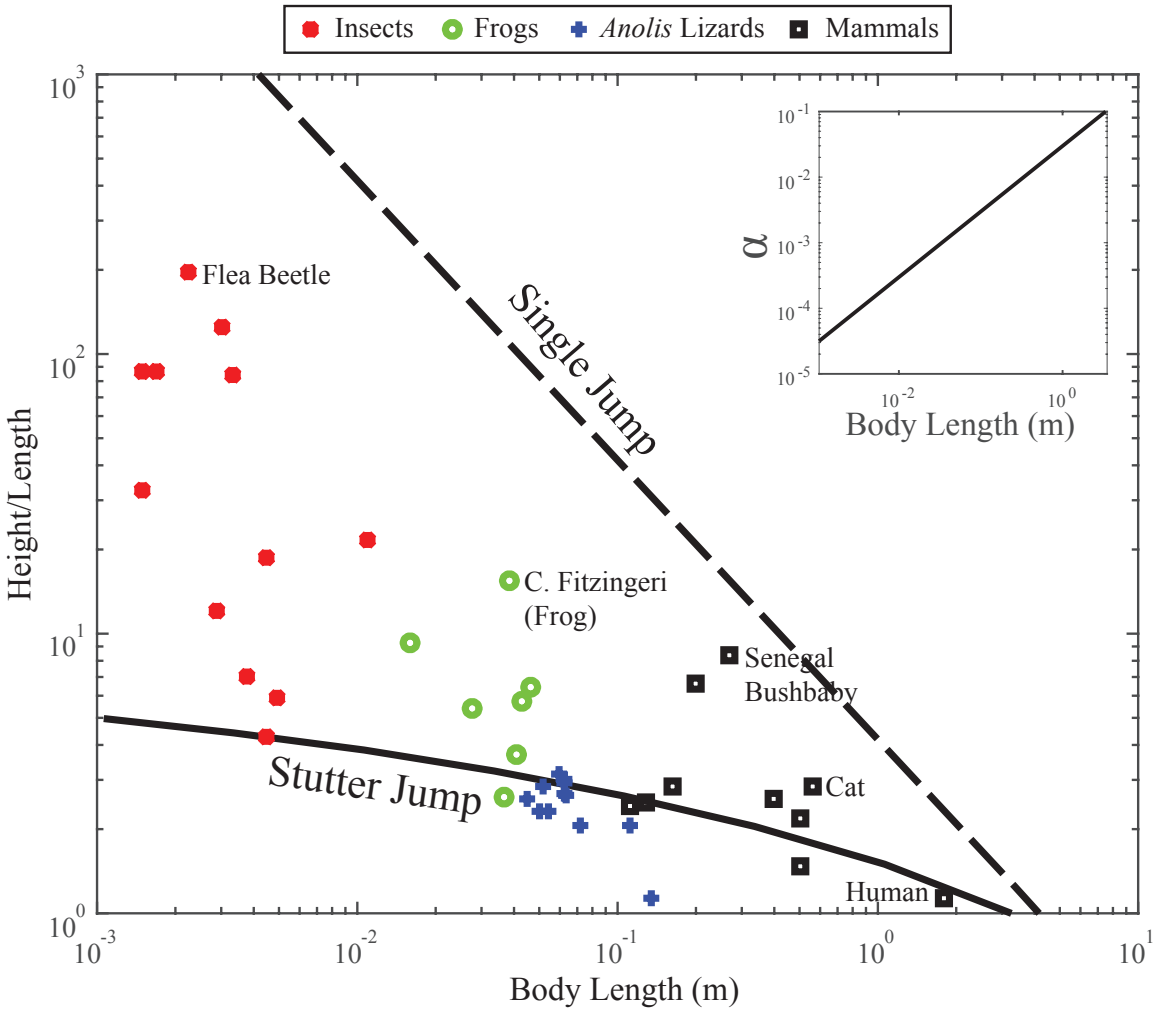

Figure 35: Comparison between spring-mass jumping model and biological jumps: jump height relative to body length vs body length. Simulated single jumps (dashed) and stutter jumps (solid) are calculated using values of α (inset) that scale from simplified isometric scaling relationships [207] relative to experimental human values [222] of mass, length and stiffness. Biological jump height data was compiled from numerous studies [84, 29, 70, 94, 44, 174, 175, 227, 52, 53, 179, 130, 206, 219, 91, 88, 60, 59, 197, 1, 97, 120, 56, 42, 208, 123, 100, 116, 68, 143].

For constant damping and relative rod mass, we simulated single jumps (Fig. 35 dashed line) and stutter jumps (Fig. 35 solid line) for the range of l in which

biological jump heights have been measured. Most animals tend to perform better than the simulated stutter jumps and worse than the simulated single jumps. Variations in morphology (such as relatively longer legs) will affect α values for individual organisms. Additionally, the simulated single jump heights are at optimal frequency, where motor power requirements quickly increase as α decreases. There may be power limitations in achieving the optimal single jump. In fact, various organisms [84, 29, 70, 94, 44, 174, 175, 227, 52, 53, 179] such as frogs and insects utilize a different strategy of jumping altogether: the catapult jump, which does not require high power inertial loading of elastic energy. Elastic energy can be slowly stored and then released all at once with a catch mechanism. The bush baby is also suspected of producing some combination of a countermovement (capable of producing a stutter jump), squat jump (akin to the single jump) and catapult [1]. Of those animals that do not use the catapult mechanism, it is highly unlikely that they are utilizing perfect sinusoidal actuations. Thus for maximal height jumps, we posit that organisms may be independently optimizing different phases of their jump (such as the stutter jump's aerial and ground phases) up to the power limit of their muscles.

2.5.3 Asymmetric trajectories: the two-frequency stutter jump

Building on the physical intuitions of how the gravitational and spring-based time scales that influence the optimization of the single jump and the stutter jump, we also examined the optimality of a stutter jump that is composed of two half cycles at distinct forcing frequencies. Such a jump would not be constrained to a single frequency that can compromise on the individual optimization of the gravity influenced pull-up phase and spring-mass dominated push-off phase.

Not surprisingly, the two-frequency stutter was always able to perform higher jumps than either the stutter jump or the single jump (Fig 36(a)). This effect was magnified at lower values of α due to the reduced relative strength of gravity, thus, a

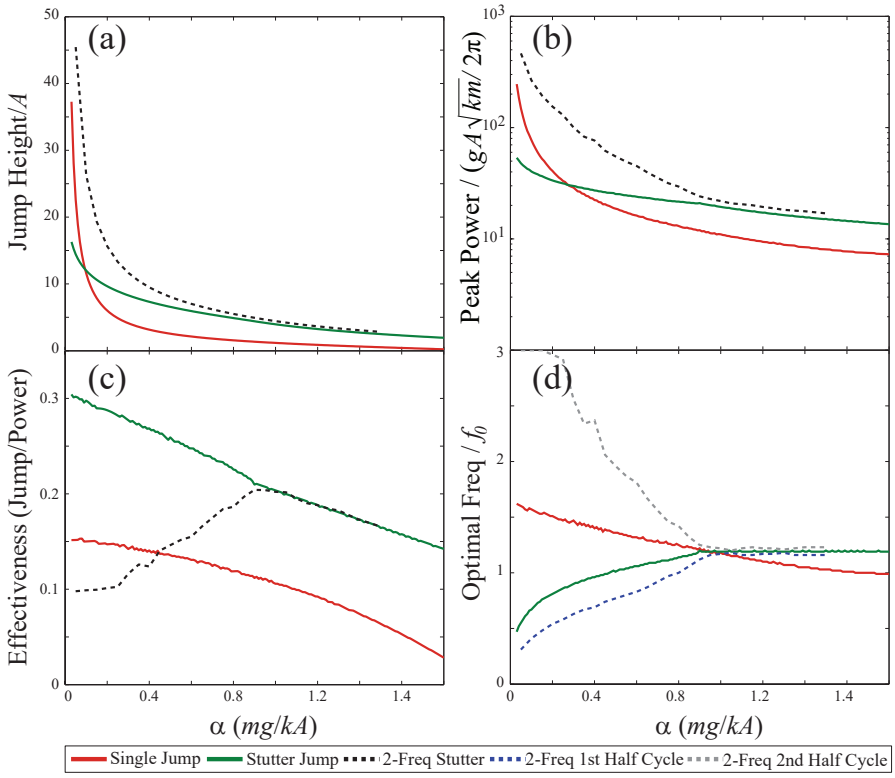

Figure 36: Two frequency stutter jump results (a) Relative jump heights vs alpha (b) Relative peak power vs alpha (c) Efficiency vs alpha (d) Optimal frequencies vs alpha.

larger percentage of the pull-up phase was spent in the air, which has an exclusively gravity dominated time-scale. This produced a greater disparity between the pull-up phase frequency and the push-off phase frequency (Fig 36(d)). As α approached 0.9, relative air time approached zero until both phases of forcing were optimal at the same frequency as the regular stutter jump due to the singular influence of the spring based time-scale. The increased jump height of the two-frequency stutter was due to the disparate frequencies - one lower than the stutter jump and the other higher than the single jump - maximizing spring compression. This increased compression was coupled with a high relative motor velocity during the high frequency push-off phase, which invariably produced peak motor powers that were also greater than either the stutter jump or single jump (Fig. 36(b)). These high peak powers significantly reduce the efficiency of the two-frequency stutter jump when compared with the regular stutter

jump until both jumps are identical for $\alpha > 0.9$ (Fig. 36(c)), at which point relative jump heights are already extremely low.

CHAPTER III

THE DYNAMICS OF JUMPING ON GRANULAR MEDIA

3.1 Summary

The locomotion of terrestrial animals or robots is typically studied in scenarios where either unyielding environments deform the locomotor or, conversely, where non-compliant locomotors deform yielding substrates. Such scenarios include animals[13, 37] or robots[172, 167, 121, 170, 46, 49] with body compliance during running or jumping on hard ground, as well as rigid robotic hexepedal locomotors that deform granular substrates[169, 129]. However, in many robotically[224] and biologically[127, 149] relevant situations like impulsive interactions during running and hopping, the deformable substrate and locomotor simultaneously affect each other's internal states.

Our group's previous work[127, 169, 129, 135, 133] has demonstrated that dry granular media forms an excellent substrate on which to study diverse locomotor behaviors. However, even in this well-studied system, little is known about locomotor dynamics during active impulsive interactions. Many studies of fixed-shape (non-locomoting) objects impacting and penetrating dry granular media have revealed reaction forces (F_{GM}) that can be described by

$$F_{GM} = F_p(z) + \alpha v^2, \tag{15}$$

where v and z are the object's velocity and depth, respectively [114, 199, 203]. The hydrodynamic-like term, αv^2, results from momentum transfer to the grains (significant during high speed impact [69, 164, 180, 26, 15, 73]), where α is the inertial drag coefficient. The hydrostatic-like force $F_p(z)$ results from frictional forces and typically scales as kz for submerged or flat intruders [199] for slow intrusions, where k characterizes the medium's penetration resistance. This hydrostatic-like term has recently

been extended to a granular resistive force theory (RFT), whereby forces are predicted on objects intruding relatively slowly (where inertial effects are negligible [166]) with different directions and orientations [129]. Such work has helped explain the kinematics of slow moving locomotors [129, 135, 133]. During high speed locomotion, recent studies of free impact in dense cornstarch solutions [211] and dry granular media [115] as well as rapid lightweight robot running on granular media [224] have shown the importance of hydrodynamic-like effects during high-speed interactions. One such effect includes added mass, which effectively increases the inertia of an intruder displacing material (see[45] for a review of added mass in fluids).

During such high speed movements, locomotors are often described by complex models [157, 220]. Yet even simple active-passive self-deforming objects (such as robots with both actuators and compliant springs) on hard ground can exhibit rich dynamics and provide insight into more complex systems. For example, the jumping performance of a 1D actuated spring-mass hopper is sensitive to its active self-deformation strategy, which induces motion coupled to both aerial and passive spring-mass dynamics [3]. We therefore posit that understanding the dynamics of rapidly self-deforming objects in complex media will require new insights into both nonlinear robot dynamics and soft matter physics when inertial effects are important. As such, in this Chapter, we discuss our expanded robophysical study of jumping (originally on hard ground publish in [3]) on dry granular media (published in [2]). However, forced impulsive interactions in granular media were not well understood. To gain new insights into the nonlinear dynamics governing jumping on sand, we systematically performed experiments that simultaneously probed the dynamics of both the robot and the granular media during jumping. Insights into new granular physics were gained from this study, such as an added mass effect induced by a granular cone that solidified under an impulsively intruding foot. These insights were further expanded and incorporated into a motion planning optimizer that was able accurately

produce desired jumping tasks in granular media.

3.2 Comparison of experimental and simulated jumping

To examine how the characteristics of jumping change on granular media compared to hard ground, we performed jumps on granular media using the strategies tested on hard ground: the single jump (Fig. 37(a)) and stutter jump (Fig. 37(b)). We additionally tested a delayed stutter jump (Fig. 37(c)), which includes a delay time between the pull-up phase and push-off phase of the stutter jump. For the delayed stutter jump, vibrational transients were eliminated by temporarily lowering the proportional positional feedback gain in the linear motor, producing an amplified damping effect in the spring vibration.

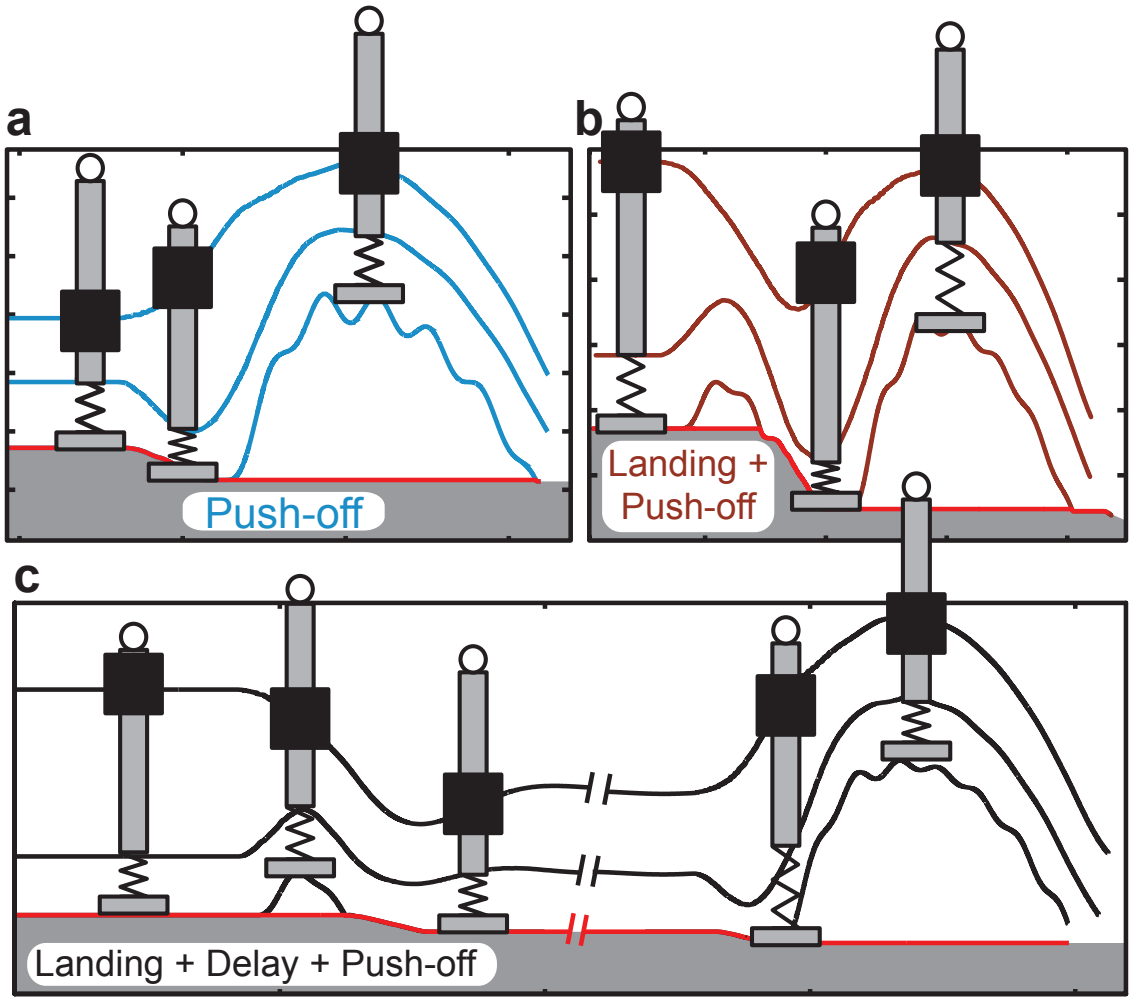

Figure 37: Simulated time series illustrations (of foot, rod and motor) show jumping trajectories for a push-off intrusion, or single jump (a), landing and push-off, or stutter jump (b), and landing, delay and push-off, or delayed stutter jump (c). Robot size scaled by $\sim 1/4$x for illustrative purposes.

The properties of jamming granular media depend on volume fraction, ϕ: dry grains transition from consolidative to dilative shearing behavior within a narrow range of volume fractions ($\phi = 0.57$ to 0.62), and their drag [83] and penetration [195] properties vary significantly. Thus, we expected that ϕ would play an important role in jump height. To characterize the role of ϕ, we systematically varied ϕ for all jump types.

We additionally compared results with a simulated model that included a granular force, F_{GM}, on the robot foot. We initially tested the simulation using the traditional relation from Equation 15. The static force, $F_p(z)$, was empirically determined.

3.2.1 Methods: Automated Granular Jumping Apparatus

We performed systematic experiments on a robophysics style jumping robot in a bed of poppy seeds (Fig. 38). The apparatus was fully automated, allowing for simultaneous robot control and data acquisition while sequentially exploring a parameter space.

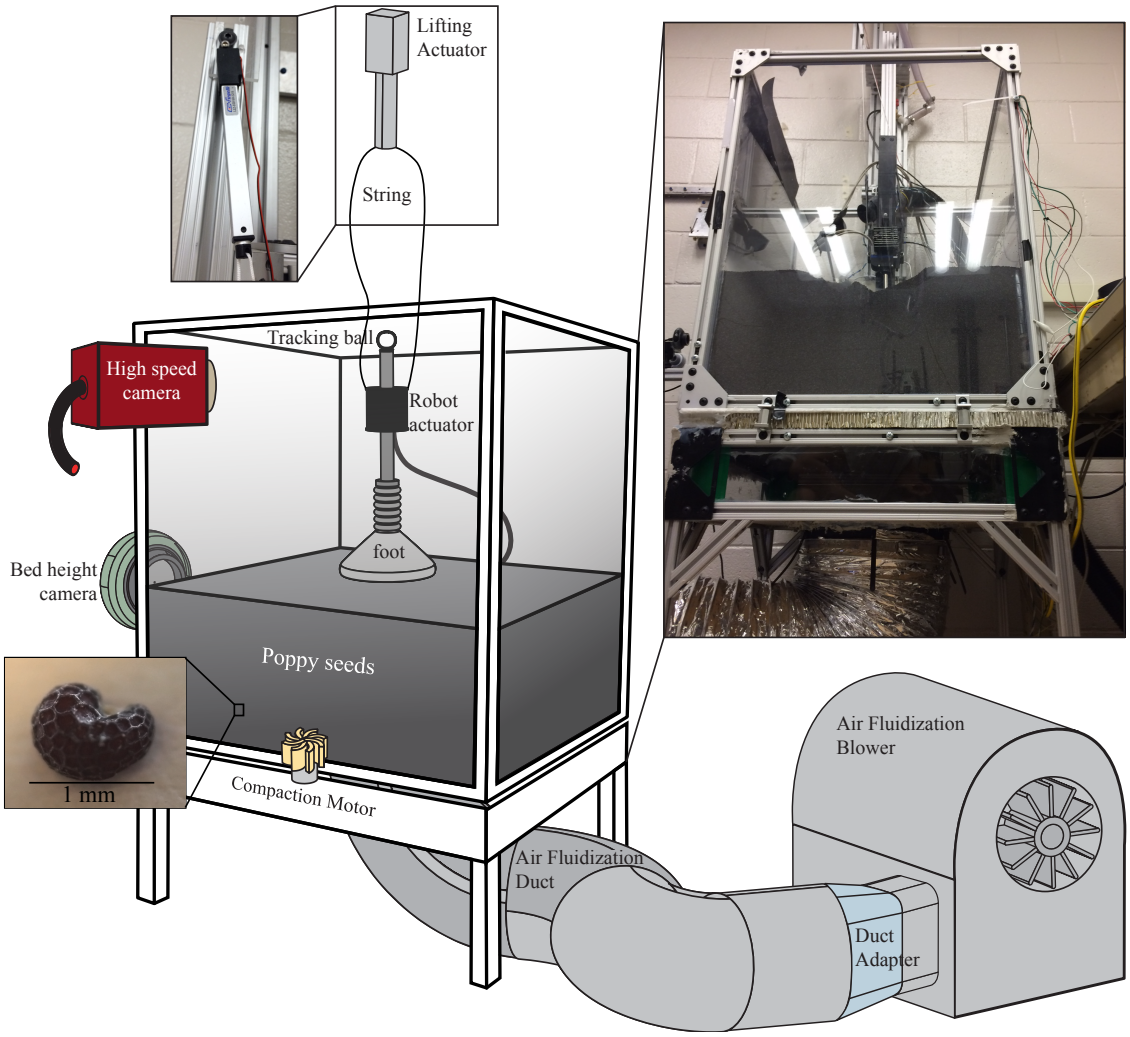

Figure 38: Automated granular jumping apparatus. A 56 cm x 56 cm area granular bed is filled with ∼1 mm diameter poppy seeds fill to a height of ∼ 25 cm. Volume fraction is controlled with a compaction motor and air pulses from a blower that fluidizes the grains, and the robot is constrained via an air bearing to jump vertically. A Firgelli linear motor lifts the jumping robot between experiments during the granular fluidization process. A webcam captures the height of the bed to measure volume fraction.

We used the same robot jumper as in hard ground experiments [3] (though oriented vertically instead of an angle). The actuator-air bearing carriage has a mass of 1.125 kg and comprises the majority of the robot mass. The bottom of the motor's thrust

rod is connected to a spring with stiffness $k_s = 3300$ N/m, which connects to a 7.6 cm diameter flat disc foot. To produce various jumping movements, the motor followed a one-cycle sinusoidal positional trajectory with an amplitude $A = 1.875$ cm. During jumping, a 9.5 mm white plastic ball fixed to the thrust rod was captured by a 200 fps camera to track rod position, and the jump height was calculated as the maximal rod position minus the initial rod position at rest. Due to the higher forcing amplitude used and increased reliance on the video tracking as compared to hard ground jumping studies (a contact sensor could not be used on granular media to quantify jumping performance), we took measures to mitigate the potential to lose tracking of the white tracker at high velocities. Aside from using a black background, we additionally fixed a 3D printed black piece to the thrust rod to hide the reflective metallic thrust rod surface from the high speed camera (Fig. 39).

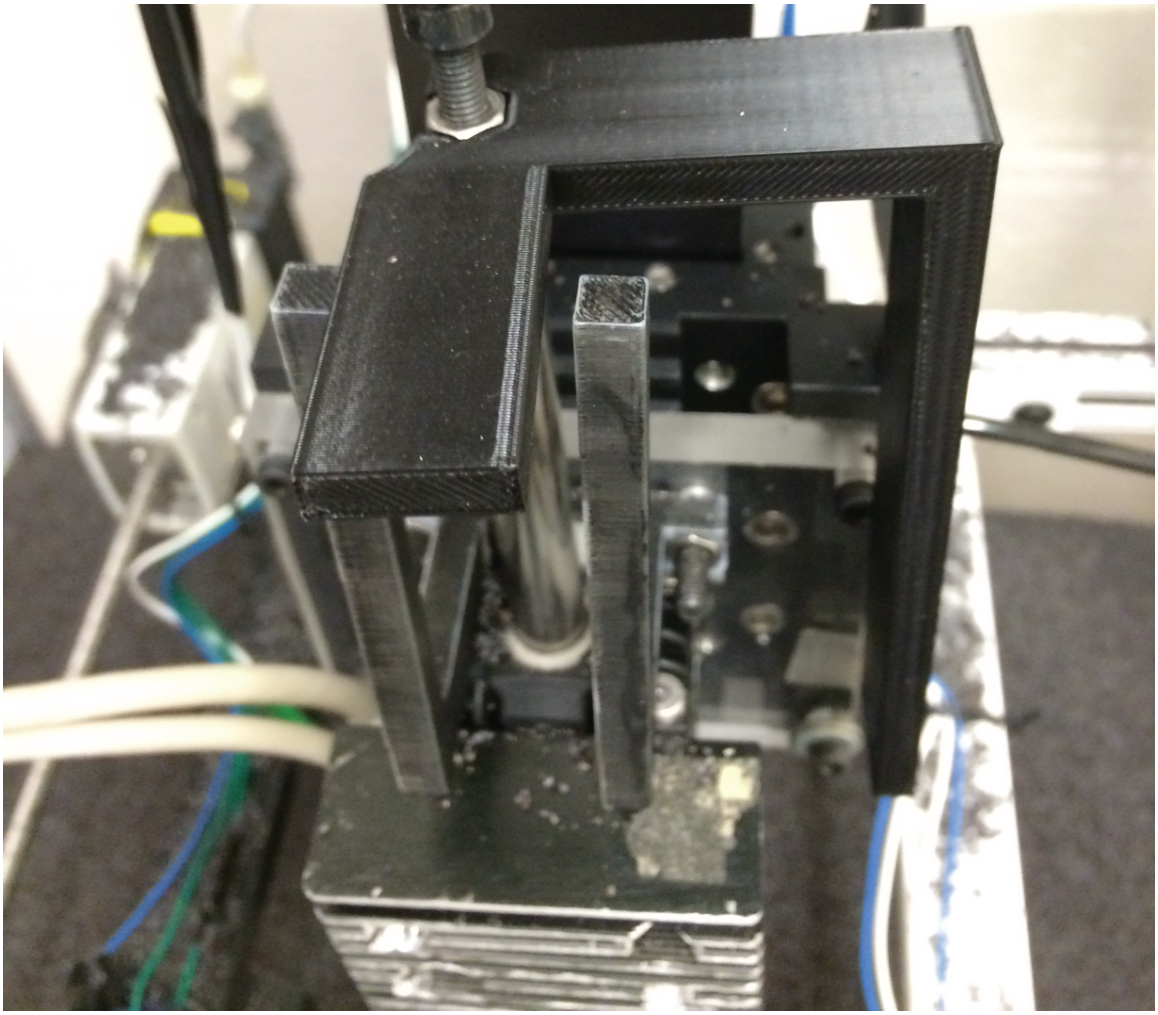

Figure 39: A black thrust rod adapter was used to block the reflective surface of the thrust rod from view of the high speed camera.

The entire robot/air bearing assembly was placed inside the bed (Fig. 38). The side walls were constructed from 1.9 cm clear acrylic plates. Grooves were cut at the edges to properly fit within the aluminum 80/20 frame. The dimensions of the bed and the amount of grains used were chosen to allow for a range of different size feet to be attached to the jumping robot without inducing wall effects and boundary effects in the granular media during jumping experiments. For example, in our experiments, the largest flat foot used had a radius of 3.81 cm. To avoid potential changes in the granular resistive force due to approaching the bottom of the granular bed, we chose a

granular bed height of approximately 25 cm (i.e. many multiples of the foot's radius). Such a bed height is uncommonly high in comparison to other locomotive experiments in poppy seeds from our group where no such boundary effects were observed during systematic intrusion force measurements [129]. As such, we argued that such a height was a safe overestimation of the required bed height.

However, such boundary effects have been probed in detail in a study [193] that examined how local jamming influenced hydrostatic-like forces on a plate intruding granular media within a vessel. Among the parameters varied in the intrusion experiments, vessel diameter, intruder size, and the height of the granular substrate were varied. As the intruder approached the bottom of the container, an exponential increase in the granular force applied to the intruder was observed that followed the functional form: $\Delta F(z) = A(1 - \exp[\tau(\zeta - z)])^2 - A$, where the bed height, $z = 0$, indicates the bottom of the container, A is intruder area, and the characteristic length, ζ, is the height of minimum $\Delta F(z)$. This characteristic length occurs near the bottom of the container where the bottom boundary would begin to influence the static penetration force. It was determined that, independent of the type of granular substrate (i.e. grain size) and assuming walls are sufficiently far away, $\zeta \propto \sqrt{F_o/r}$, where r is the intruder radius, and F_o is the force at the bottom depth of the container if there was no constraining boundary at that depth.

To obtain an estimate of ζ given our intruder size in poppy seeds with a bed height of 25 cm, we first calculated an approximate scaling factor, C, for $\zeta = C\sqrt{F_o/r}$ given the data from figures in [193] (particularly Figures 12 and 14). Then, we estimated F_o (for a bed height of 25 cm) by using empirical force relations obtained from our experiments in poppy seeds [2] (Fig. 48). For the purpose of our simple calculations, we approximated a linear depth relation following k_2 resistance at high volume fraction ($\phi \approx 0.625$, Fig. 48), yielding an approximate $\zeta \approx 9$ cm, which corresponds to an intrusion depth of about 14 cm. Maximum intrusion depths in our experiments ranged

from 2 to 3 cm in loose packed media and much less in close packed media.

Wall effects on granular forces were also studied in [193], which revealed that, for an intruder with a radius of 12.7 mm, vessel diameters greater than approximately 130 mm did not significantly induce a change in the force. However, only one intruder size was reported for the experiments varying vessel diameters. Another study [186] measured the penetration depth, δ, of a sphere impacting granular media where the relative sphere diameter, d, and cylindrical container diameter, D, were varied. For values of D/d greater than about 5, there was no significant change to the scaling of the power law that describes δ/d. The sides of our granular container were 56 cm in length, or about 7.3 times the diameter of the largest foot tested.

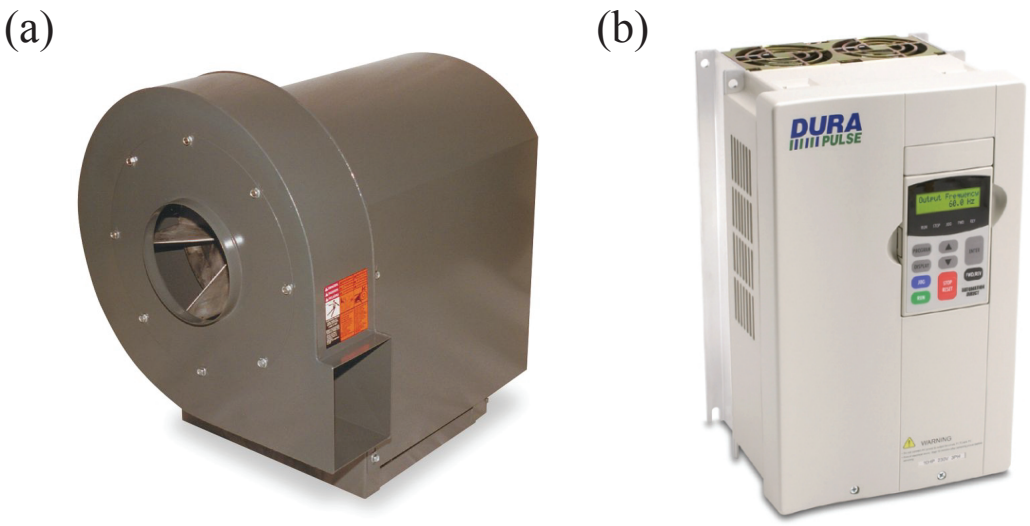

Figure 40: Fluidization fan. (a) Dayton 5 hp blower motor. (b) DURApulse AC drive blower controller.

To reset the state of the granular media and control volume fraction, the granular media was fluidized between jumping experiments by a Dayton 5 hp blower fan (Fig. 40(a)) with variable voltage flow control. To properly distribute the flow across the surface of the bed, a small chamber was built between the inlet and the bottom of the granular container. At the top of the chamber (opposite the inlet of the duct,

i.e. bottom of the granular bed) was a 1 inch thick layer of aluminum honeycomb for structural rigidity and flow distribution, on top of which was a Porex porous plastic sheet. The blower was controlled with a DURApulse AC drive controller (Fig. 40(b)). This controller was programmable and allowed for both manual control of fan RPM as well as proportional voltage control of RPM. To automate the experiment, RPM was controlled through Labview with a variable analog 0-5 V signal sent from a National Instruments USB 6009 DAQ (which consequently was also used to control all other automated components such as the shaker motor and lifting motor).

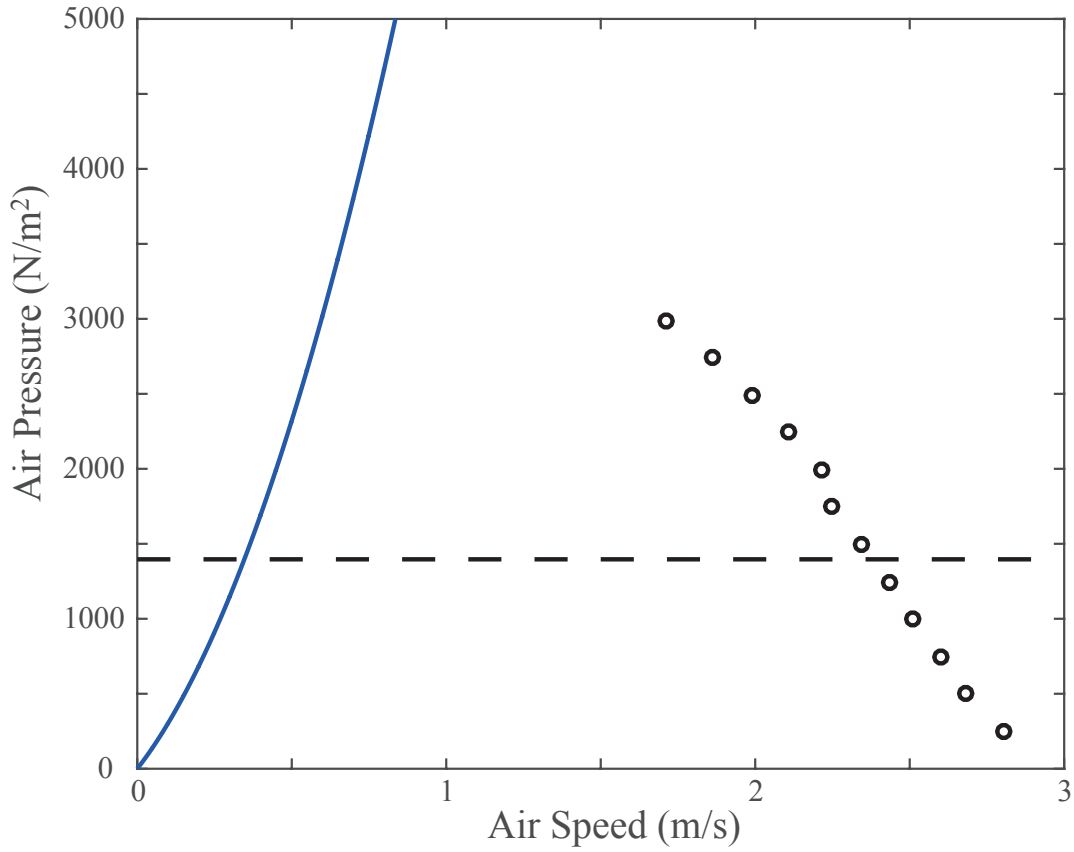

Figure 41: Comparison of the theoretical pressure drop (using a model described in [217]) through granular substrate vs superficial air speed (blue solid line) and static pressure of Dayton blower fan for at different air speeds through granular bed (black circles). Dashed line indicates the pressure of the granular media due to the weight of the grains.

The blower was selected mainly by trial and error such that the rated horsepower of the blower was sufficient to fluidize the granular media. The blower required enough power to produce a pressure drop through the granular media to overcome the weight of the grains. In fluidization applications, the pressure drop through a granular substrate is related to the fluid flow rate through the media by a model that describes the resistance to flow through a porous material. The most commonly used

of these models is Ergun's 1952 equation [67]:

$$\frac{\Delta P}{L} = \frac{150\mu(1-\epsilon)^2\nu}{d^2\epsilon^3} + 1.75\frac{1-\epsilon}{\epsilon^3}\frac{\rho\nu^2}{d}, \tag{16}$$

where ΔP is the pressure drop from the bottom to the top of the granular bed, L is the bed height, μ is the dynamics viscosity of the fluid, ρ is the fluid density, ν is the superficial airspeed (flow rate over the cross-sectional area of the bed), d is average grain diameter, and ϵ is porosity ($\epsilon = 1 - \phi$, where ϕ is volume fraction). The outer scaling terms were empirically determined. This equation relates the pressure drop due to both kinetic and viscous energy loss, such that it is predictive at both high and low Reynolds numbers. Wu et al. [217] developed a similar model which had no empirical scaling constants:

$$\frac{\Delta P}{L} = \frac{72\mu\tau(1-\epsilon)^2\nu}{d^2\epsilon^3} + \frac{3\tau(1-\epsilon)\rho\nu^2(1.5+\beta^{-4}-2.5\beta^{-2})}{4d\epsilon^3}, \tag{17}$$

where the tortuosity, τ, is approximated as a function of ϵ in [40] (and reproduced as Eq. 4 in [217]). The pore to throat diameter ratio, β, is derived from a simplified pore-throat model of granular media and is calculated as $1/(1-\sqrt{1-\epsilon})$. Plugging in values from our setup produced similar values of pressure drop using both equations. Equation 17 (Fig. 41) dictates that the required air speed to overcome the weight of the granular substrate and produce fluidization is about 0.35 m/s, which was verified with anemometer readings. Comparing this pressure drop equation to the rated air speeds at which the blower operates for various static pressures (Fig. 41, black circles) reveals that there is no reported data for the static pressure that would produce 0.35 m/s air flow in the blower. Furthermore, the static pressure for the blower includes more than just the pressure drop through the granular media; it also includes the pressure drop at the turns in the duct as well as through the honeycomb flow distributor and Porex porous material at the bottom of the bed. This increase in static pressure would further reduce the flow rate output of the blower. The operating airspeed would theoretically be the point in which the static pressure curve (Fig. 41,

black circles) and the curve of pressure drop vs airspeed (which would also include all other sources of pressure drop) intersect. If the pressure at this point is greater than the gravitational granular pressure, then fluidization would occur. However, though sealant was used to great effect, due to the design of the fluidized bed, we still observed air leaks throughout the bed that were difficult to control and monitor. This inevitably also reduced the flow rate going through the granular media. One challenge in properly routing airflow from the blower to the granular bed was properly mating the blower outlet (which was incomprehensibly rectangular) to standard circular duct tubing (Fig. 42). A custom designed adapter had to be printed in five separate pieces (the design was too big for the 3D printing chamber) and assembled, which was difficult to fully seal. In the end, a 5 hp blower was required to operate at full power to produce consistent and repeatable fluidized states and volume fractions.

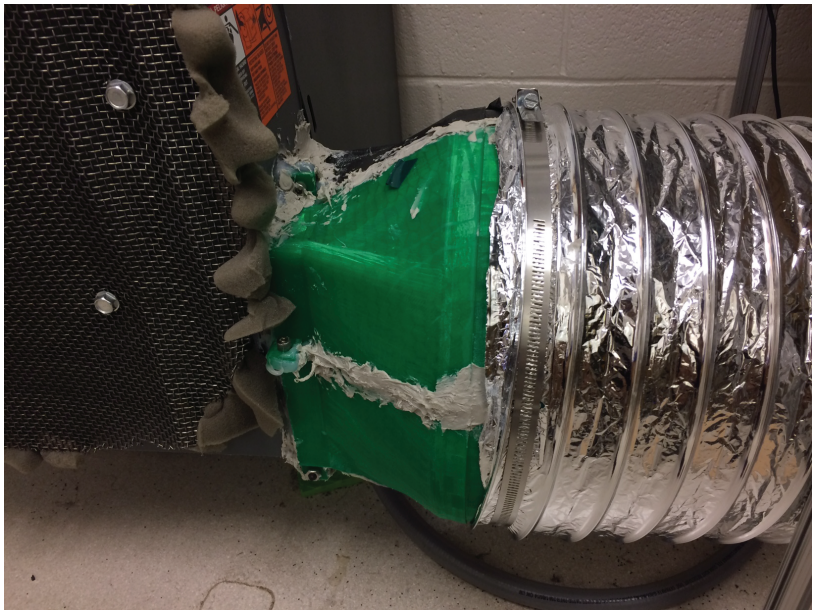

Figure 42: A 3D printed adapter was designed to mate the blower with the duct.

The fluidization process reset the state of media from previous disturbances and produced a loose-packed state with volume fraction, $\phi \approx 0.57$. Producing higher

compactions consisted of modulating air-flow rate below onset of fluidization to produce air pulses while simultaneously activating a shaker motor that vibrated the bed. Volume fractions, measured with a camera that captures granular bed height, ranged from 0.57 to 0.62. The webcam captured an image of the side of the granular bed (Fig. 38) after the fluidization process. From within Labview, the image was automatically processed through a routine of intensity thresholding, determining regions of black and white, and performing several iterations of image dilation and erosion to eliminate noisy pixels (Fig. 43). White paper and a fluorescent strip light were placed on the opposite side of the bed to enhance contrast with poppy seeds. This processed image was then used to detect that average height of the poppy seeds. Volume fraction, ϕ, is the ratio of the collective volume of individual grains vs the volume the grains occupy in bulk. Given a certain amount of grains, N, that fill the bed and the known dimensions (length, l, and width, w) of the bed, the granular bed height, h, was sufficient to calculate volume fraction ($\phi = \frac{N\pi r^2}{lwh}$, r is average grain radius). We additionally explored the use of ultrasonic range finders to measure bed height, but concluded that image capture was more reliable, since it took an average value instead of bed height at a single location on the granular surface.

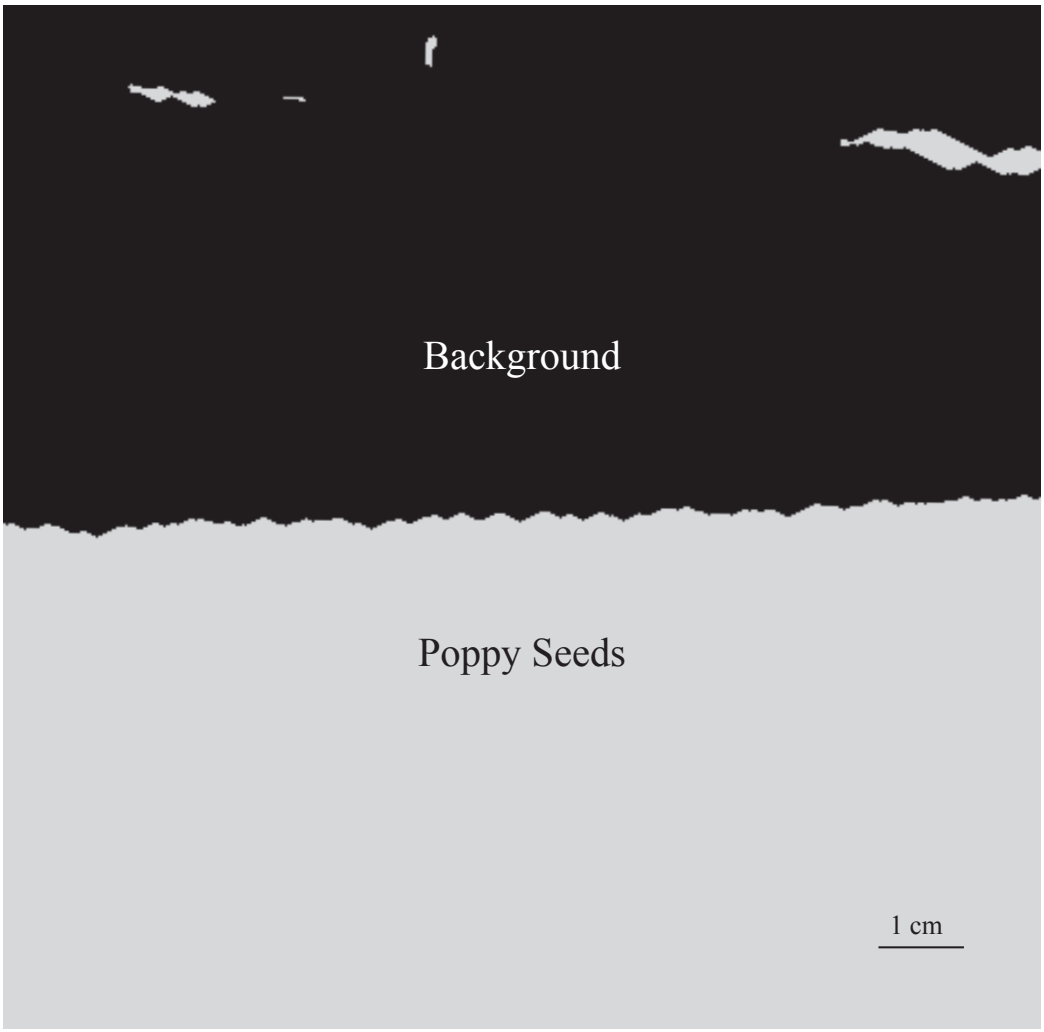

Figure 43: A sample processed image from the camera that captured the level of the poppy seeds.

Between jumping experiments, a linear motor lifted the jumping robot via a string attached to the carriage of the air bearing (Fig. 38) to prevent the robot from sinking during the fluidization/granular preparation process. The Firgelli motor had a maximum extension length of 10.16 cm. The supplied extension length and the length of the string were selected to allow for the jumping robot to be lifted with sufficient clearance from the fluidizing granular media while also providing sufficient slack while jumping such that jumping dynamics were not obstructed.

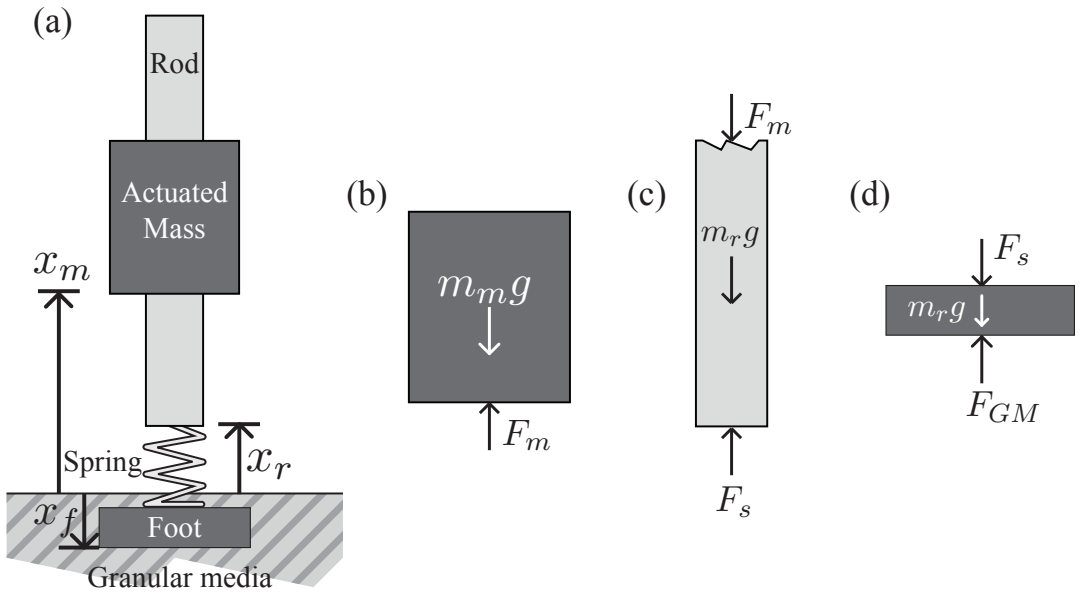

Figure 44: Diagram of the theoretical model on granular media. (a) Overall granular substrate model. Free body diagrams of the (b) actuated mass, (c) rod and (d) foot.

3.2.2 Methods: Simulated Jumping Model on Granular Media

To compare experimental jumps with simulation, we numerically integrated the robot's equations of motion based on a simple model (Fig. 44):

$$m_m \ddot{x}_m = -m_m g + F_m, \tag{18}$$

$$m_r \ddot{x}_r = -m_r g - F_m + F_s, \tag{19}$$

$$m_f \ddot{x}_f = -m_f g - F_s + F_{GM}, \tag{20}$$

where the subscripts, m, r and f corresponding to motor, rod and foot quantities, respectively. The rod and motor equations were combined as

$$M \ddot{x}_r = -Mg + F_s + m_m(\ddot{X}_m), \tag{21}$$

where $M = m_m + m_r$, and the $\ddot{X}_m = \ddot{x}_r - \ddot{x}_m$. A granular force, F_{GM}, was applied to the foot. As in the hard ground simulations (Section 2.2.2), the numerical integration scheme was performed using Simulink. To compare directly with experiment, we used

experimental encoder positions from each experimental jump performed to obtain the $\ddot{X}_m$ command for simulation. The granular force, F_{GM}, followed the various relations discussed in this Chapter, and the spring force, F_s, followed Hooke's law for the spring between the rod and foot. Another property of F_{GM} was its hybrid dynamic dependence on the discrete transition of the foot between the ground and air phases (i.e. $F_{GM} = 0$ during aerial phase). The ground position changed as the foot intruded and was set to the foot's position while the foot was grounded. During the robot's aerial phase, the ground maintained the last foot position before transition to the aerial phase. For hard ground simulations (Section 2.2.2), it was sufficient to utilize the variable time-step ODE45 integrator to avoid Zeno effects and accurately detect hybrid transitions. However, on granular media, the changing ground position can cause perpetual Zeno-like behavior unless proper conditions are established for determining the transition from the ground to aerial phase.

A naive approach is to state that the foot becomes aerial when the total force on the foot causes the foot to accelerate from a negative to positive velocity. However, this caused constant Zeno-like switching between the ground and air phase and was only accurate for extremely small integration time-steps. An understanding of the nature of the different forces is required to obtain the proper transition conditions. Ground reaction forces, or F_{GM} in this case, are merely capable of resisting downward motion, and not producing propulsive upward motion. Thus, even if $\dot{x}_f = 0$ and $\ddot{x}_f > 0$, the foot remains grounded and foot speed remains zero at the next time step if the spring is still compressed and pushing down on the foot ($-F_s - m_f g < 0$). To become aerial, the foot must be pulled off the ground by the spring ($-F_s - m_f g > 0$), rather than pushed off by the ground. This condition eliminated Zeno effects while achieving output results identical to the small time-step approach, yielding faster simulation.

3.2.3 Results and Discussion

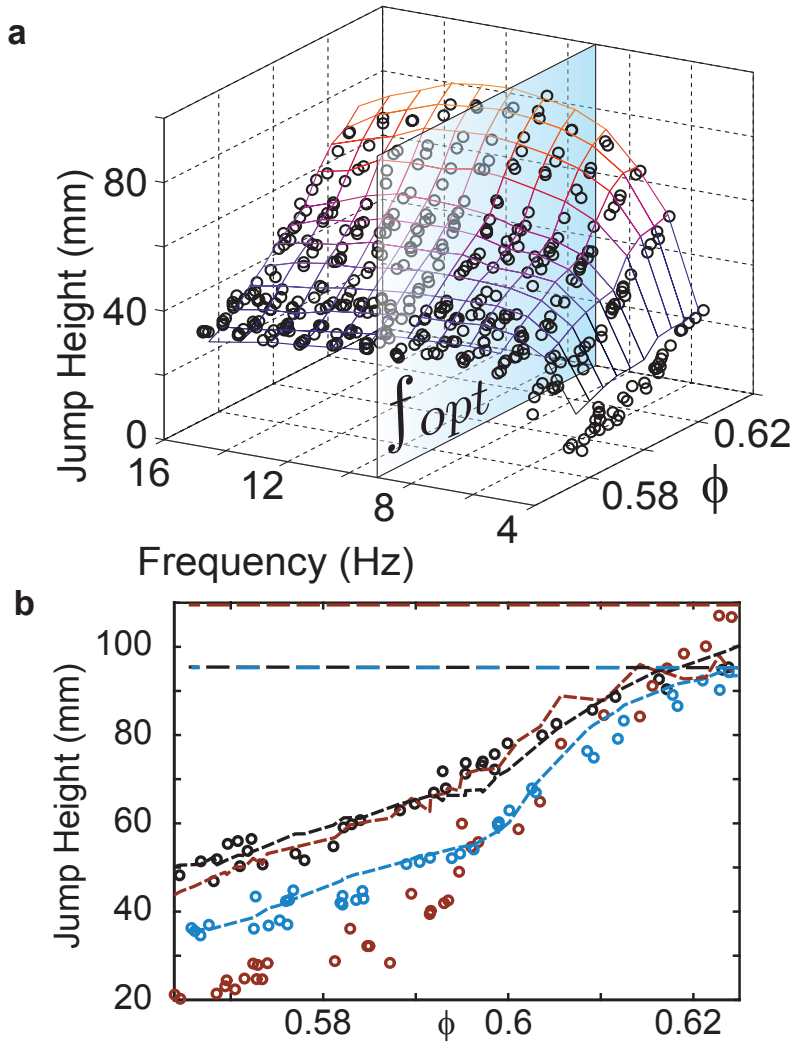

Figure 45: Jump heights for various self-deformations. Each jump type is produced with a sine wave at optimal frequency determined from a larger sweep of forcing frequencies. (a) Experimental (black circles) and simulated (color mesh grid) jump heights of single jumps for different forcing frequencies and ϕ. (b) Experimental jump heights at optimal forcing frequency (f_{opt} determined according to highest jump at high ϕ) (circles) vs. ϕ compared with 1D simulation (dashed lines) results using the traditional granular force relation, Equation 15 (and the 2-resistance re-intrusion relation for $F_p(z)$), for single jumps (blue), stutter jumps (maroon), and delayed stutter jumps (black). Hard ground jump heights are indicated by horizontal dashed lines.

Similar to hard ground experiments, we tested the role of forcing frequency (where, as in hard ground experiments, the relative motor position of each jump was prescribed a single cycle sine wave trajectory at a specific frequency), and, for single jumps, we observed a broad range of frequencies that produced jump heights near the height of the optimal frequency (Fig. 45(a)), similar to single jumps on hard ground [3]. Experimental results of the single jump, which consisted of a single push-off phase (Fig. 37(a)), revealed that jump height was sensitively dependent on ϕ (Fig. 45(b)). For example, at optimal forcing frequency, a 5 percent reduction in ϕ reduced jump performance to approximately one third of the hard ground jump height. There was a particularly sharp dependence to changes in ϕ near $\phi \approx 0.605$. This volume fraction is near the critical packing state in glass beads, $\phi_c \approx 0.60$ [83]. The critical packing state is the volume fraction in which granular media transitions from consolidative behavior under shear in loose packed granular media to dilative behavior at high compactions. We performed tests to approximate this volume fraction in poppy seeds by dropping a metal ball into poppy seeds at different ϕ (Fig. 46). Using a laser line, we captured the cross-sectional shape of the resulting crater, and, assuming azimuthal symmetry, we calculated the resulting volume change of the granular media. The transition from negative to positive volume change determined $\phi_c \approx 0.61$. However, this experiment was performed in a smaller granular bed before our larger experimental apparatus was constructed; ϕ was calculated based on an assumed low volume fraction of 0.58 at a certain bed height, where bed height measurements were used to scale from this initial measurement. Based on our most recent jumping and intrusion experiments, it is likely that ϕ_c was closer to 0.605.

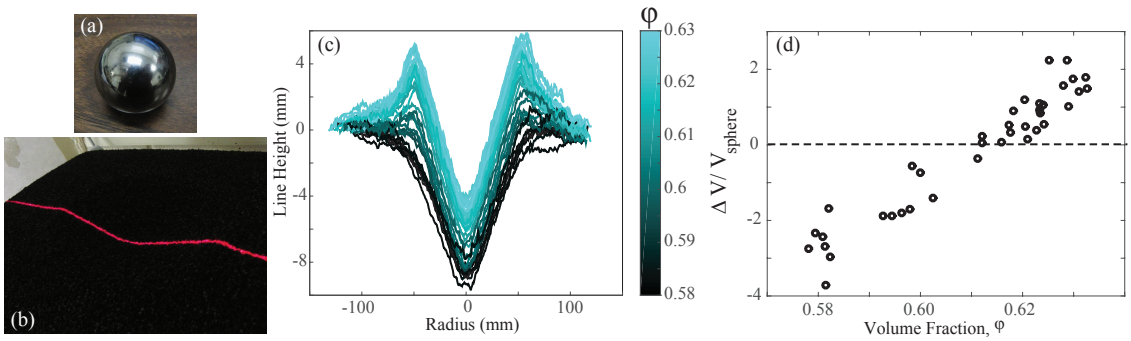

Figure 46: Determining the critical packing state. A (a) metal ball was dropped into a (b) bed of granular media. (c) The cross-sectional shape of the resulting crater was capture with a laser line and camera. Assuming azimuthal symmetry of the crater, (d) we used the crater's cross-section to calculate the volume change of the granular media.

Our previous study of jumping on hard ground demonstrated that the stutter jump, consisting of a preliminary hop landing followed immediately by a push-off (Fig. 37(b)), outperformed the single jump while requiring lower peak actuation power[3]. We tested its efficacy on sand, hypothesizing that a preliminary hop would precompact the ground, increasing granular reaction forces and improving jump heights at low ϕ. Surprisingly, this jump yielded lower heights than the single jump at low ϕ (Fig. 45(b)).

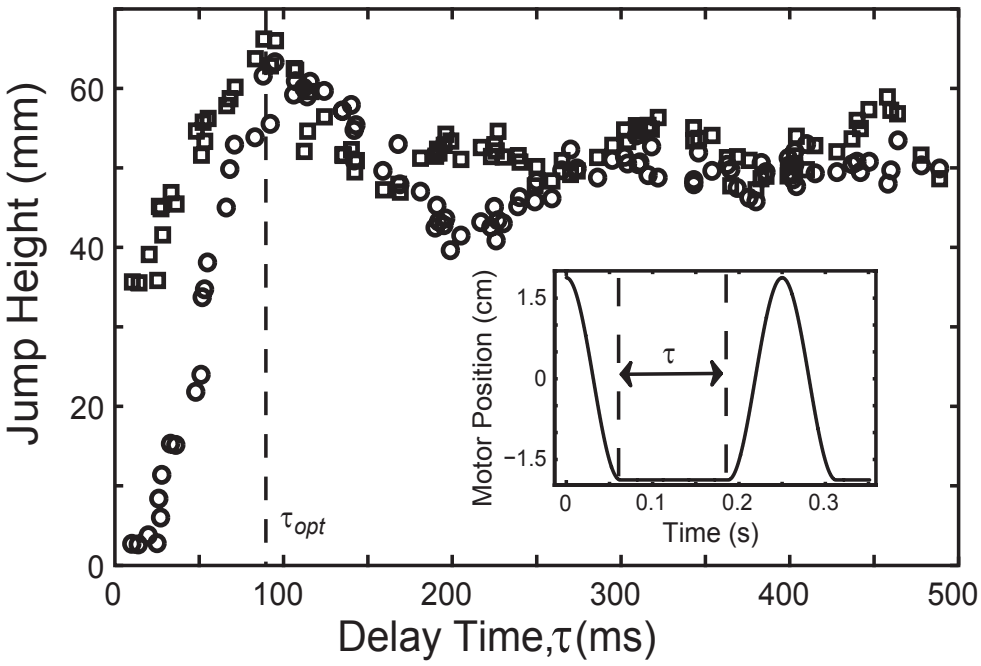

Figure 47: Delayed stutter jump heights for various delay times. Experimental (circles) heights compared with 1D simulation (squares) results using the traditional granular force relation, Equation 15 (and the 2-resistance re-intrusion relation for $F_p(z)$) of delayed stutters in loose poppy ($\phi = 0.57$) agree for delay times, $\tau \geq \tau_{opt}$.

To eliminate potential transient dynamics preventing the media from relaxing into a compacted state, we introduced a delay time of $\tau = 0.75$ seconds between the pull-up phase and push-off phase of the stutter jump (Fig. 37(c)). The delay not only improved stutter jump heights (measured with respect to initial rod height), but surpassed the single jump at low ϕ (Fig. 45(b)), suggesting that the best way to jump on loose granular media is by enhancing the single jump with a properly timed preliminary hop, locally compacting the substrate. Indeed, measuring jump heights from after the preliminary hop revealed that low ϕ delayed stutter jumps resembled single jumps compacted to ϕ_c and higher. Varying τ at low ϕ revealed an optimal delay time, τ_{opt}, near 100 ms (Fig. 47). This time scale represents a 5 Hz

half cycle oscillation, which is near the robot's spring-mass resonance. The natural frequency is near 8 Hz on hard ground, and, during foot intrusion, is reduced at low ϕ to approximately 5 Hz, since the robot gains an effective one-way series spring - the k_1 penetration resistance of $F_p(z)$. Thus, the timing of an optimal delayed stutter jump is determined by a combination of the robot's spring-mass dynamics and the transient settling of the granular media during local compaction.

We compared experimental jumps with a numerical model of the robot jumper in which the foot experiences granular forces, F_{GM}. Since little was known about the complex granular interactions of self-deforming passive/active intruders, we first applied Equation 15 for F_{GM} using a linear relation for $F_p(z)$. Fitting simulation to experimental jump heights with a constant α and constant k yielded parameter values that were inconsistent between different jumping strategies. Also, previous experiments for slow penetration revealed that, while $F_p(z)$ was approximately linear with depth[129, 195] away from boundaries[192, 193], the relationship between $F_p(z)$ and z was nonlinear near the surface. Thus, we chose to empirically determine $F_p(z)$ by systematically performing slow-intrusion force vs. depth measurements (Fig. 48(a)) at various values ϕ. To obtain these intrusion force measurements, we repurposed the robot's linear motor. With the motor clamped securely to the bed, the spring was removed from the rod and foot, and the rod was connected directly to the foot and slowly forced at constant speed into poppy seeds at various ϕ. Force and depth measurements were attained from motor current and encoder position, respectively. We used both 5.1 cm and 7.6 cm diameter flat feet and found that F_p scaled proportionally with foot surface area.

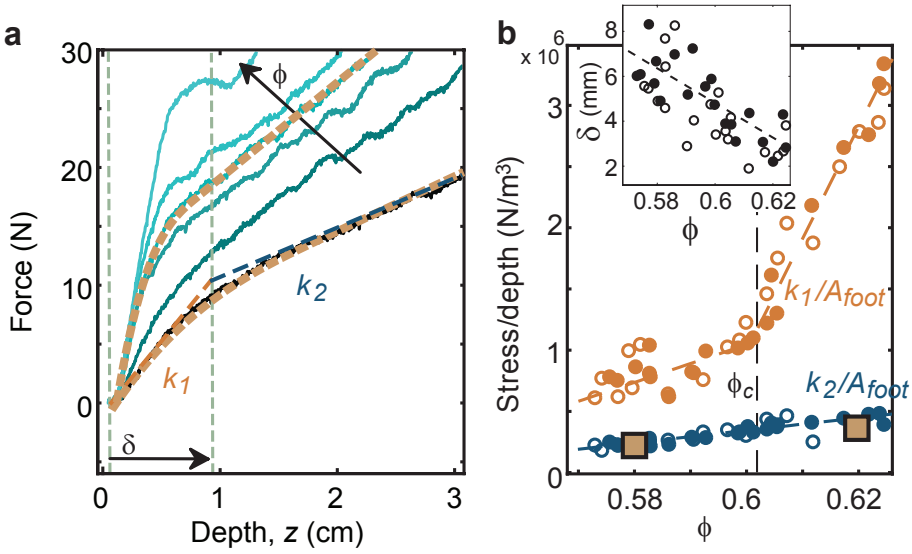

Figure 48: Empirical measurements of force vs. intrusion depth. A 5.1 cm diameter (a, b solid circles) and 7.6 cm diameter (b open circles) flat foot were tested for increasing ϕ (black to light blue in a). Transition depths, δ, between low and high penetration resistance vs. ϕ are displayed in inset in (b). Empirical estimates of k_1/A_{foot}, RFT measurements for angled intrusions[129] and a model of granular cone jamming were combined to predict force vs. depth at $\phi = 0.58$ and $\phi = 0.62$ (a, brown dashed curves). Stress vs. depth for fully developed cones accurately predicted the k_2/A_{foot} penetration resistance at low and high ϕ (b, brown squares), where A_{foot} is the foot surface area.

These slow-speed intrusion measurements revealed a nearly linear depth-dependence at low ϕ that became increasingly nonlinear for higher ϕ. We modeled this as two constant penetration resistance coefficients, k_1 and k_2, where k_1 was the slope of a linear fit of $F_p(z)$ near the surface, and k_2 was the slope at deeper intrusion (Fig. 48(b)). Near the granular critical packing state, ϕ_c, k_1 transitioned to a greater sensitivity to increasing ϕ. While the values for k_2 showed no transition at ϕ_c, the k_2 regime ($z > \delta$) exhibited an onset of force oscillations at ϕ_c which steadily increased with ϕ, consistent with shearing dynamics observed in drag[195, 83] experiments.

Implementing the two-penetration resistance relation and a constant α in simulation was essential for agreement with experiment; using a linear $F_p(z)$ relation yielded inaccurate simulation results.

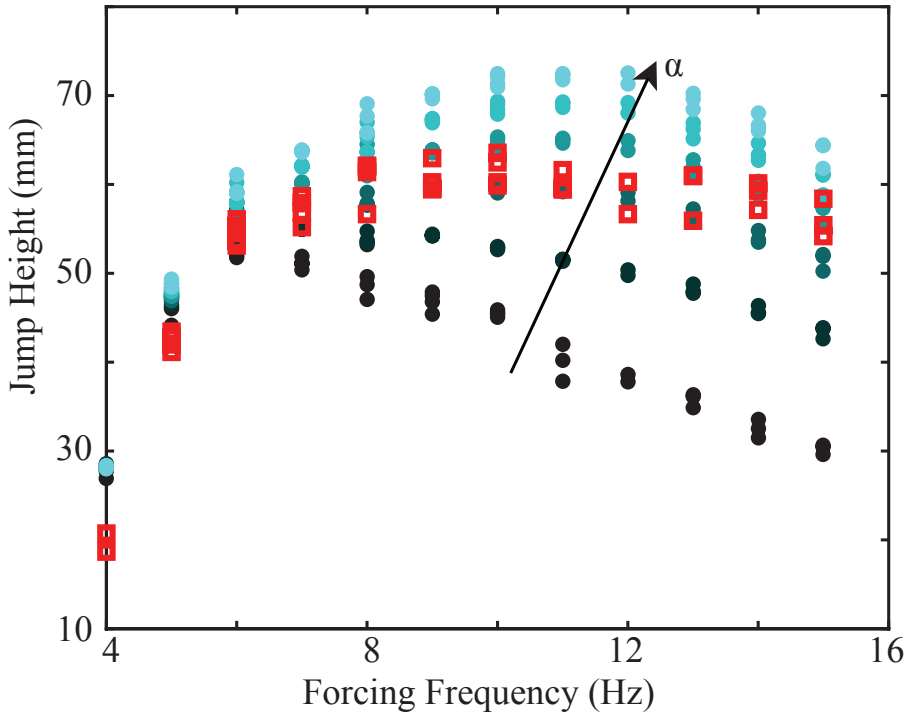

Figure 49: Fitting depth-independent inertial drag coefficient, α. Single jump simulation of increase values of α (circles, α increases from 0 N(m/s)$^{-2}$ (black) to 300 N(m/s)$^{-2}$ (light blue)) and experimental (squares) jump heights vs motor forcing frequency at $\phi = 0.60$.

To determine a constant (depth-independent) α at each ϕ, we systematically varied α while simulating single jumps at each ϕ and compared simulation jump heights at different forcing frequencies to experimental single jump heights at various forcing frequencies (Fig. 49). Jump heights were most sensitive to α for high forcing frequencies, as expected since higher frequencies induced higher intrusion speeds. Fits of α vs. ϕ revealed a similar scaling with ϕ as k_1: a higher $d\alpha/d\phi$ was observed for $\phi > \phi_c$. This fit of α with a two-resistance empirical $F_p(z)$ yielded good agreement between

simulation and experiment single jumps. These ϕ-dependent values of α were then used when simulating the other jumping strategies.

However, a comparison of simulation and experiment of delayed stutter jumps and stutter jumps revealed poor agreement for the α fits and the original empirical two-penetration resistance form $F_p(z)$. To determine if modification to $F_p(z)$ was needed due to reintrusions, we performed reintrusion measurements by intruding the thrust rod at slow velocities to a certain depth, extracting, and then reintruding (Fig. 50). Upon reintrusion, we observed a sharp rise in force to a peak that was higher than the expected force according to the original two-resistance force relation. This led to a new formulation of $F_p(z)$ according to the observed reintrusion force behavior that had a force overshoot proportional to the depth of reintrusion. To attain the correct reintrusion parameters, we performed a fitting process similar to the fitting process described to find α at different ϕ, leading to simulation agreement with both single jumps as well as delayed stutter jumps with delay times $\tau \geq \tau_{opt}$. However, this model did not explain the poor performance of the regular stutter jump: the simulation showed agreement at high ϕ, but over-estimated the stutter jump heights at low ϕ (Fig. 45(b)). This deviation was particularly evident for delayed stutter jumps with $\tau < \tau_{opt}$ (Fig. 47), suggesting unaccounted for transient granular dynamics preventing the media from relaxing into a compact state.

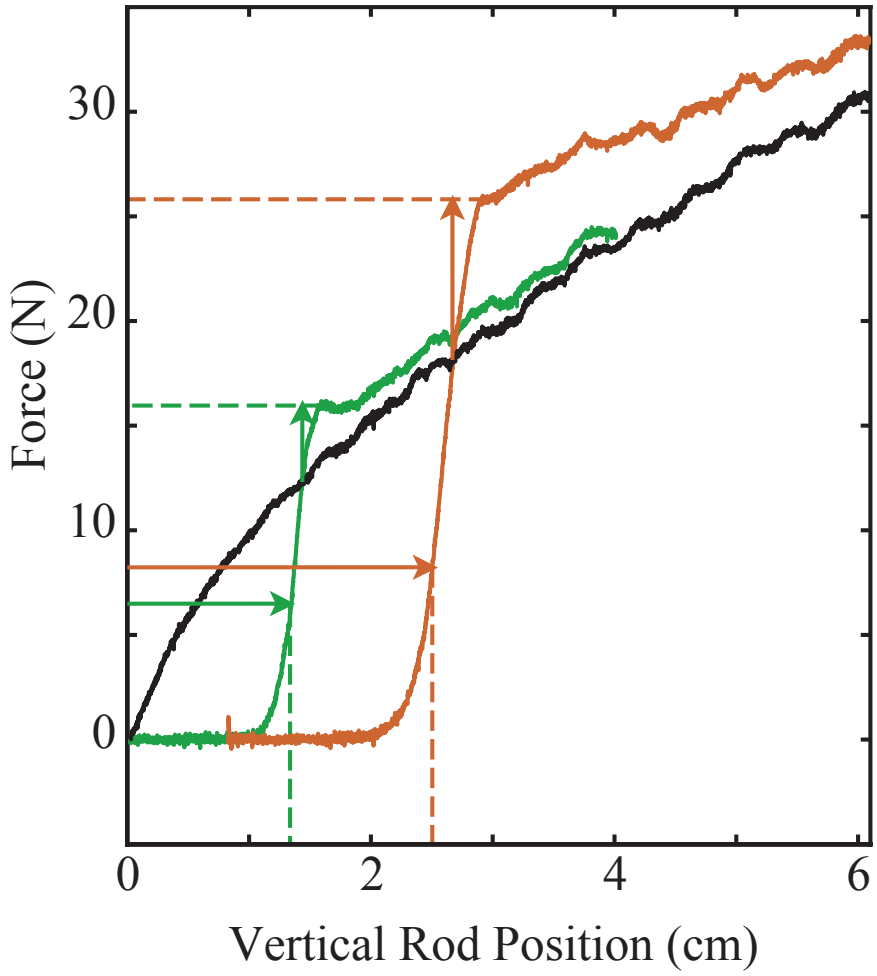

Figure 50: Measuring slow-speed reintrusion forces. Force vs depth measurements at $\phi = 0.57$ during slow velocity reintrusions with a 6.4 cm diameter disk foot at 2 different reintrusion depths. Horizontal arrows indicate the reintrusion depth for the force curve of the corresponding color. Likewise, vertical arrows indicate the force overshoot from the original force vs depth curve with no reintrusion (black) for the force curve of the corresponding color.

3.3 Evolution of jammed granular cone

Thus far, we have measured $F_p(z)$ and made assumptions about the form of the hydrodynamic-like force, αv^2, based on models in previous literature. However, we

posited that a joint analysis of the granular and robot dynamics would provide insight into the mechanism that lowered the peak height of stutter jumps. We next discuss how measuring granular flow kinematics during jumping provided insight into these dynamics, which, when incorporated into our 1D jumping model, revealed the mechanism for altered jumping performance.

3.3.1 Methods: PIV analysis of granular flow

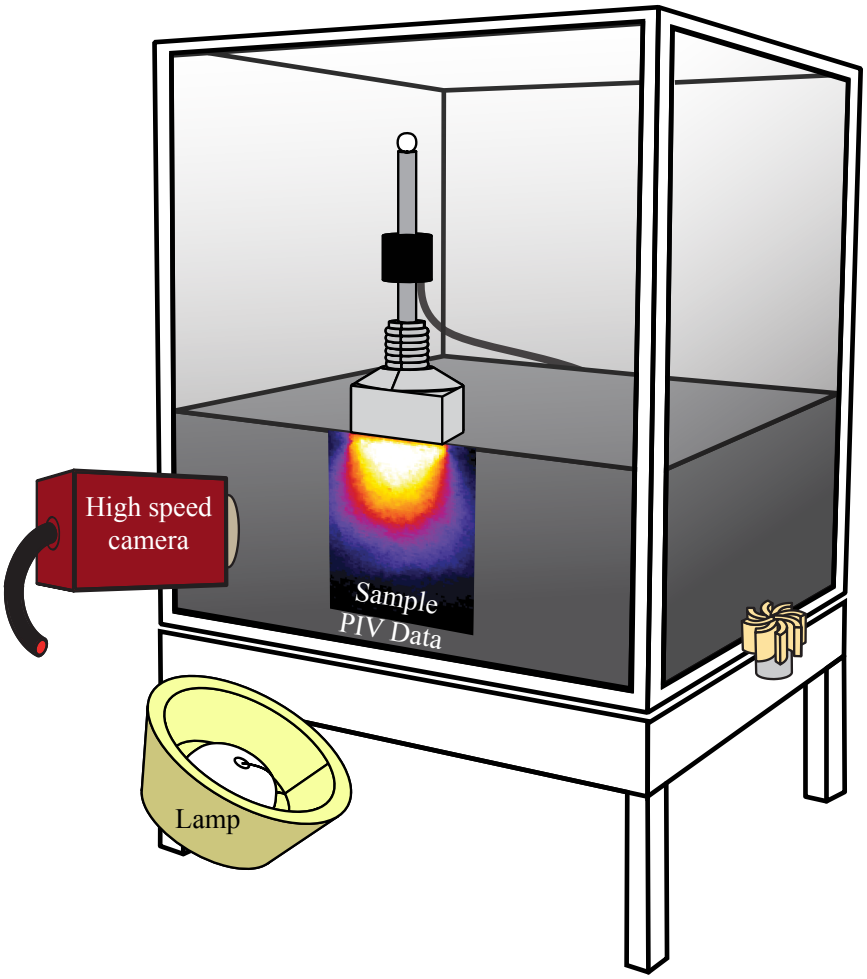

Figure 51: Diagram of granular bed for experiment capturing granular flow kinematics during jumping. Jumping robot was moved to the side wall with a foot that mates flush with the wall. A lamp illuminates the poppy seeds while a high speed camera captures the flow of the poppy seeds during jumping. Particle image velocimetry (sample vertical velocity colormap is displayed below robot foot) takes high speed image data and measures granular flow kinematics.

We moved the robot from the center of the granular bed to the clear acrylic side wall (Fig. 51), and, using a foot with a flat side, we had the robot perform all 3 jump strategies for a sparse sweep of volume fractions and recorded high speed video (500

fps AOS camera at 1280 x 1024 resolution) of the sidewall grain flow. Jump heights did not deviate significantly from jump heights at the center of the bed (away from wall effects). We performed a particle image velocimetry (PIV) analysis on these videos. No tracer particles were necessary, since poppy seed images provided a sufficiently large and well mixed distribution of grey-scale intensities among grains. The PIV analysis compared divided each video frame into a grid of pixel windows. Each window of each frame was compared with the following frame, where a correlation analysis determined the local velocity vector of the grains within the window. Thus a velocity vector field of the granular flow was produced for each frame.

3.3.2 Results and Discussion

In conjunction with the measured velocity field, we used the PIV measurements to calculate the shear strain rate field, $\dot{\gamma}$,

$$\dot{\gamma} = \sqrt{\frac{1}{2}\left(\frac{\partial u}{\partial x} - \frac{\partial v}{\partial y}\right)^2 + \frac{1}{2}\left(\frac{\partial u}{\partial y} + \frac{\partial v}{\partial x}\right)^2}, \tag{22}$$

where u is horizontal velocity and v is vertical velocity (Fig. 52(b)). We observed triangular shear bands (long boundaries of high localized shear) that were similar to other granular compression experiments and simulations[124]. Combined with vertical grain flow (Fig. 52(a)) and the PIV vector field (Fig. 52(b)), these shear bands illustrate how, as the foot enters the media, a cone of effectively solidified grains (outlined by the shear bands) rapidly develops underneath the foot. Moving at similar downward speeds as the foot; this cone wedges surrounding material away.

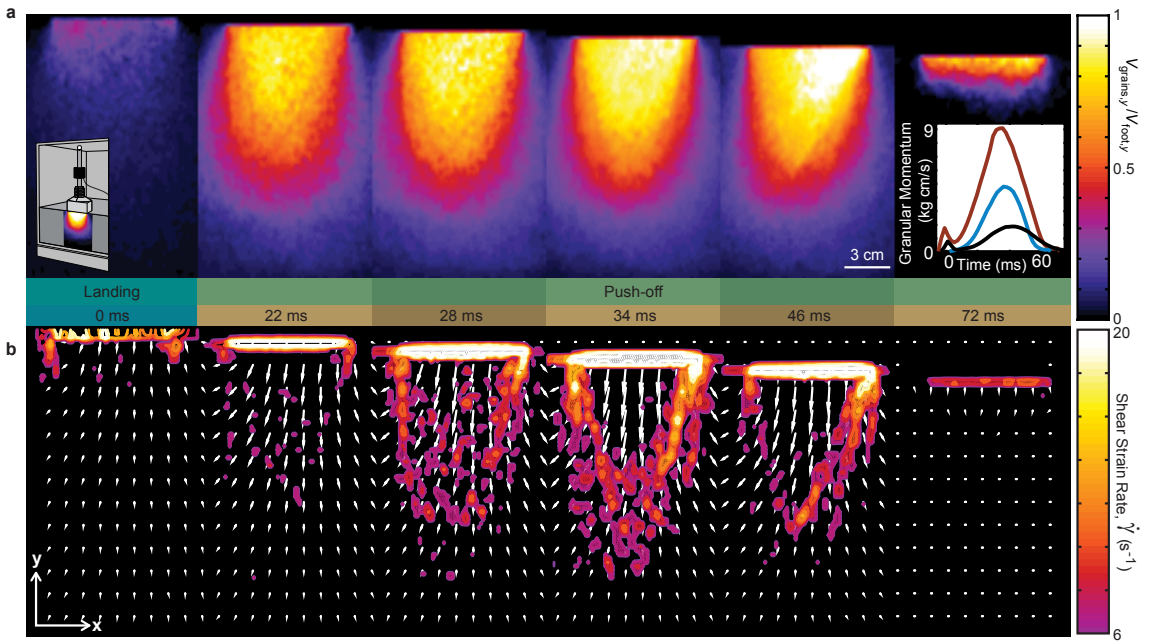

Figure 52: Particle Image Velocimetry (PIV) measurement of granular flow kinematics. (a) Frame sequence of the downward velocity field, normalized by foot speed, taken during the landing and push-off phase of a stutter jump at $\phi = 0.57$ (left inset, diagram of setup). Right inset, Time sequence of granular momentum calculated from PIV for single (blue), stutter (maroon) and delayed stutter (black) jumps at $\phi = 0.57$. (b) PIV vector field of same snapshots superimposed by shear bands derived from the shear strain field according to Equation 8. Shears bands illustrate how a cone of jammed grains rapidly emerge below the foot and wedge through surrounding material.

To illustrate the geometric evolution of the cone jamming phenomenon, we developed a simple discrete element model (DEM) of 2D disks interacting. Grain-grain interactions consisted of a simple Hooke's law spring repulsion, zero friction, and viscous damper repulsion, which allowed for inelastic collisions. While we instituted a simplification of zero grain-grain friction, we introduced individual grain friction (like grains sliding on carpet) to prevent excessive inertial motion (which would resemble a

billiards simulation), allowing for a more geometric analysis of cone evolution. A flat object was approximated by "intruder grains" that move with a prescribed trajectory and apply similar grain-grain interaction forces on other "free" grains. Accelerations were integrated using an explicit forward Euler integration scheme.

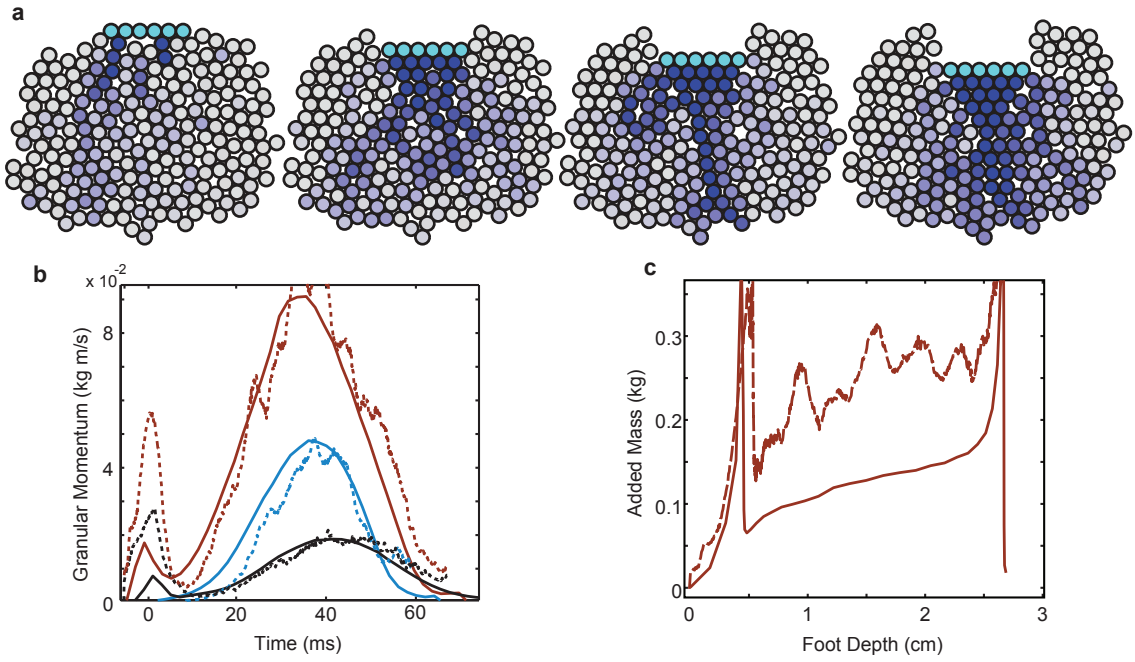

Figure 53: DEM Analysis of granular cone. (a) Visualization of sequential frames (left to right) of 2D DEM simulation during foot (teal grains) intrusion. Grains are colored according to downward speed relative to intruder, blue being 100 percent foot speed. (b) Time sequence of granular momentum calculated from PIV (solid) and a simple 2D discrete element method (DEM) granular simulation (dashed, scaled by 0.5) for single (blue), stutter (maroon) and delayed stutter (black) jumps. (c) Added mass vs. depth calculation from PIV (solid) and DEM simulation (dashed) for a stutter jump.

The simulation revealed a similar triangular jamming front as that found with PIV experiment (Fig. 53(a)) and shear bands observed in other compression experiments[124].

Use of monodisperse grains produced crystallizing (a feature of monodisperse spherical particles [75, 57]) triangles resulting from 60° shear bands. Similarly forming triangles emerged without crystallizing lattices using both bidisperse and polydisperse particles. A simple 2D DEM provided an intuitive illustration of how grains jam with the foot through local crystallizations which shear sides as each layer of grains is deceased in length by one grain (Fig. 53(a)).

Motivated by these flow field kinematics, we derived a geometric model of the cone's development as a flat circular intruder plows vertically into particulate media (Fig. 54). In this model, the depth of a jammed front of grains moving with the foot grows proportionally by μ with intrusion depth, z (where the depth, z, is the negative of the foot position, x_f relative to the undisturbed surface of the granular substrate). In the 1D analogy of a line of grains that collide inelastically (as introduced in[211] to describe the speed of a jamming front during rapid intrusion in a colloidal suspension), the rate, μ, is inversely proportional to the separation distance between each grain relative to grain size. In dry granular media, all grains are already in contact with other grains before intrusion begins; there is no separation distance between grains. Thus μ describes the rate of growth of the jamming front, or the rate at which grains settle into a locally compacted solid-like state. As the foot descends and the granular cone grows, the radius, r, of the flat portion of the cone decreases due to the angle, θ, of the shear bands according to,

$$r = \frac{R\tan\theta - \mu z}{\tan\theta}, \tag{23}$$

where R is the foot's radius. Thus, the surface areas of the flat portion of the cone, A_{flat}, and conical surface, A_{cone} decrease according to,

$$A_{flat} = \pi\left(R^2 + \left(\frac{\mu z}{\tan\theta}\right)^2 - \frac{2R\mu z}{\tan\theta}\right). \tag{24}$$

$$A_{cone} = \frac{\pi R^2 - A_{flat}}{\cos\theta}. \tag{25}$$

While the shear bands fluctuated in time ($\pm 4°$), as observed in a previous plowing PIV experiment[83], θ at low ϕ was approximately 60°.

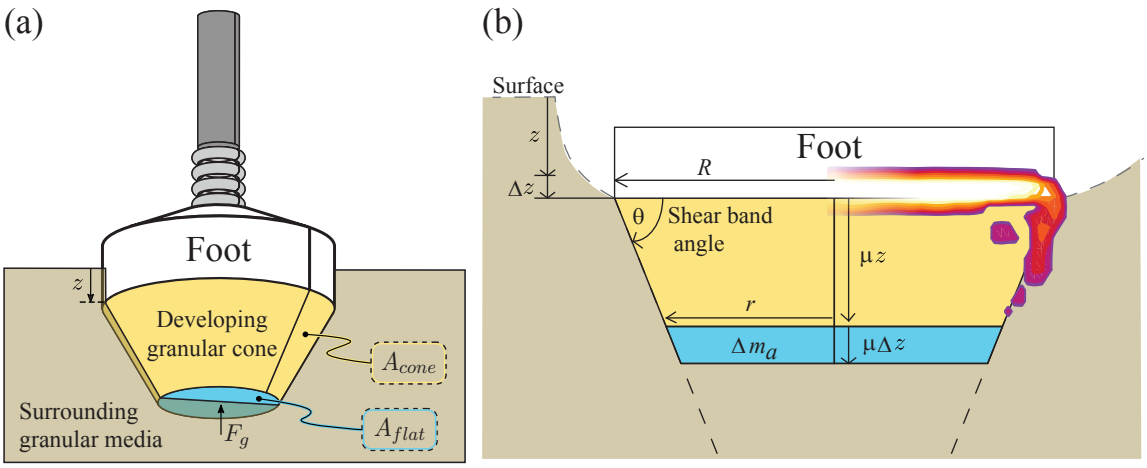

Figure 54: Diagram of developing granular cone. (a) 3D representation of the developing cone. As the foot intrudes, the total surface area of the developing compacted granular structure is comprised with more of the conical surface area, A_{cone}, and less of the flat surface area, A_{flat}, as the cone fully saturates and shears through and wedges away surrounding granular material. (b) A 2D geometric illustration of granular cone evolution versus intrusion depth. For a given differential increase in intrusion depth, Δz, the cone fills in by a proportional depth of $\mu \Delta z$, where μ is the rate of growth of the jamming front. An added-mass model of this cone takes into account a solidified conical core (yellow) as well as extra virtual mass, C, from slower moving grains surrounding the cone. The conical angle, θ, is estimated from the angle of shear bands from PIV shear strain (superimposed).

We hypothesized that this jammed cone extended the volume of the intruder from a flat disc to a conical wedge. A resistive force theory model (RFT) proposed by Li et al. [129] suggests that such a change in intruder shape affects the vertical quasistatic reaction force, $F_p(z)$. Quasistatic RFT forces are determined by taking an intruder of arbitrary shape moving through granular media with a specific direction

vector, and performing a linear superposition of the forces acting on small individual surface elements of the intruder. To determine the RFT forces of a given substrate, one develops an empirical map of stresses acting a small flat plate that is intruded at different angles of orientation, θ_1, and directions of motion, θ_2. To test our hypothesis of an evolving intruder geometry, we combined the empirical RFT model for poppy seeds [129] with our geometric model of cone development and estimated $F_p(z)$ as the summation of the quasistatic forces acting on the flat surfaces and conical surfaces of the extended intruder (illustrated in Fig. 55):

$$F_p(z) = F_{p,flat}(z) + F_{p,cone}(z). \tag{26}$$

Li et al. [129] performed systematic intrusion measurements to develop RFT stress maps for poppy seeds. As such, for the quasistatic force on conical surfaces, $F_{p,cone}(z)$, we utilized the vertical RFT stress from [129] for 60° conical surfaces (30° surface normal) intruding vertically ($\sigma_z(30°, 90°)$):

$$F_{p,cone}(z) = \sigma_z(30°, 90°) \int A_{cone}(z)dz. \tag{27}$$

RFT requires an assumption that forces and granular flows acting at any given location on an intruder are decoupled and do not affect the forces acting at any other point on the intruder. As such, forces determined from RFT typically assume fully developed flow. For this reason, we did not use RFT stresses for flat surfaces ($\sigma_z(90°, 90°)$); instead, we used our own empirical measurements of the initial slope of $F_p(z)$ (the k_1/A_{foot} penetration resistance, Fig. 48).

$$F_{p,flat}(z) = \frac{k_1}{\pi R^2} \int A_{flat}(z)dz. \tag{28}$$

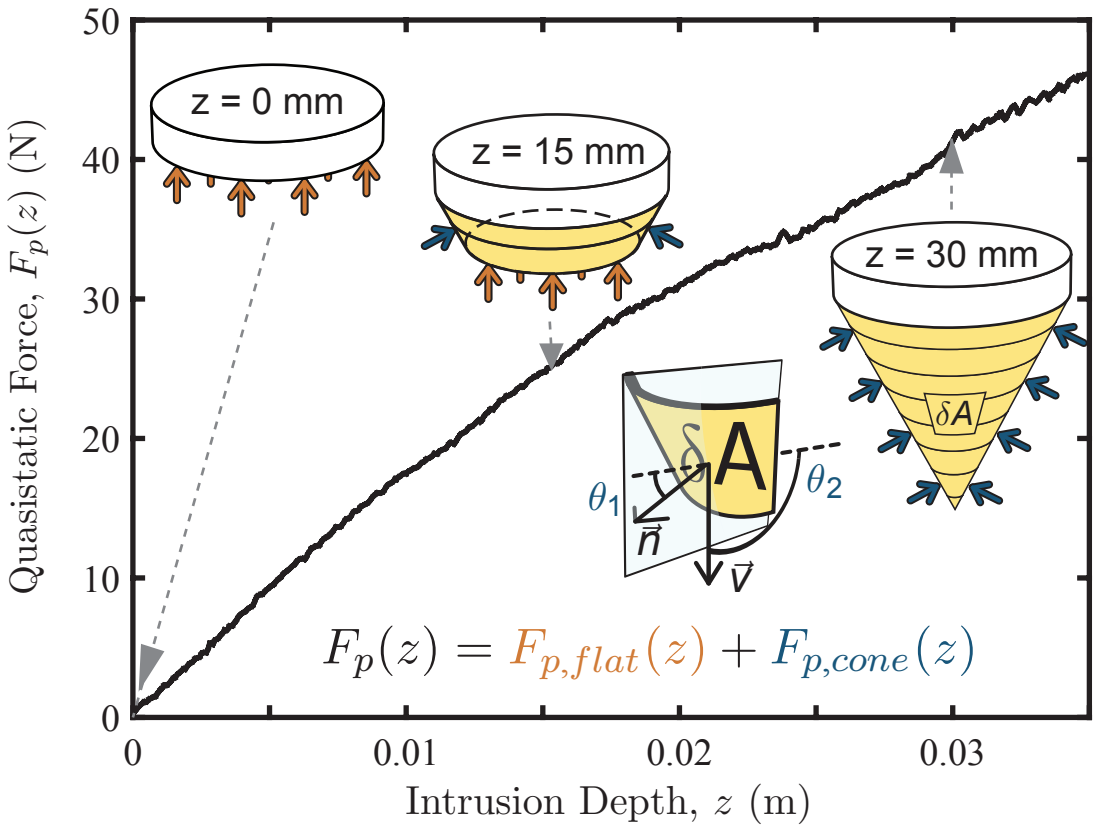

Figure 55: Description of RFT cone force model. Data shown is a sample of experimentally measured quasistatic force, F_p, vs intrusion depth, z, for a foot with radius, $R = 3.81$ cm at $\phi = 0.57$ (similar to data shown in Figure 48(a)). The RFT cone estimation of $F_p(z)$ is determined by summing the contributions to the quasistatic force from both flat and conical surfaces as the cone develops, where the slope is defined empirically as the initial slope, k_1, for $F_{p,flat}(z)$ (Equation 28), and is based on empirically determined RFT stresses for $\theta_1 = 30°$ angled surfaces moving downward ($\theta_2 = 90°$) for $F_{p,cone}(z)$ (Equation 27). Once the cone is fully developed, the slope of the curve remains constant according to $F_{p,cone}(z)$.

By selecting proper values for μ, calculating RFT forces on the evolving geometry of this granular cone captured the nonlinearity in empirical measurements of $F_p(z)$

(Fig. 48(a, brown dashed curves)). The effective stress per unit depth for a fully developed cone, $\iint_{cone} \sigma_z(30°, 90°)\delta A/A_{foot}$, coincided with k_2/A_{foot} values at low and high ϕ (Fig. 48(b, brown squares)). Such insights helped explain the phenomenon of rapidly diverging values of k_1 and k_2 for $\phi > \phi_c$. Flat intrusions displace grains predominantly through normal stresses that increase at higher ϕ, where the substrate is rapidly approaching a jammed state. Above ϕ_c, grains cannot consolidate as readily due to reduced mobility. As a result, flat intrusions cause individual grains to compress, and the material stiffness of the grains becomes a component of the k_1 penetration resistance. Once the cone forms, the intruder produces lateral grain displacements and shear stresses. As ϕ increases, more grain-grain frictional contacts during shearing result in an increase in k_2. However, for $\phi > \phi_c$, k_2 is not as large as k_1, since shear stresses do induce as much material compression as normal stresses.

An additional consequence of the RFT cone model was that the cone is fully developed once $\mu z = R \tan\theta$, such that the saturation depth was dependent on the size of the intruder. To test this size dependence on the saturation depth, we performed force vs. depth measurements at $\phi = 0.57$ for different size intruders (3 trials each for R = 1, 2, 2.54 and 3.175 cm and 6 trials each for R = 0.5 and 3.81 cm) and compared with theoretical force curves (Fig. 58). For a proper comparison, we calculated an estimate for μ using simplified, principled assumptions about how grains consolidate and jam. For a given intrusion distance, Δz, the cone gains a jammed layer of grains of thickness proportional to the intrusion distance, $\Delta z_{jammed} = \mu \Delta z$. Thus, μ can be thought of as the ratio $\Delta z_{jammed}/\Delta z$. Prior to the Δz intrusion, this layer of grains would be unjammed at some initial average volume fraction (we tested intrusions in loose packed media, $\phi = 0.57$). Once the layer jams, the volume fraction of the layer will have increased. We argue that this volume fraction may be near the critical packing state, $\phi_c \approx 0.605$, since any further shearing would require dilation, and compressive forces rapidly rise. Thus, assuming minimal loss of grains,

the relationship between the jammed and unjammed layer heights would be

$$\Delta z_{unjammed} = \frac{\phi_c}{\phi} \Delta z_{jammed}. \tag{29}$$

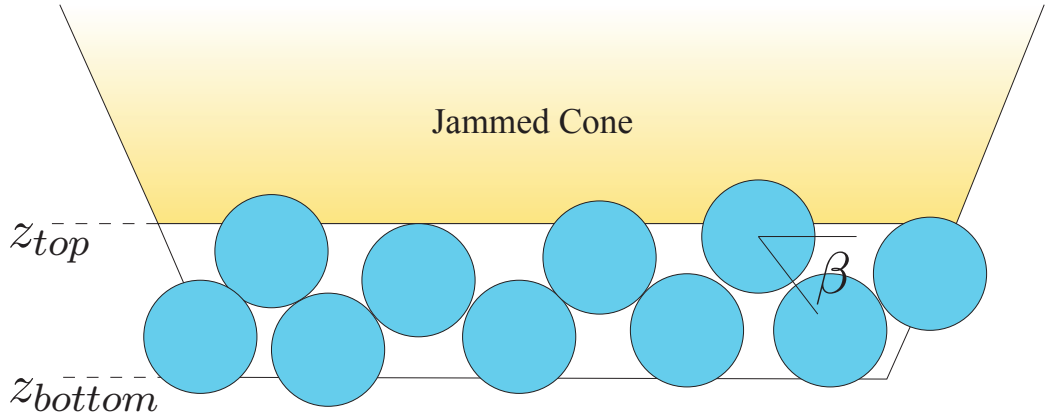

Figure 56: Diagram of simplified jamming with spherical frictionless grains. The jammed cone pushes the top of the initially unjammed layer, which has an initial layer thickness of $\Delta z_{unjammed} = z_{bottom} - z_{top}$. We define an average angle, β, relative to the horizontal axis that each grain makes with its neighboring grain below.

To determine how fast the unjammed layer compresses to a jammed state, we assumed a simplified model of frictionless spherical grains (Fig. 56) and investigated how the bottom of an unjammed layer displaces as the top is displaced. If we consider two grains in contact, the top grain displaces the bottom grain according to their relative angle of contact, β. For example, if both grains are positioned on the same vertical axis ($\beta = 90°$), the bottom grain displaces the same amount as the top grain when the top grain is displaced vertically. However, if $\beta = 60°$, then the bottom grain will displace by $\sin 60°$ of the top grain's displacement as the top grain slides past. Thus, for the simplified case of an uncompressed bilayer of grains, $\Delta z_{bottom} = \sin(\beta) \Delta z_{top}$, where β is the average angle of contact, and $\Delta z_{top} = \Delta z$. A study [22] that experimentally examined the angle distribution between common neighbor particles in granular

packs of acrylic spheres revealed that grains tended to produce regular tetrahedral configurations with their neighbors. For a jammed layer at ϕ_c, we argue that grains will tend to produce these tetrahedral configurations, and that such configurations will likely be orientated in the preferential jamming direction (vertically). Thus, according to the geometry of regular tetrahedra, $\beta_{jammed} \approx 54.72°$. However, as grains slide past one another, β will be changing, and, in the more disordered unjammed state, we argue that β will be larger according to the relative change in layer thickness, $\beta_{unjammed} = \sin^{-1}(\frac{\phi_c}{\phi}\sin(\beta_{jammed})) = 60.08°$. For simplicity, we assumed an average constant angle during the jamming process, $\beta = (\beta_{jammed} + \beta_{unjammed})/2 = 57.41°$.

This description of granular compaction suggests that, during an intrusion event, all unjammed layers will be sequentially compressed at a fractional rate relative to the adjacent layer above, such that downward grain speed follows an exponential function with respect to its layer depth: $\dot{z}_{grain} \propto \sin(\beta)^{z_{grain}}$, where z_{grain} is in units of layers (assuming each layer has a thickness $\Delta z_{unjammed}$). To verify this relationship, we analyzed the central column (center of the developing cone) of the PIV velocity field for a loose-packed stutter jump upon re-intrusion (Fig. 57). At each frame of PIV data, we fit an exponential curve according to $\dot{z}_{grain} = a^{z_{grain}+b}$ where constants, a and b were determined for each frame (Fig. 57(b)). We calculated the relative speed decrease between layers based on a specific layer thickness: $a^{\Delta z_{unjammed}}$ (Fig. 57(c)), after which we calculated an average angle as $\beta = \sin^{-1}(a^{\Delta z_{unjammed}})$ (Fig. 57(d)). Choosing a layer thickness of 8 mm yielded an initial value similar to our theoretically determined β. We suspect that the need for such a large layer thickness (poppy seed grains have approximately a 1 mm diameter) is due to grain-grain friction and the irregular non-spherical shapes of the grains. The decrease in angle with intrusion depth is qualitatively consistent with our simple model, since increasingly compacted layers will yield smaller values of β.

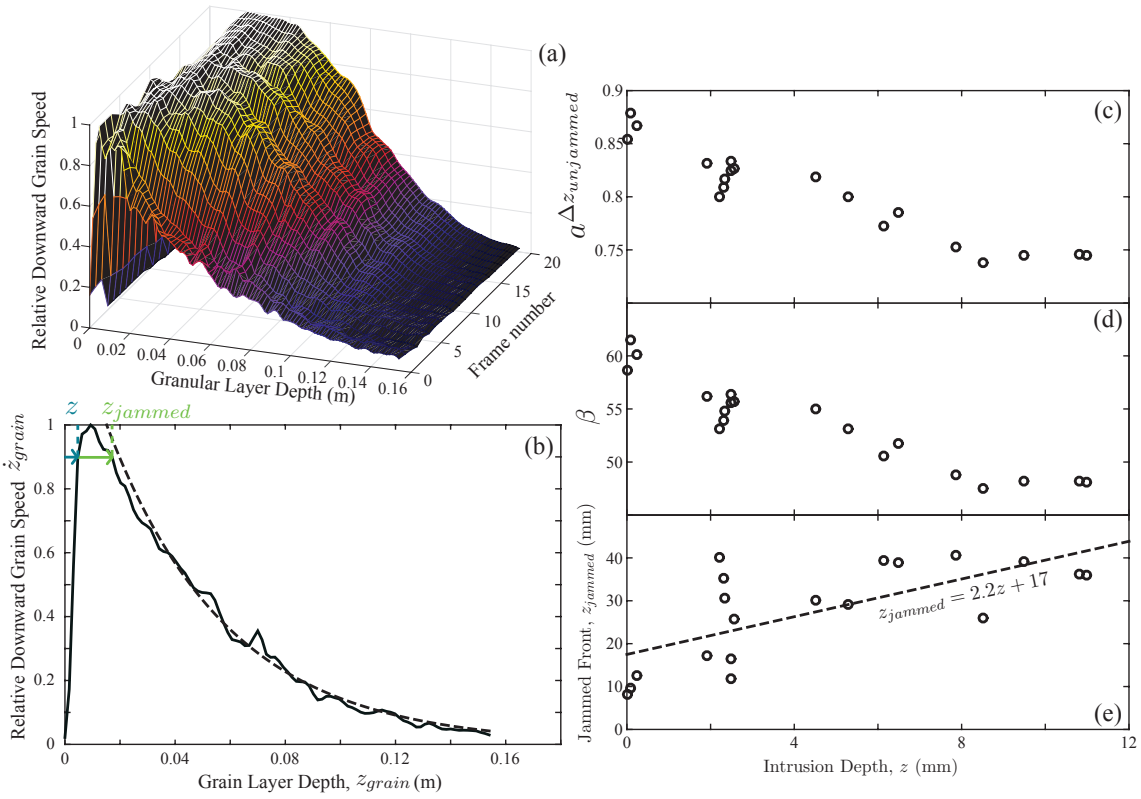

Figure 57: Analysis of central PIV grain speeds for a stutter jump at $\phi = 0.57$. (a) Vertical PIV speeds of central column relative to max speed vs. granular depth and PIV frame number. (b) Sample frame of relative grain speed vs. depth. Foot intrusion depth, z, was determined from sharp increase in PIV speed. Depth of the jammed front, z_{jammed}, was determined from grain speeds that are at least 0.9 of max speed. Exponential curve fit (dashed line) follows form, $\dot{z}_{grain} = a^{z_{grain}+b}$ where constants, a and b were determined for each frame. (c) Relative per layer decrease in speed vs intrusion depth for $\Delta z_{unjammed} = 8$ mm. (d) β vs intrusion depth for $\Delta z_{unjammed} = 8$ mm. (e) z_{jammed} vs z, linear fit (dashed) approximates $\mu = 2.2$.

We also measured the intrusion depth and depth of the jammed front, z_{jammed} by measuring the width of PIV velocities that were greater than a threshold percentage (we chose 90%) of a given frame's max speed (intrusion speed). A linear fit of the data yielded an estimated $\mu = 2.2$ (Fig. 57(e)). To compare this result with a

theoretical calculation of μ, we express the jammed layer thickness in terms of the relative displacements of the top and bottom of the layer: $\Delta z_{jammed} = \Delta z_{unjammed} + (\sin(\beta) - 1)\Delta z_{top}$. Substituting in $\frac{\Delta z_{jammed}}{\mu} = \Delta z_{top} = \Delta z$ as well as the relation in Equation 29, we arrive at a relationship for μ:

$$\mu = \frac{1 - \sin\beta}{\frac{\phi_c}{\phi} - 1}. \tag{30}$$

Using our theoretical $\beta = 57.41$ yields a μ of 2.56. Using this value for μ in calculating theoretical $F_p(z)$ curves for different size intruders yields good agreement with experiment (Fig. 58). As the radius of the intruder increases, both experiment and theory verify that the quasistatic force $F_p(z)$ saturates to its final slope at deeper penetration depths, causing the initial nonlinearity to have a larger influence on granular dynamics. Thus, for large flat surfaces, RFT cannot be considered a superposition of individual surface elements; these elements cooporate to generate a jammed front that alters the effective geometry of the intruder until a cone is fully formed.

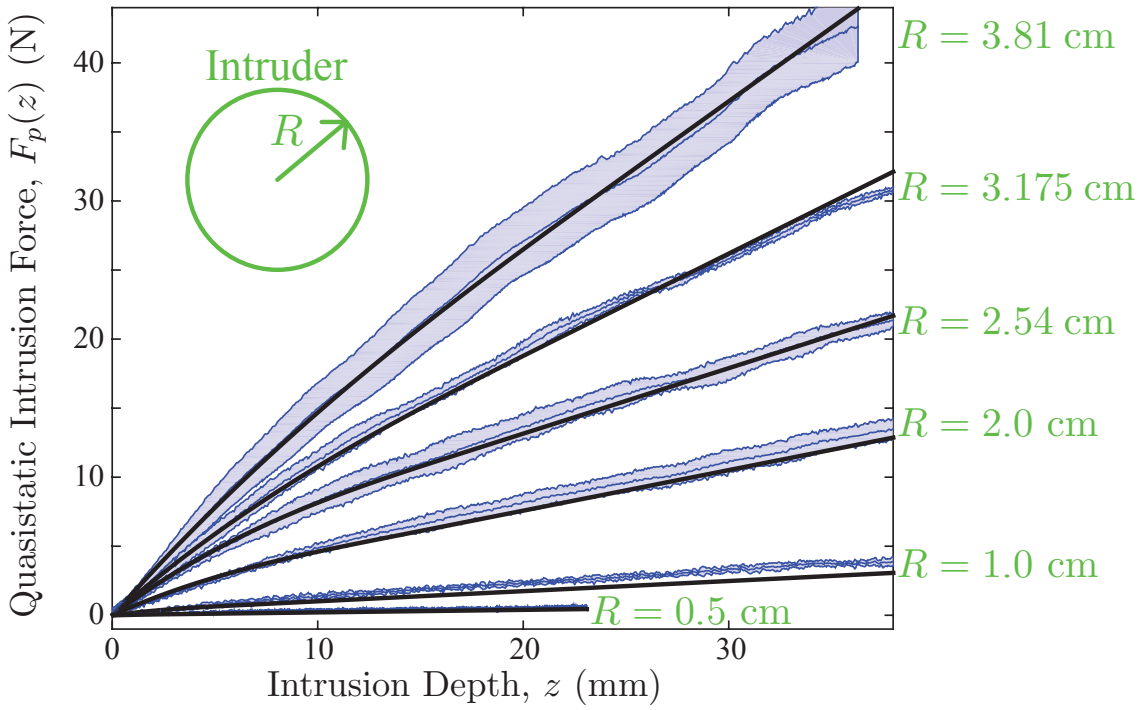

Figure 58: Quasistatic forces for different size intruders. Experimental curves (blue) are average over multiple trials; curve corresponds to forces for a flat disk intruder of specific radius, R (labeled in green). Shaded regions are standard deviations. Theoretical curves (black) were calculated with Equation 26 with a theoretical $\mu = 2.56$.

3.4 Emergence of added mass and inertial drag from a growing granular cone

While the characteristics of $F_p(z)$ are insufficient to explain the transient dynamics that decrease the stutter jump height, such insights into the development of the extended intruder volume suggest that the additional mass of the granular cone, or added mass, m_a, must be considered in the momentum of the foot. Added mass can contribute to a shear-thickening response in dense suspensions[211]. In the realm of actively forced impacts, added mass effects contribute to the impulse developed during the slap phase of a basilisk lizard running on water[80].

Added mass for an intruder impacting a fluid has been approximated by the hemispherical volume of liquid accelerated forward in front of the intruder, consistent with the velocity change imparted by an inelastic collision with a mass equal to the added mass[177, 210]. Similarly, by dividing the granular momentum, P_{grains}, by the velocity of the foot, we considered added mass in the granular media to be comprised of the grains moving with flow kinematics most similar to the downward motion of the foot. Previous studies have utilized PIV to estimate the momentum of added mass in fluids [181] and qualitatively characterize momentum transfer in dense suspensions[211]. We estimated P_{grains} by spatially integrating the PIV velocity field according to $P_{grains} \approx \rho\phi \int_0^H \int_0^{2\pi} \int_0^R v(r,h) r \, dr \, d\psi \, dh$ where h and r are the 2D velocity field coordinates, and $\rho \approx 1000$ kg/m^3 is the density of poppy seeds. ψ was approximated by assuming azimuthal symmetry of the flow field. The foot imparted a significant amount of momentum onto the grains proportional to the foot speed, most notably during the stutter jump (Fig. 52(a) right inset, maroon). The added mass, comprised primarily by the granular cone, reached values over four times the foot mass (Fig. 59(a)).

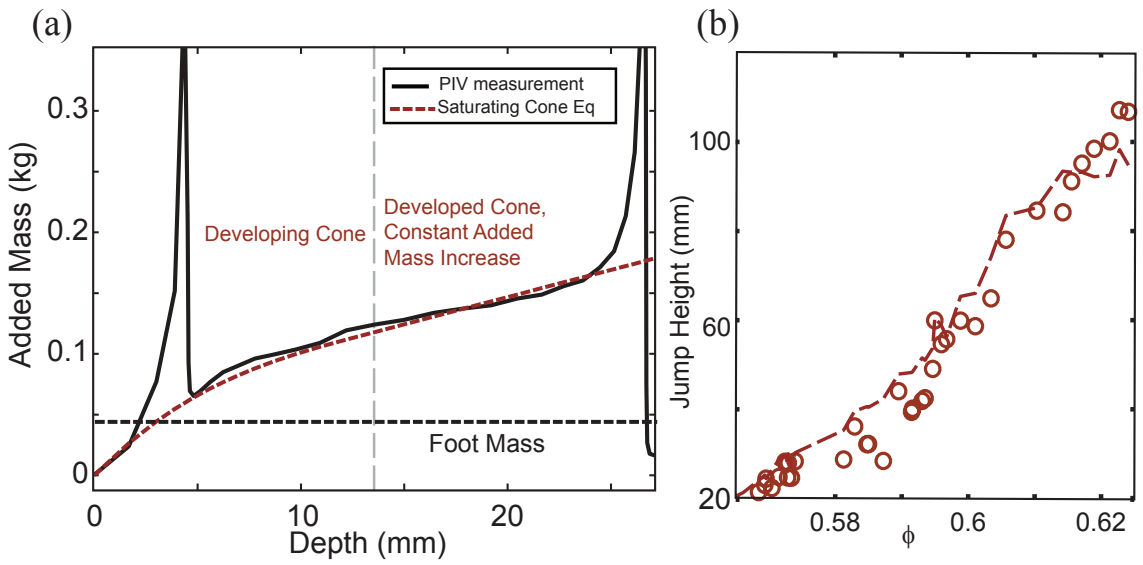

Figure 59: Inertial properties of a jamming granular cone. (a) Added mass vs. depth calculation from PIV (black, solid) and a saturating cone equation (Equation 33) for a stutter jump at $\phi = 0.57$. Added mass was calculate by dividing granular momentum by the speed of the foot. As a result, singularities in the added mass measurement appeared when the foot speed approached zero. (b) A simulation (dashed line) of stutter jump heights vs. ϕ using Equation 34 for F_{GM} improves agreement with experiment (circles) at low ϕ.

To compare with experiment, we simulated all three jump types (single, stutter and delayed stutter) with our 2D DEM scheme by prescribing the intruder trajectory as the trajectories of the foot tracked during the PIV experiments. For momentum and added mass calculations, bidisperse particles were used to avoid crystallization. Using a 2D grid of interpolated grain velocities, we were able to calculate momentum (Fig. 53(b)) and added mass (Fig. 53(c)) identically to PIV measurements. Simulation values for momentum and added mass were about twice those of PIV. While properties such as grain size, density and foot size were chosen to resemble experimental values, there were numerous differences between the DEM simulation and

PIV experiments that are likely contributing to the numerical discrepancies, from the difference in shape to the lack of gravity, boundaries or shearing grain-grain friction in simulation to the fact that the simulation only considered 2D dynamics. However, regardless of these differences, even this simple 2D simulation was able to capture many of the qualitative observations in experiment, from the relative scaling of grain momentum between different jump types to the saturating added mass.

Recently, Katsuragi et al. posited that added mass forces could play a role in the dynamics of non-forced impact into dry granular media [115] but no experimental tests were conducted. To test the role of added mass during jumping, we incorporated these dynamics into the 1D jumping simulation by modifying F_{GM}. The term in Equation 15 defining inertial drag during granular impact, αv^2, originates from the momentum change associated with colliding inelastically with a virtual mass [164], which accumulates when the impactor accelerates surrounding material, $\frac{d(m_a v)}{dt} = \frac{dm_a}{dt} v + m_a a$. However, this derivation was mainly used to analyze non-forced impacts in which there would be no forward acceleration upon impact. Furthermore, depending on the shape of the intruder, such as spheres or bullets, the added mass itself may have been minimal relative to the mass of the intruder, thus allowing for exclusion of the added mass term, $m_a a$. To consider these dynamics in our experiment, our granular reaction force becomes

$$F_{GM} = F_p(z) - \frac{dm_a}{dt} v - m_a a, \tag{31}$$

where a is the foot's acceleration. We then formulated a description of added mass accumulation based on our geometric cone model (Fig. 54(b)), where a differential increase in intrusion depth corresponded to a differential increase in added mass according to the following relation,

$$\Delta m_a = C \phi \rho A_{flat} \mu \Delta z, \tag{32}$$

where ϕ and ρ are the volume fraction and grain density, respectively, and $\mu\Delta z$ is the differential depth of the jamming front. The constant, C, scales the growth of added mass due to extra added mass from slower moving grains surrounding the cone. Taking the infinitesimal change in z, we integrated Equation 32 and found the added mass to be

$$m_a(z) = C\phi\rho\mu z\pi\left(R^2 + \frac{1}{3}\frac{(\mu z)^2}{\tan^2\theta} - \frac{R\mu z}{\tan\theta}\right). \tag{33}$$

We used this equation until $\mu z = R\tan\theta$. Both μ and C were tuned to match PIV added mass measurements (Fig. 59(a)) for all depths except when the foot speed approached zero, which caused a singularity in the added mass measurement. However, since this rapid increase in added mass only occurred during slow velocities, its effect on jumping dynamics was negligible; this was confirmed by simulations incorporating the singularity. The values of μ found were similar to those found in Section 3.3.2, which suggests that both quasistatic and inertial forces are coupled by the dynamics of the evolving cone. While estimating added mass in fluids can be challenging for all but simple intruder shapes[177], we expect that the geometry and dynamics of granular jamming fronts in other intrusion scenarios will be determined by predictable shearing behavior that forms granular cones.

Similar to sphere impact in fluids [177], an added mass model which is dependent on depth instead of time allows us to express the conservation of momentum force, $\frac{dm_a}{dt}v$, as $\frac{dm_a}{dz}v^2$, resulting in a depth dependent inertial drag term, $\alpha(z)v^2$, where $\alpha(z) = b\frac{dm_a}{dz}$. Inertial drag was also observed to be sensitive to depth in granular sphere [203] and disk impact [55]. Our granular force model becomes

$$F_{GM} = F_p(z) + \alpha(z)v^2 - m_a(z)a, \tag{34}$$

where $F_p(z)$ is still defined by an empirical two-resistance relation with reintrusion dynamics. The constant, b, is a scaling coefficient required to obtain agreement

between simulation and experiment. We set b at each ϕ such that there was agreement between experiment and simulation for all jumps. We posit that this scaling (where $b > 1$ for all ϕ) is the result of the system experiencing more inelastic granular collisions than is evident from the increasing added mass, with the cone constantly gaining and shedding grains at the shearing boundaries. Nevertheless, our added mass equation dictates that $\alpha(z)$, which is proportional to the slope of $m_a(z)$, is greatest near the surface. Introducing this reactive force into the jumping model with a correctly scaled b preserved the accuracy of the single and delayed stutter jumps and appropriately decreased the stutter jump heights at low ϕ (Fig. 59(b)). While added mass effects were negligible at high ϕ, jump heights were sensitive to the scaling, b, of inertial drag, especially during high frequency motor forcing. Interestingly, b tended to increase with ϕ in a similar qualitative trend to k_1. We expect such inertial effects will also help explain other high-speed movements such as running [170].

3.4.1 Coupling of robotic spring-mass and added mass dynamics

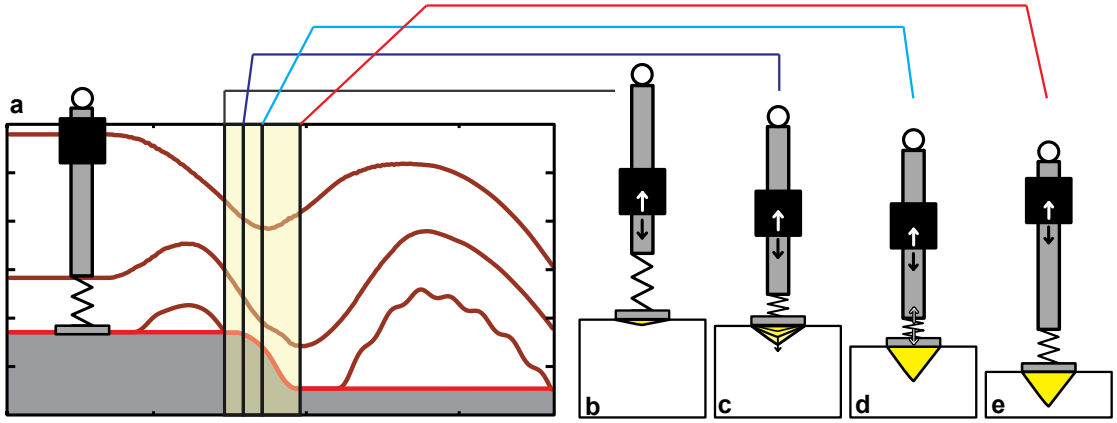

Figure 60: Simulation of coupled added mass and robot jumping dynamics. (a), Time trajectories of the motor, rod and foot positions using 1-D simulations at $\phi = 0.57$. (b-e), Snapshots of robot during landing and push-off illustrate the interplay of granular forces on stutter jump dynamics, from (b) initial foot landing, to (c) rapid added mass recruitment, to (d) spring decompression (white arrows) and a fully developed cone, to (e) granular jamming. Relative positions of robot elements were taken from 1-D simulation. Arrows on rod and motor indicate the rod being pushed down relative to the motor. Yellow added mass regions are illustrated based on the experimental PIV observations; such observations inspired the model of added mass included in the 1-D simulation. Robot scaled by $\sim 1/4$x for illustrative purposes.

We now discuss the mechanism by which the above granular physics affected the locomotor's internal state to reduce jumping performance. Added mass lowers stutter jump heights by altering the phasing of the robot's spring-mass vibration (Fig. 60), in which grain momentum causes the peak spring forces to occur at a non-ideal phase of the motor's oscillation. After the preliminary hop, the foot lands and stops due to granular reaction forces (Fig. 60(b)). The robot's actuator continues falling while it pushes the rod down, causing spring compression as the foot encounters

high inertial drag due to a rapidly developing cone of added mass (Fig. 60(c)). The spring reaches peak compression (Fig. 60(d)), slowing the thrust rod, and pushing the foot down further, assisted inertially by a fully formed added mass cone. The foot descends further due to slower decelerations from added mass (Fig. 60(e)), and a less compressed spring now produces smaller upward propulsion forces as the robot's center of mass takes off. A direct comparison of simulations using the various models of F_{GM} reveals how the reduction in spring compression during the upward swing phase of the motor only occurs when added mass forces are considered (Fig. 61).

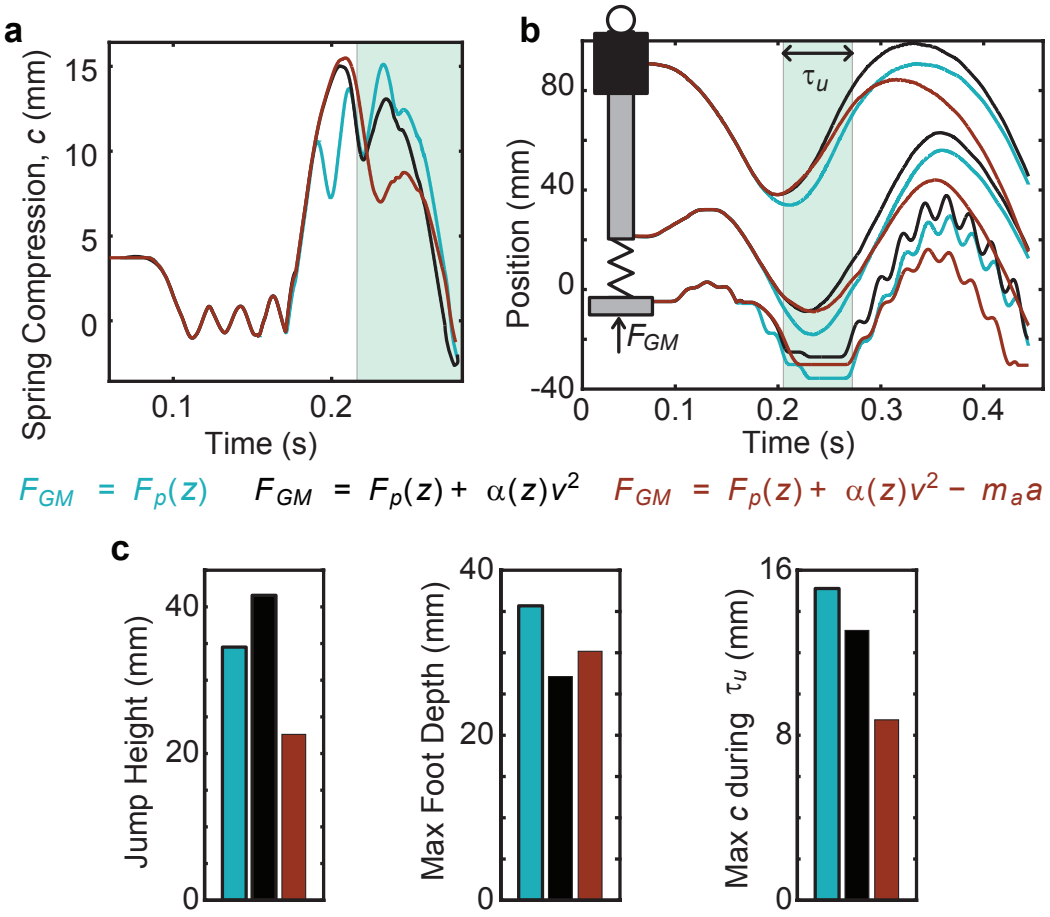

Figure 61: Comparison of stutter jump simulation using various force models for F_{GM}. (a) Jumping performance is largely determined by the spring forces during the upward swing phase of the motor, τ_u, (light blue highlight). Adding αv^2 to the static force model (black) slightly improves jump heights over the static model (teal) by reducing foot sinking. Introducing added mass (maroon) phase shifts spring mass vibration, reducing spring compression during τ_u, which reduces jump heights. (b) Simulated trajectories of the motor, rod and foot compare stutter jump kinematics using different granular force models. Relevant quantities are summarized in (c).

Prescribing a delay improves the jump height in two ways. A sufficiently long delay time separates both methods of granular intrusion: passive intrusion from the robot's falling inertia during landing and active intrusion during push-off. Separating

these two mechanisms reduces the overall intrusion speeds of the foot, reducing the compounding effect of the added mass decreasing the deceleration rate. As such, the robot sinks less and is able to provide more upward spring forces to the robot. Selecting the optimal delay time ensures that the phasing transfers maximal spring energy during the upward take-off movement of the motor.

3.5 Terrain-aware Motion Planning for Jumping on Granular Media

3.5.1 Summary

In pursuit of dynamic walking and running robots, significant progress has been made toward motion planning with the nonlinear, hybrid dynamics of legged machines [137, 214]. However, while dirt, sand, mud, and other deformable terrain are ubiquitous in nature, by and large, underlying physical models employed in motion planning typically assume rigid contact. Given the insights into granular interactions previously discussed in this Chapter, we now discuss a tractable method for motion planning subject to rapid interactions in loose-packed granular media (e.g. sand, a ubiquitous medium which has proven useful in the study of complex locomotion [129, 135]), and experimentally validate planning trajectories on the granular jumping test bed used in our previous experiments of jumping on granular media [2]. This work was performed in conjunction with Dr. Christian Hubicki of Prof. Aaron Ames' group and is found in [103].

3.5.2 Motion Planning and System Modeling

Optimal motion planning techniques can quickly and precisely design controlled robotic trajectories to near-arbitrary specifications. Our study utilizes the direct collocation approach [209] for motion planning, which has been used previously by Hubicki to optimize jumping plans over the course of 20 steps [102], and has been

streamlined further to optimize 3D walking for a humanoid robot [95]. Direct collocation methods simultaneously perform the integration of the robot's dynamical model (which includes interactions with the environment) and solve for optimized control trajectories that produce desired output kinematics. The optimizer integrates the dynamics by solving a series of algebraic equality constraints at a series collocation points. Such methods are optimal when dynamical equations can be written in closed-form [112, 95]. Furthermore, the success and predictive ability of the optimizer is dependent upon the accuracy of the supplied model. For the experiments of this study, we used the granular jumping testbed from our other granular jumping experiments described in this Dissertation. Thus, the dynamical equation for the robot model used by the optimizer was the same model used in previous simulations.

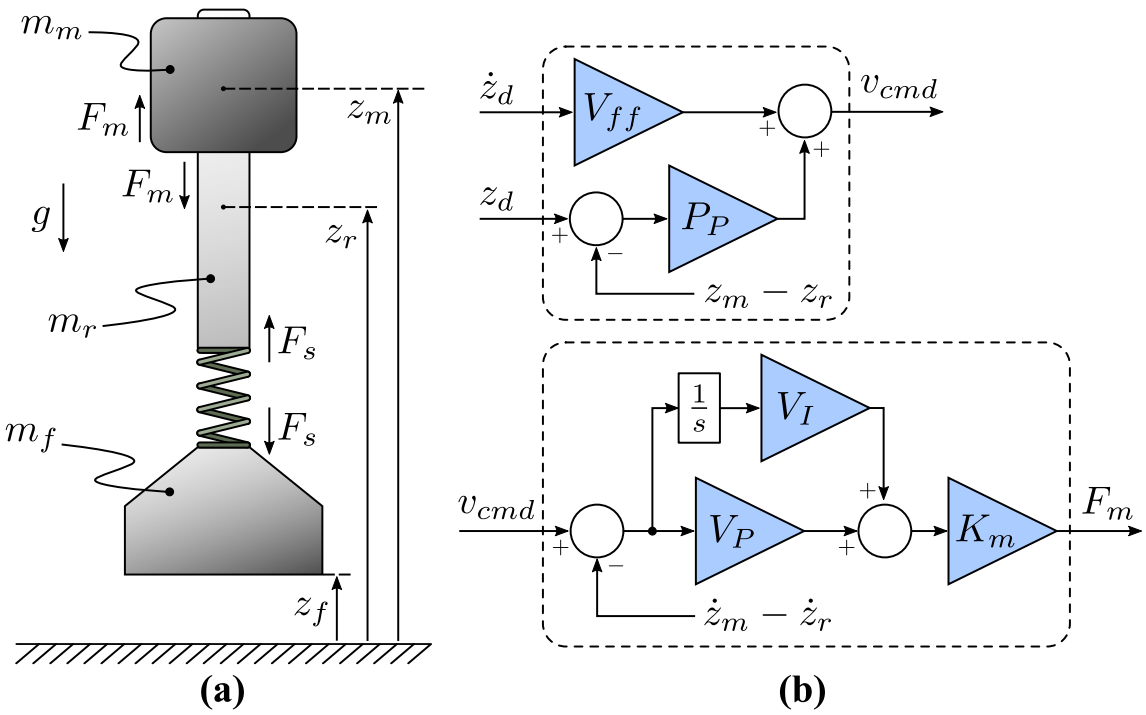

Figure 62: **(a)** A diagram of the jumping robot math model with feedback dynamics. **(b)** The motor control feedback loop used to track the open-loop desired actuator position trajectory, z_d, such that $z_m - z_r \rightarrow z_d$. This feedback loop is modeled explicitly in the optimization as a passive-dynamic element, so the open-loop command trajectory z_d can be designed with awareness of tracking dynamics.

However, unlike previous simulations, we additionally considered the feedback dynamics of the robot's actuator. In the sand jumping experiments of [2], the feedback dynamics could be ignored, because the direct encoder position trajectory of experimental jumps were fed into the command motor position of the simulation, thus already accounting for trajectory deviations due to feedback tracking error. Since the optimizer determines a command trajectory to perform specific objectives, simulation of the feedback dynamics was essential. The motor-position feedback control loop (Fig. 62(b)) impacted the robot's dynamics, even when well-tuned control gains resulted in small deviations in the relative motor trajectory (Fig. 63).

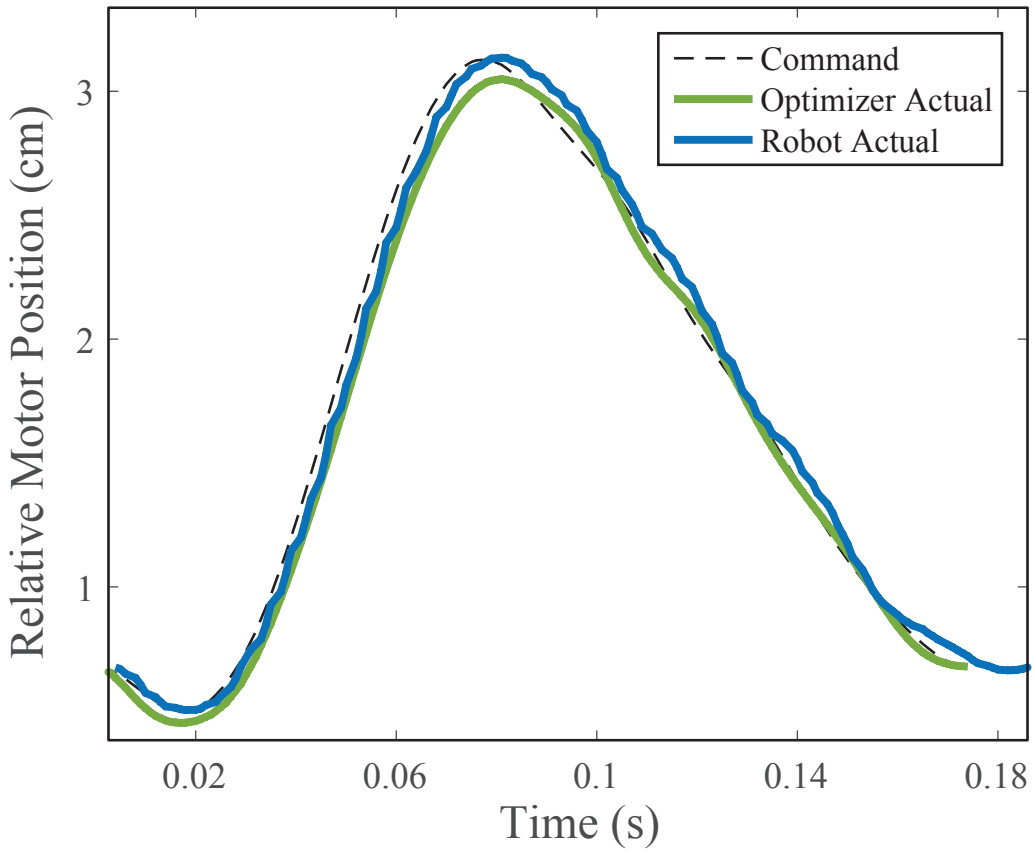

Figure 63: Motor command trajectory tracking as predicted by the optimization and measured on the robot. The gap between the measured motor trajectory and the command is small, but has a significant impact on the resulting jumping dynamics. This motivated our inclusion of the feedback-loop dynamics (Fig. 62(b)), in the overall math model.

The insights into impulsive granular dynamics discussed in the previous Sections of this Chapter allowed for the formulation of a closed form dynamical equation describing the granular forces on the foot. We employed the granular cone-based added mass model derived from the above experiments in jumping on sand [2]. Unlike the model used for previous simulations [2], we defined the quasistatic force, $F_p(z)$, by the cone-based Equation 26 rather than the two-resistance relation. As such, all

granular forces were determined by the evolution of the granular cone. To simplify our protocol, we only considered single take-off trajectories (i.e. no stutter jumps), so as to not consider reintrusion dynamics. This principled reduced-order formulation could also be represented with closed-form equations, making it amenable to fast motion planning techniques. The dynamical equations, constraints and the direct collocation formulation specific to our experiments are described in detail in [103].

3.5.3 Experiment and Results

As an aggressive benchmark for the accuracy of our motion plans, we tested open-loop impulsive jumping on loose-packed grains. Open-loop impulsive jumping presents a number of challenges. By sending only open-loop motor-position commands to the jumper, there is no opportunity to correct errors online. We measured jump height accuracy by apex height error, which is sensitive to the error in takeoff velocity. The ballistic dynamics of the airborne model dictate that errors in hop height scale with the square of the takeoff error. By demanding high jumps which require quick impulsive motions, we insured that the robot induced complex inertial reaction forces from the granular media.

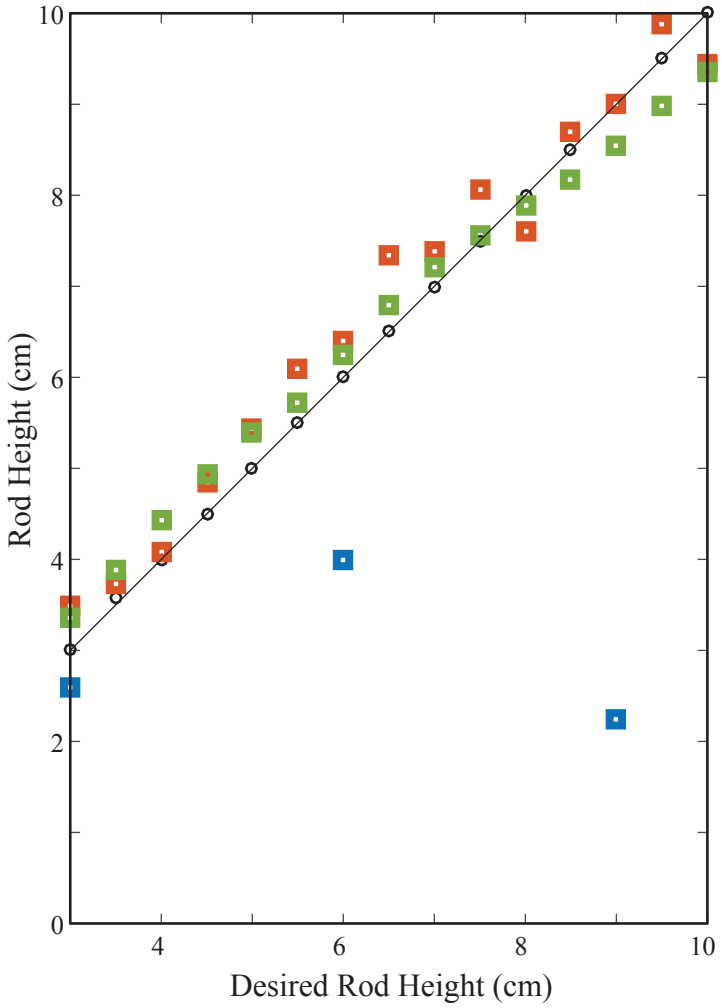

Figure 64: A plot of actual jumping apex heights vs. commanded apex heights for all three experimental groups. Granular media (GM) command trajectories jumped nearly as accurately on granular media (3.9 ± 2.1 mm) (red squares) as rigid strategies jumped on hard ground (HG) (3.4 ± 1.5 mm) (green squares). In contrast, rigid ground strategies not only underperformed on granular media (blue squares), but the trajectory optimized for the highest jump performed the most poorly of all tested scenarios. Black circles indicate optimizer jumping predictions.

In total, this work [103] comprised of three experimental groups of impulsive robotic jumping (Fig. 64). We tested **1)** a trajectory optimized with a rigid ground model, executed on rigid ground, **2)** a trajectory optimized with the added-mass

model and executed on loosely packed poppy seeds, and **3)** a trajectory optimized with a rigid ground model, but executed on loosely packed poppy seeds. Optimizing with the added mass model allowed the jumper to accurately hit its target apex height within 6.6% error. Further, not only did rigid-ground strategies come nowhere close to target heights (40.6% error), some higher-jumping strategies performed significantly worse on granular media than lower-jumping strategies.

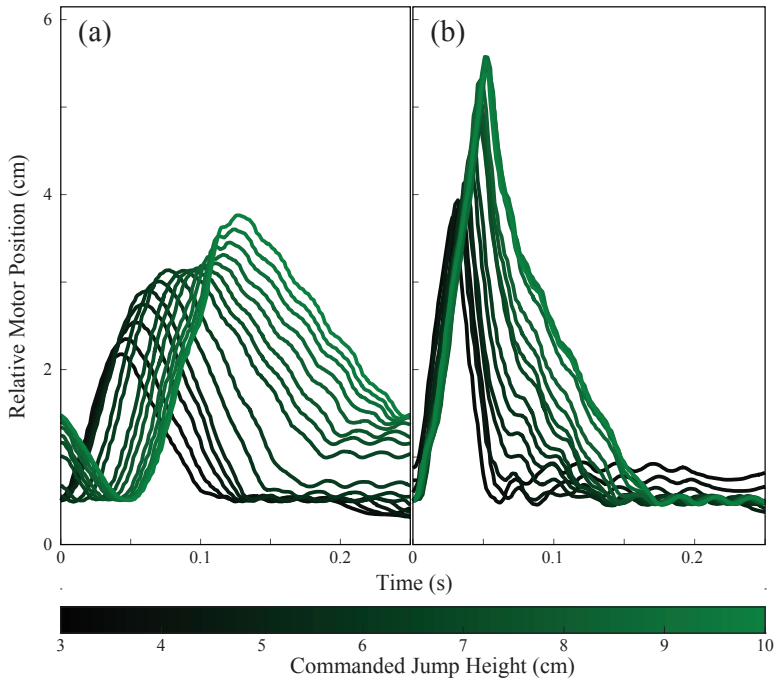

Figure 65: Side-by-side plots of the executed motor trajectories ($z_m - z_r$) optimized for **(a)** rigid ground and **(b)** loosely-packed granular media. Across terrain types, the amplitude and shape of the motor trajectories are clearly distinct. Within terrain types, we observe a smooth shift in strategy with increasing jump height.

A comparison of the motion plans optimized for hard ground and granular media revealed that the optimizer produced qualitatively different strategies between the two surfaces (Fig. 65). Unsurprisingly, granular media strategies required more thrust, nearly twice the amplitude compared to the counterpart rigid strategies. However, the shape of the motor trajectories was also markedly different. Rigid strategies took

advantage of "pull-then-push" strategy, while granular media trajectories favored a single, quick thrust. Thus, successful control on granular media isn't just a matter of amplifying rigid-ground strategies, but thoughtfully considering the complex dynamics of the terrain. Overall, these results serve as a proof of concept that optimal motion planning, a powerful tool in legged locomotion control, can be made accurate and tractable through highly complex substrates.

CHAPTER IV

CONCLUSION

4.1 Accomplishments

We have demonstrated that a simple spring-mass hopper on both hard ground and granular media exhibits rich dynamics. We performed a systematic and automated study of experimental hard ground jumping, where we commanded sinusoidal wave actuation strategies and varied the parameters of actuation, such as amplitude, forcing frequency and initial phase. This variation of parameters revealed two main types of jumps, the stutter jump and single jump. The stutter was induced by a countermovement where the motor starts near the top of the thrust rod and pulls the rod up for a preliminary hop, followed by a push-off during landing. The single jump consisted only of a push-off phase. The optimal forcing frequencies for both jumps were found to be off-resonant: given the parameters of the mass, stiffness, gravity and forcing amplitude used (which can be non-dimensionalized to a single parameter, mg/kA), the stutter jump was optimal below the natural frequency, and the single jump was optimal above the natural frequency. The lower optimal frequency of the stutter jump caused the required peak motor power to be lower than that needed for the single jump.

A simulation analysis that varied mg/kA revealed how relative jump height, motor power and optimal frequency varied with mg/kA for both jump types. Within a range of values for mg/kA (about 0.1 to 0.9), the stutter jump was doubly ideal due to its jump height being higher and peak power requirement being lower. An analysis of the stutter jump's kinematics yielded estimates of the stutter jump's optimal frequency vs mg/kA, which provided insight into the influence of the relative time scales of the

aerial phase and the grounded phase.

We additionally discussed how our model compared to animal jump heights at different size scales. Based on simplistic assumptions about the scaling of mg/kA with body size, reported values of animal jump heights were always much lower than simulated single jumps and typically higher than simulated stutter jumps. We attributed this to the fact that the relative power requirements and optimal frequencies of single jumps are exceedingly high for single jumps and increase with decreasing values of mg/kA.

We also constructed a fully automated bed of granular media that could perform and collect data on jumping experiments using the spring mass hopper, fluidize the bed, reset the granular state and control the volume fraction between experiments. These experiments revealed that unmodified stutter jumps performed more poorly than single jumps in loose packed granular media (whereby, given the parameters of the robot, the stutter would perform better than the single jump on hard ground). Incorporating a delay time between the pull-up phase and push-off phase of the stutter improved jumps relative to the single jumps. Further experiments attributed the need for this delay time to an added mass effect in granular media (which had not been considered before in dry granular media) due to a jammed cone of grains that developed beneath the foot and moved with the foot. The added mass produced an inertial phase shift in the stutter jump where the foot sank deeper and was not able to maximally compress the spring during the upward swing of the robot's center of mass. This cone effectively extended the geometry of the foot beneath the granular surface, and an analysis of the growth of the jamming front revealed that this cone also affected quasistatic forces and coupled the dynamics of all the quastistatic and hydrodynamic-like granular forces. Development of this principled model allowed for a motion planning optimizer to produce accurately predicted optimal open loop controlled jumps on granular media.

4.2 Future Investigations

4.2.1 Optimizing for diverse performance goals

A significant utility of optimal motion planning (such as the direct collocation formulation supplied by Dr. Christian Hubicki in Section 3.5 [103]) is the ability to plan for more diverse performance goals with creative constraints. A future goal will be to leverage such a tool to exploit the locomotor's physics and environmental interactions and achieve objectives beyond typical goals such as take-off speeds or jump heights, such as obstacle avoidance or turning maneuvers (perhaps not in our 1D hopper). To this end, the optimizer has already succeeded in producing an open-loop trajectory the enables the robot to jump to a specific height within a specified time and then effectively "stick" the landing (a gymnastics inspired maneuver, Fig. 66) on hard ground. Previous experiments have shown how such a maneuver is possible by simply reducing feedback gains to dampen the robot, however, the optimizer achieved identical dynamics with open loop trajectory control. One can imagine how such controlled landings can be crucial in sensitive missions such as that of a comet lander.

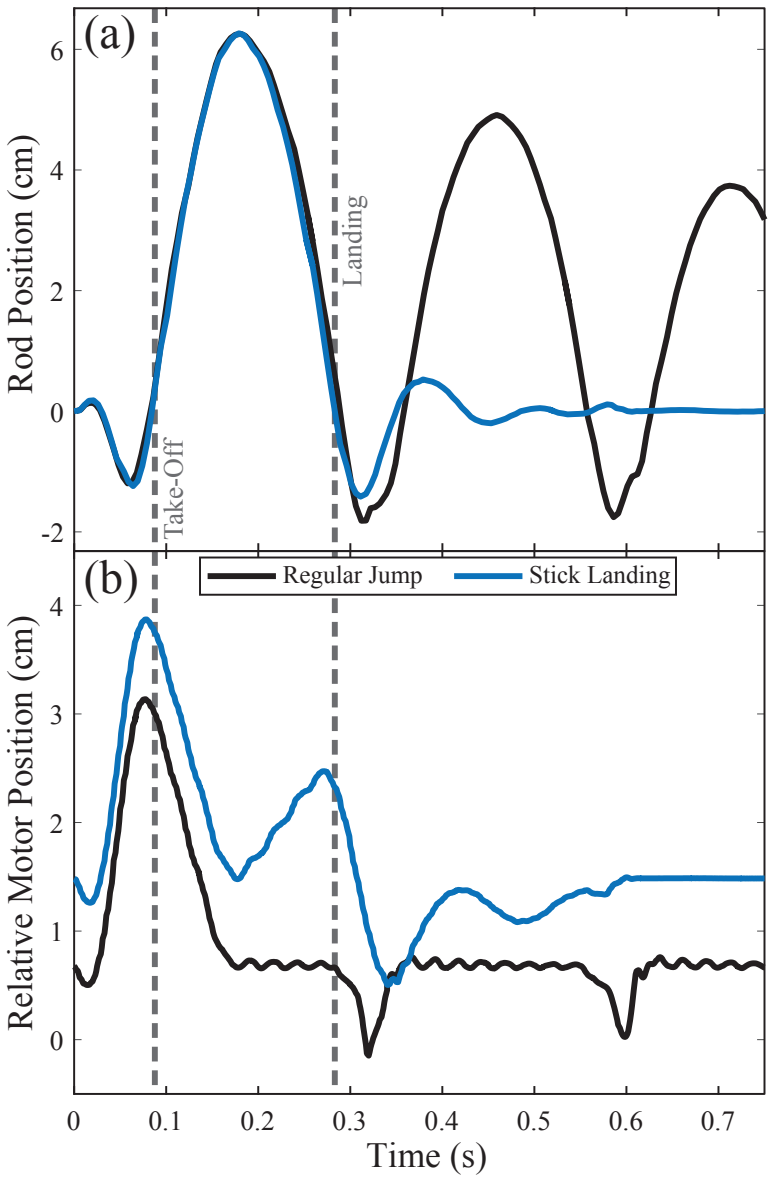

Figure 66: Experimental trajectory comparison of regular single jump vs. jump with stick landing. (a) Rod positions vs time. (b) Relative motor actuation trajectories vs time.

4.2.2 Motion planning optimization as a robophysical tool to uncover and leverage new granular physics

While tuning the feedback gains of the optimizer's model to match the experimental robot's hard ground kinematics, the gains were at one point set to values that inadvertently produced an output trajectory that can be best described as a 'stop-go' motion. The trajectory was not a single downward stroke, but rather consisted of an intermediate pausing phase in the forcing (Fig. 67). When implemented and performed by the robot, the optimizer under-predicted the actual jump height by about 30 mm, where the expected jump height was 60 mm, and the experimental jump height was 90 mm (Fig. 67(a)).

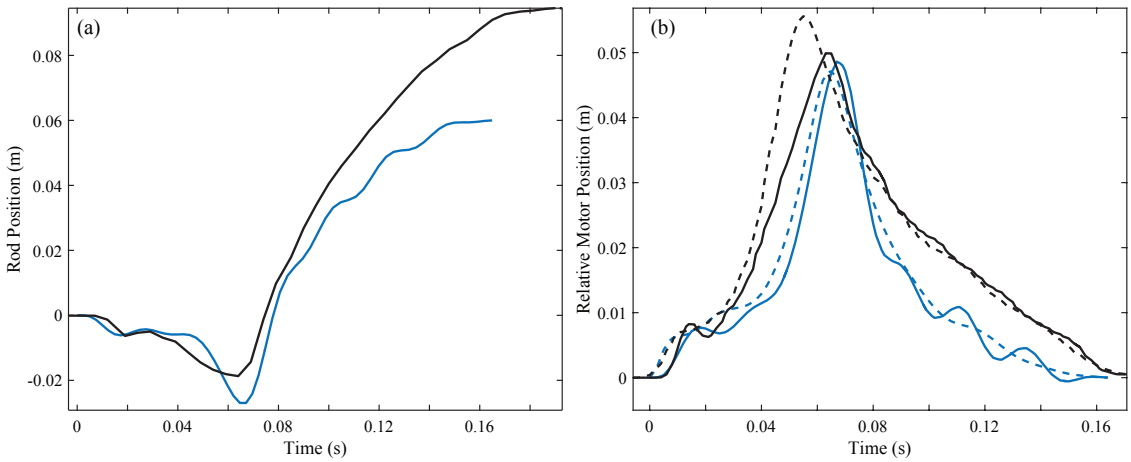

Figure 67: Experimental vs optimizer prediction of 'stop-go' jumping trajectory. (a) Rod position vs. time for experiment (black) vs prediction (blue). Optimizer's command max height was 60 mm. (b) Relative motor forcing trajectory vs. time comparison of both commanded (dashed) vs. actual (solid) for both experiment (black) and prediction (blue).

While there was some variance in the actual command trajectory between experiment and optimizer (Fig. 67(b)), the variance during the motor's downward intrusion

stroke was minimal, and similar differences in trajectory were observed in well predicted jumps. However, the primary granular modeling component excluded from the optimization routine was the empirical reintrusion model observed in [2] (Fig. 50). While no reintrusions occurred before take-off in the optimizer, the optimizer did yield foot kinematics whereby, midway into the intrusion, the foot reached a velocity of nearly zero before intruding further (Fig. 68). We hypothesized that this behavior could be inducing reintrusion-type forces.

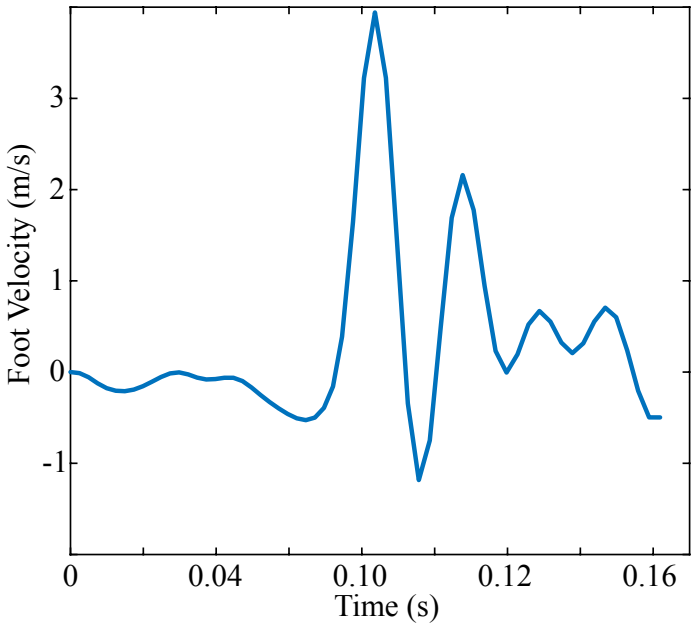

Figure 68: Optimizer prediction of foot speed during stop-go maneuver. Foot intrudes, slows to nearly zero speed, then continues intruding before lift-off.

To test this hypothesis, we have begun to perform systematic stop-go intrusion measurements on a Denso robot arm fitted with a force sensor. The primary motion protocol was to slowly intrude (10 mm/s) a flat intruder with about 4 cm sides to a specific intrusion depth, pause for a specific time, and then continue intrusion. Preliminary results indicate similar overshoots to those in reintrusions which are proportional to the depth at which the stop-go motion was performed (Fig. 69(a)).

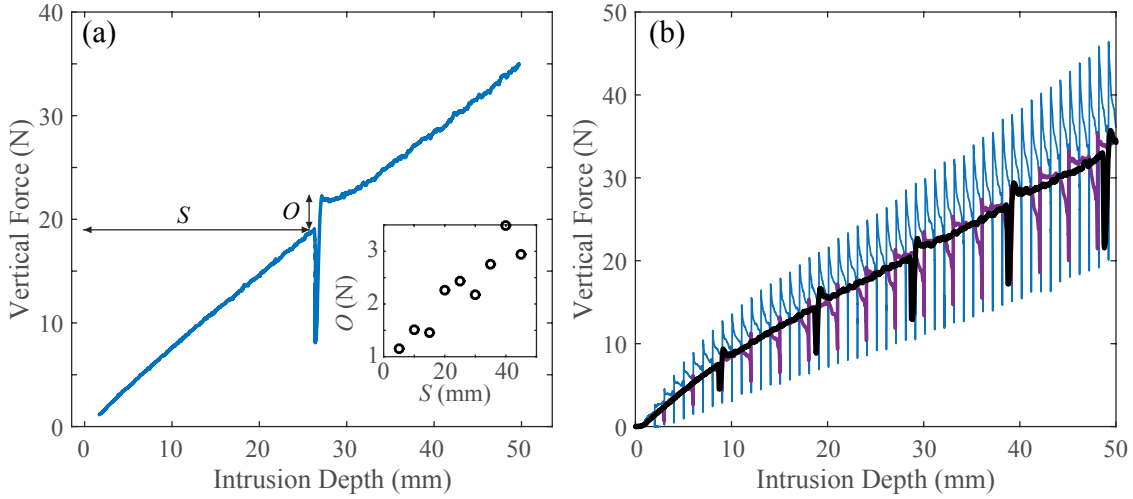

Figure 69: Force vs. depth measurements of stop-go intrusions. (a) Sample stop-go measurement in loose-packed poppy seeds for a pause time of 3 seconds. The force overshoot, O, was found to be proportional to the intrusion depth of the stop-go motion, S (inset). (b) Force vs. depth for for compounded stop-go motions with 0.2 second pause time for step lengths of 10 mm (black), 3 mm (purple) and 1 mm (blue).

We additionally performed multiple stop-go movements within one intrusion, whereby the robot arm intruded by some step length and paused in between steps for some pause time. We sought to examine the effect of pausing an intrusion while it was still exhibiting a force overshoot. Consequently, the smallest step length tested (1 mm) yielded higher overshoot forces (Fig. 69(b)) than the longer step lengths (3 mm and 10 mm), suggesting a potential compounding force. We suspect that the dynamics of both stop-go forces and reintrusion forces are coupled to mechanics of local compaction. A laser speckle analysis beneath the intruder during these events (similar to those performed during drag experiments [83]) may provide insight into the local compaction properties.

Developing a principled description of these intrusion mechanics will potentially allow an optimized motion planning routine to intentionally exploit such mechanics

in concert with cone-based static and inertial forces and produce more optimal jumps.

4.2.3 Expanded understanding of jamming granular structures

While estimating added mass in fluids can be challenging for all but simple intruder shapes [177], we expect that the geometry and dynamics of granular jamming fronts in other intrusion scenarios will be determined by shearing behavior that forms predictably shaped jamming fronts. A systematic investigation of how these jamming fronts form will allow for a more complete model of granular reaction forces to both predict locomotion kinematics on and within granular media, as well as have an intuitive understanding of their dynamics. This is particularly important for fast modes of locomotion like jumping, hopping and running, which induce inertial forces from the substrate due to the formation of these fronts. In particular, a systematic investigation of the how nonlinearities in the frictional resistive forces change with changing foot size (and if these changes in force have a correspondence with how the granular cones are forming) will provide insight into how the scaling of feet affects the importance of force nonlinearities at the onset of intrusion into the substrate or in general the relative contributions of the different types of forces. For, example, for a flat circular disc foot, the quasistatic and inertial drag forces will scale proportionally with R^2 (where R is the foot's radius), whereas the added mass will scale with R^3. More broadly, understanding the shape and evolution of jamming granular fronts from other orientations (aside from just vertical intrusions), movement trajectories (such as rotations in the media), and foot properties (foot shape and surface friction, mass), will facilitate the understanding of more complex movements in granular media.

REFERENCES

[1] Aerts, P., "Vertical jumping in Galago senegalensis: the quest for an obligate mechanical power amplifier," *Transactions of the Royal Society*, vol. 353, no. 1375, pp. 1607–1620, 1998.

[2] Aguilar, J. and Goldman, D. I., "Robophysical study of jumping dynamics on granular media," *Nature Physics*, vol. 12, pp. 278–283, Mar 2016. Article.

[3] Aguilar, J., Lesov, A., Wiesenfeld, K., and Goldman, D. I., "Lift-off dynamics in a simple jumping robot," *Physical review letters*, vol. 109, no. 17, p. 174301, 2012.

[4] Aguilar, J., Zhang, T., Qian, F., Kingsbury, M., McInroe, B., Mazouchova, N., Li, C., Maladen, R., Gong, C., Travers, M., Hatton, R. L., Choset, H., Umbanhowar, P. B., and Goldman, D. I., "Locomotion robophysics: the study of movement at the intersection of robotics, soft matter and dynamical systems, in press," *Reports on Progress in Physics*, 2015.

[5] Ahmadi, M. and Buehler, M., "The ARL monopod II running robot: Control and energetics," in *Robotics and Automation, 1999. Proceedings. 1999 IEEE International Conference on*, vol. 3, pp. 1689–1694, 1999.

[6] Akinfiev, T., Armada, M., and Montes, H., "Vertical movement of resonance hopping robot with electric drive and simple control system," *IEEE 11th Mediterranean Conference on Control and Automation (MED03), Greece*, 2003.

[7] Albro, J. and Bobrow, J., "Optimal motion primitives for a 5 dof experimental hopper," in *Robotics and Automation, 2001. Proceedings 2001 ICRA. IEEE International Conference on*, vol. 4, pp. 3630–3635, 2001.

[8] Alexander, R. M., "Leg design and jumping technique for humans, other vertebrates and insects.," *Philosophical transactions of the Royal Society of London. Series B, Biological sciences*, vol. 347, pp. 235–48, Feb. 1995.

[9] Alexander, R. M., "Modelling approaches in biomechanics.," *Philosophical transactions of the Royal Society of London. Series B, Biological sciences*, vol. 358, pp. 1429–35, Sept. 2003.

[10] Alexander, R. M. and Vernon, A., "The mechanics of hopping by kangaroos (Macropodidae)," *Journal of Zoology*, vol. 177, pp. 265–303, Aug. 1973.

[11] Alexander, R. M., "Tendon elasticity and muscle function.," *Comparative biochemistry and physiology. Part A, Molecular & integrative physiology*, vol. 133, pp. 1001–11, Dec. 2002.

[12] Alexander, R., "Elastic mechanisms in primate locomotion," *Zeitschrift für Morphologie und Anthropologie*, 1991.

[13] Alexander, R., *Principles of animal locomotion*. Princeton University Press, 2002.

[14] Alexander, R. M., "Optimum take-off techniques for high and long jumps.," *Philosophical transactions of the Royal Society of London. Series B, Biological sciences*, vol. 329, pp. 3–10, July 1990.

[15] Allen, W. A., Mayfield, E. B., and Morrison, H. L., "Dynamics of a projectile penetrating sand," *Journal of Applied Physics*, vol. 28, no. 3, pp. 370–376, 1957.

[16] Allison, J., "Monopod Jumping Robot," 2002.

[17] Ambroso, M., Kamien, R., and Durian, D., "Dynamics of shallow impact cratering," *Physical Review E*, vol. 72, no. 4, p. 041305, 2005.

[18] Andreotti, B., Forterre, Y., and Pouliquen, O., *Granular media: between fluid and solid*. Cambridge University Press, 2013.

[19] Anitescu, M. and Potra, F. A., "Formulating dynamic multi-rigid-body contact problems with friction as solvable linear complementarity problems," *Nonlinear Dynamics*, vol. 14, no. 3, pp. 231–247, 1997.

[20] Armour, R., Paskins, K., Bowyer, A., Vincent, J., Megill, W., and Bomphrey, R., "Jumping robots: a biomimetic solution to locomotion across rough terrain.," *Bioinspiration & biomimetics*, vol. 2, pp. S65–82, Sept. 2007.

[21] Askari, H. and Kamrin, K., "Intrusion in heterogeneous materials: Simple global rules from complex micro-mechanics," *arXiv preprint arXiv:1510.02966*, 2015.

[22] Aste, T., "Volume fluctuations and geometrical constraints in granular packs," *Physical review letters*, vol. 96, no. 1, p. 018002, 2006.

[23] Astley, H. C. and Roberts, T. J., "Evidence for a vertebrate catapult: elastic energy storage in the plantaris tendon during frog jumping," *Biology letters*, vol. 8, no. 3, pp. 386–389, 2012.

[24] Azizi, E. and Roberts, T. J., "Muscle performance during frog jumping: influence of elasticity on muscle operating lengths," *Proceedings of the Royal Society of London B: Biological Sciences*, vol. 277, no. 1687, pp. 1523–1530, 2010.

[25] Babic, J., "Biarticular Legged Robot : Design and Experiments," in *2008 IEEE International Conference on Robotics and Biomimetics*, pp. 155–159, 2009.

[26] Backman, M. E. and Goldsmith, W., "The mechanics of penetration of projectiles into targets," *International Journal of Engineering Science*, vol. 16, no. 1, pp. 1–99, 1978.

[27] Baraff, D., "Issues in computing contact forces for non-penetrating rigid bodies," *Algorithmica*, vol. 10, no. 2-4, pp. 292–352, 1993.

[28] Bennet-Clark, H. C., "The energetics of the jump of the locust Schistocerca gregaria.," *The Journal of experimental biology*, vol. 63, pp. 53–83, Aug. 1975.

[29] Bennet-Clark, H. C. and Lucey, E. C., "The jump of the flea: a study of the energetics and a model of the mechanism.," *The Journal of experimental biology*, vol. 47, pp. 59–67, Aug. 1967.

[30] Bennet-Clark, H., "Energy storage in jumping animals," *Perspectives in Experimental Biology*, 1976.

[31] Bennet-Clark, H., "Scale effects in jumping animals," *Scale effects in animal locomotion*, pp. 185–201, 1977.

[32] Bennett, M., Ker, R., Imery, N., and Alexander, R., "Mechanical properties of various mammalian tendons," *Journal of Zoology*, vol. 209, no. 4, pp. 537–548, 1986.

[33] Berkemeier, M. and Desai, K., "Control of hopping height in legged robots using a neural-mechanical approach," in *Robotics and Automation, 1999. Proceedings. 1999 IEEE International Conference on*, pp. 1695–1701, 1999.

[34] Biewener, A., Alexander, R. M., and Heglund, N. C., "Elastic energy storage in the hopping of kangaroo rats (Dipodomys spectabilis)," *Journal of Zoology*, vol. 195, pp. 369–383, Aug. 1981.

[35] Biewener, A., Konieczynski, D., and Baudinette, R., "In vivo muscle force-length behavior during steady-speed hopping in tammar wallabies.," *The Journal of experimental biology*, vol. 201, pp. 1681–94, June 1998.

[36] Biewener, A. A., "Biomechanical consequences of scaling," *Journal of Experimental Biology*, vol. 208, no. 9, pp. 1665–1676, 2005.

[37] Blickhan, R., "The spring-mass model for running and hopping," *Journal of biomechanics*, vol. 22, no. 11, pp. 1217–1227, 1989.

[38] Blickhan, R. and Full, R., "Similarity in multilegged locomotion: Bouncing like a monopode," *Journal of Comparative Physiology A: Neuroethology ...*, 1993.

[39] Blickhan, R., Seyfarth, A., Geyer, H., Grimmer, S., Wagner, H., and Günther, M., "Intelligence by mechanics.," *Philosophical transactions. Series A, Mathematical, physical, and engineering sciences*, vol. 365, pp. 199–220, Jan. 2007.

[40] Bo-Ming, Y. and Jian-Hua, L., "A geometry model for tortuosity of flow path in porous media," *Chinese Physics Letters*, vol. 21, no. 8, p. 1569, 2004.

[41] Bobbert, M., "Dependence of human squat jump performance on the series elastic compliance of the triceps surae: a simulation study," *Journal of Experimental Biology*, 2001.

[42] Bobbert, M., Mackay, M., Schinkelshoek, D., Huijing, P., and van Ingen Schenau, G., "Biomechanical analysis of drop and countermovement jumps," *European journal of applied physiology and occupational physiology*, vol. 54, pp. 566–573, 1986.

[43] Bougie, J., Moon, S. J., Swift, J. B., and Swinney, H. L., "Shocks in vertically oscillated granular layers," *Physical Review E*, vol. 66, p. 051301, 2002.

[44] Brackenbury, J. and Wang, R., "Ballistics and visual targeting in flea-beetles (Alticinae)," *The Journal of Experimental Biology*, vol. 198, pp. 1931–42, Jan. 1995.

[45] Brennen, C., "A review of added mass and fluid inertial forces.," tech. rep., DTIC Document, 1982.

[46] Bridge, B., Dubowsky, S., Kesner, S., Plante, J.-S., and Boston, P., "Hopping mobility concept for search and rescue robots," *Industrial Robot: An International Journal*, vol. 35, no. 3, pp. 238–245, 2008.

[47] Brown, B. and Zeglin, G., "The bow leg hopping robot," *Robotics and Automation*, 1998.

[48] Burdick, J. and Fiorini, P., "Minimalist Jumping Robots for Celestial Exploration," *The International Journal of Robotics Research*, vol. 22, pp. 653–674, July 2003.

[49] Burdick, J. and Fiorini, P., "Minimalist jumping robots for celestial exploration," *The International Journal of Robotics Research*, vol. 22, no. 7-8, pp. 653–674, 2003.

[50] Cavagna, G., Thys, H., and Zamboni, A., "The sources of external work in level walking and running.," *The Journal of physiology*, vol. 262, no. 3, pp. 639–657, 1976.

[51] Cham, J. and Cutkosky, M., "Dynamic stability of open-loop hopping," *Journal of dynamic systems, measurement, and control*, vol. 129, no. 3, p. 275, 2007.

[52] Choi, I. and Park, K., "Variations in take-off velocity of anuran amphibians: relation to morphology, muscle contractile function and enzyme activity," *Comparative Biochemistry and Physiology Part A: Physiology*, vol. 113, no. 4, pp. 393–400, 1996.

[53] Choi, I., Shim, J. H., and Ricklefs, R. E., "Morphometric relationships of take-off speed in anuran amphibians.," *Journal of experimental zoology. Part A, Comparative experimental biology*, vol. 299, pp. 99–102, Oct. 2003.

[54] Ciamarra, M. P., Lara, A. H., Lee, A. T., Goldman, D. I., Vishik, I., and Swinney, H. L., "Dynamics of drag and force distributions for projectile impact in a granular medium," *Physical review letters*, vol. 92, no. 19, p. 194301, 2004.

[55] Clark, A. H. and Behringer, R. P., "Granular impact model as an energy-depth relation," *EPL (Europhysics Letters)*, vol. 101, no. 6, p. 64001, 2013.

[56] Coutts, K., "Kinetic differences of two volleyball jumping techniques," *Medicine & Science in Sports & Exercise*, 1982.

[57] Daniels, K. E. and Behringer, R. P., "Hysteresis and competition between disorder and crystallization in sheared and vibrated granular flow," *Physical review letters*, vol. 94, no. 16, p. 168001, 2005.

[58] de Bruyn, J. R. and Walsh, A. M., "Penetration of spheres into loose granular media," *Canadian Journal of Physics*, vol. 82, no. 6, pp. 439–446, 2004.

[59] Demes, B., Jungers, W., Fleagle, J., Wunderlich, R., Richmond, B., and Lemelin, P., "Body size and leaping kinematics in Malagasy vertical clingers and leapers," *Journal of Human Evolution*, vol. 31, pp. 367–388, Oct. 1996.

[60] Demes, B., Jungers, W., Gross, T., and Fleagle, J., "Kinetics of Leaping Primates: Influence of Substrate Orientation and Compliance," *American Journal of Physical Anthropology*, vol. 96, no. 4, pp. 419–429, 1995.

[61] Dickinson, M. H., Farley, C., Full, R., Koehl, M., Kram, R., and Lehman, S., "How Animals Move: An Integrative View," *Science*, vol. 288, pp. 100–106, Apr. 2000.

[62] Ding, Y., Gravish, N., and Goldman, D., "Drag induced lift in granular media," *Physical Review Letters*, vol. 106, no. 2, p. 028001, 2011.

[63] Ding, Y., Sharpe, S. S., Wiesenfeld, K., and Goldman, D. I., "Emergence of the advancing neuromechanical phase in a resistive force dominated medium," pp. 9746–9751, 2013.

[64] Ding, Y., Sharpe, S. S., Masse, A., and Goldman, D. I., "Mechanics of undulatory swimming in a frictional fluid," *PLoS Computational Biology*, vol. 8, no. 12, p. e1002810, 2012.

[65] Emerson, S., "Allometry and Jumping in Frogs : Helping the Twain meet," *Evolution*, vol. 32, no. 3, pp. 551–564, 1978.

[66] Emerson, S., "Jumping and leaping," *Functional vertebrate morphology*, 1985.

[67] Ergun, S., "Fluid flow through packed columns," *Chem. Eng. Prog.*, vol. 48, pp. 89–94, 1952.

[68] Essner, R. L., "Three-dimensional launch kinematics in leaping, parachuting and gliding squirrels.," *The Journal of experimental biology*, vol. 205, pp. 2469–77, Aug. 2002.

[69] Euler, L., "1745 neue grundsätze der artillerie; reprinted in euler's opera omnia," *Druck und Verlag Von B.G. Teubner*, vol. 2, no. 14, 1922.

[70] Evans, M. E. G., "The jump of the click beetle (Coleoptera, Elateridae)-a preliminary study," *Journal of Zoology*, vol. 167, pp. 319–336, Aug. 1972.

[71] Farley, C. T. and Gonzalez, O., "Leg stiffness and stride frequency in human running," *Journal of biomechanics*, vol. 29, no. 2, pp. 181–186, 1996.

[72] Farley, C. T., Houdijk, H. H., Van Strien, C., and Louie, M., "Mechanism of leg stiffness adjustment for hopping on surfaces of different stiffnesses," *Journal of applied physiology*, vol. 85, no. 3, pp. 1044–1055, 1998.

[73] Forrestal, M. and Luk, V., "Penetration into soil targets," *International Journal of Impact Engineering*, vol. 12, no. 3, pp. 427–444, 1992.

[74] Forterre, Y. and Pouliquen, O., "Flows of dense granular media," *Annual Review of Fluid Mechanics*, vol. 40, pp. 1–24, 2008.

[75] Francois, N., Saadatfar, M., Cruikshank, R., and Sheppard, A., "Geometrical frustration in amorphous and partially crystallized packings of spheres," *Physical review letters*, vol. 111, no. 14, p. 148001, 2013.

[76] Full, R. J. and Koditschek, D. E., "Templates and anchors: neuromechanical hypotheses of legged locomotion on land.," *The Journal of experimental biology*, vol. 202, pp. 3325–32, Dec. 1999.

[77] Galantis, A. and Woledge, R., "The theoretical limits to the power output of a muscletendon complex with inertial and gravitational loads," *Proceedings of the Royal Society of London. Series B: Biological Sciences*, vol. 207, no. 1523, pp. 1493–1498, 2003.

[78] German, J., "Hop to it: Sandia hoppers leapfrog conventional wisdom about robot mobility," *Sandia Lab News*, vol. 52, no. 21, 2000.

[79] Ghiringhelli, G. L., Masarati, P., Mantegazza, P., and Nixon, M. W., "Multi-body analysis of a tiltrotor configuration," *Nonlinear Dynamics*, vol. 19, no. 4, pp. 333–357, 1999.

[80] Glasheen, J. and McMahon, T., "A hydrodynamic model of locomotion in the basilisk lizard," *Nature*, vol. 380, no. 6572, pp. 340–341, 1996.

[81] Goldstein, S., *Modern developments in fluid dynamics: an account of theory and experiment relating to boundary layers, turbulent motion and wakes*, vol. 1. Clarendon Press, 1938.

[82] Gonthier, Y., McPhee, J., Lange, C., and Piedboeuf, J.-C., "A regularized contact model with asymmetric damping and dwell-time dependent friction," *Multibody System Dynamics*, vol. 11, no. 3, pp. 209–233, 2004.

[83] Gravish, N., Umbanhowar, P. B., and Goldman, D. I., "Force and flow at the onset of drag in plowed granular media," *Physical Review E*, vol. 89, no. 4, p. 042202, 2014.

[84] Gray, J., *How animals move*. 1953.

[85] Gray, J. and Hancock, G. J., "The propulsion of sea-urchin spermatozoa," *Journal of Experimental Biology*, vol. 32, no. 4, pp. 802–814, 1955.

[86] Guckenheimer, J. and Holmes, P., *Nonlinear oscillations, dynamical systems, and bifurcations of vector fields*. Applied mathematical sciences, New York: Springer-Verlag, 1983.

[87] Günther, M., "Biomechanical prerequisites for the leap-off of Senegal galagos.," *Zeitschrift für Morphologie und Anthropologie*, 1985.

[88] Günther, M., Ishida, H., Kumakura, H., and Nakano, Y., "The jump as a fast mode of locomotion in arboreal and terrestrial biotopes," *Zeitschrift für Morphologie und Anthropologie*, vol. 78, no. 3, pp. 341–372, 1991.

[89] Hale, E., Schara, N., Burdick, J., and Fiorini, P., "A minimally actuated hopping rover for exploration of celestial bodies," in *Robotics and Automation, 2000. Proceedings. ICRA'00. IEEE International Conference on*, vol. 1, pp. 420–427, Ieee, 2000.

[90] Hall-Craggs, E. C., "an Osteometric Study of the Hind Limb of the Galagidae.," *Journal of anatomy*, vol. 99, pp. 119–26, Jan. 1965.

[91] Harris, M. a. and Steudel, K., "The relationship between maximum jumping performance and hind limb morphology/physiology in domestic cats (Felis silvestris catus).," *The Journal of experimental biology*, vol. 205, pp. 3877–89, Dec. 2002.

[92] Hatze, H., "A comprehensive model for human motion simulation and its application to the take-off phase of the long jump," *Journal of Biomechanics*, vol. 14, no. 3, pp. 135–142, 1981.

[93] Hayashi, R. and Tsujio, S., "High-performance jumping movements by pendulum-type jumping machines," in *Intelligent Robots and Systems, 2001. Proceedings. 2001 IEEE/RSJ International Conference on*, pp. 722–727, 2001.

[94] Heitler, W., "The locust jump. Specialisations of the metathoracic femoral-tibial joint," *J. comp. Physiol*, 1974.

[95] Hereid, A., Cousineau, E. A., Hubicki, C. M., and Ames, A. D., "3D Dynamic Walking with Underactuated Humanoid Robots: A Direct Collocation Framework for Optimizing Hybrid Zero Dynamics," in *IEEE Conference on Robotics and Automation (accepted)*, pp. 1–8, 2016.

[96] Hill, A., "The heat of shortening and the dynamic constants of muscle," *Proceedings of the Royal Society of London. Series B, Biological Sciences*, vol. 126, no. 843, pp. 136–195, 1938.

[97] Hill, A., "The dimensions of animals and their muscular dynamics," 1949.

[98] Hof, A., "In vivo measurement of the series elasticity release curve of human triceps surae muscle," *Journal of biomechanics*, vol. 31, pp. 793–800, Sept. 1998.

[99] Hoover, A. M., Burden, S., Shankar Sastry, S., and Fearing, R. S., "Bio-inspired design and dynamic maneuverability of a minimally actuated six-legged robot," *2010 3rd IEEE RAS & EMBS International Conference on Biomedical Robotics and Biomechatronics*, pp. 869–876, Sept. 2010.

[100] Horita, T., Komi, P. V., Nicol, C., and Kyröläinen, H., "Interaction between pre-landing activities and stiffness regulation of the knee joint musculoskeletal system in the drop jump: implications to performance.," *European journal of applied physiology*, vol. 88, pp. 76–84, Nov. 2002.

[101] Hubbard, M. and Trinkle, J., "Clearing maximum height with constrained kinetic energy," *Journal of applied mechanics*, vol. 52, no. 1, pp. 179–184, 1985.

[102] Hubicki, C., Jones, M., Daley, M., and Hurst, J., "Do Limit Cycles Matter in the Long Run? Stable Orbits and Sliding-Mass Dynamics Emerge in Task-Optimal Locomotion,"

[103] Hubicki, C. M., Aguilar, J. J., Goldman, D. I., and Ames, A. D., "Tractable terrain-aware motion planning on granular media: An impulsive jumping study, in review," in *Intelligent Robots and Systems (IROS), 2016 IEEE/RSJ International Conference on*, IEEE, 2016.

[104] Hyon, S. H. and Mita, T., "Development of a Biologically Inspired Hopping Robot "Kenken"," in *International Conference on Robotics and Automation*, no. May, pp. 3984–3991, 2002.

[105] Impellizzeri, F. M., Rampinini, E., Castagna, C., Martino, F., Fiorini, S., and Wisloff, U., "Effect of plyometric training on sand versus grass on muscle soreness and jumping and sprinting ability in soccer players," *British journal of sports medicine*, vol. 42, no. 1, pp. 42–46, 2008.

[106] James, C., Sacco, P., and Jones, D., "Loss of power during fatigue of human leg muscles.," *The Journal of physiology*, vol. 484, no. 1, pp. 237–246, 1995.

[107] James, R. S., Navas, C. a., and Herrel, A., "How important are skeletal muscle mechanics in setting limits on jumping performance?," *The Journal of experimental biology*, vol. 210, pp. 923–33, Mar. 2007.

[108] James, R., Wilson, R., de Carvalho, J., Kohlsdorf, T., Gomes, F., and Navas, C., "Interindividual differences in leg muscle mass and pyruvate kinase activity correlate with interindividual differences in jumping performance of hyla multilineata," *Physiological and Biochemical Zoology*, vol. 78, no. 5, pp. 857–867, 2005.

[109] Jenkins, J. and Richman, M., "Grads 13-moment system for a dense gas of inelastic spheres," *Arch. Rat. Mech. Anal.*, vol. 87, p. 355, 1985.

[110] Jerkins, M., Schröter, M., Swinney, H. L., Senden, T. J., Saadatfar, M., and Aste, T., "Onset of mechanical stability in random packings of frictional spheres," *Physical review letters*, vol. 101, no. 1, p. 018301, 2008.

[111] Johansson, K. H., Sastry, S., Zhang, J., and Lygeros, J., "Zeno hybrid systems," *International Journal of Robust & Nonlinear Control*, vol. 11, no. 435-451, p. 6, 2001.

[112] Jones, M. S., *Optimal Control of an Underactuated Bipedal Robot*. PhD thesis, 2014.

[113] Kamrin, K. and Koval, G., "Nonlocal constitutive relation for steady granular flow," *Physical Review Letters*, vol. 108, no. 17, p. 178301, 2012.

[114] Katsuragi, H. and Durian, D. J., "Unified force law for granular impact cratering," *Nature Physics*, vol. 3, pp. 420–423, Apr. 2007.

[115] Katsuragi, H. and Durian, D. J., "Drag force scaling for penetration into granular media," *Physical Review E*, vol. 87, p. 052208, May 2013.

[116] Keith, M., Scheibe, J., and Hendershott, A., "Launch dynamics in Glaucomys volans," *Biology of gliding mammals*, 2000.

[117] Ker, R., Dimery, N., and Alexander, R., "The role of tendon elasticity in hopping in a wallaby (Macropus rufogriseus)," *Journal of Zoology*, 1986.

[118] Kikuchi, F., Ota, Y., and Hirose, S., "Basic performance experiments for jumping quadruped," in *Intelligent Robots and Systems, 2003.(IROS 2003). Proceedings. 2003 IEEE/RSJ International Conference on*, 2003.

[119] Koditschek, D. and Bühler, M., "Analysis of a simplified hopping robot," *The International Journal of Robotics Research*, vol. 10, no. 6, pp. 587–605, 1991.

[120] Komi, P. and Bosco, C., "Utilization of stored elastic energy in leg extensor muscles by men and women.," *Medicine and Science in Sports*, 1978.

[121] Komsuoglu, H., Majumdar, A., Aydin, Y. O., and Koditschek, D. E., "Characterization of dynamic behaviors in a hexapod robot," in *Experimental Robotics*, pp. 667–684, Springer, 2014.

[122] Kovac, M., Fuchs, M., Guignard, A., Zufferey, J., and Floreano, D., "A miniature 7g jumping robot," in *ICRA 2008. IEEE International Conference on Robotics and Automation*, no. figure 3, pp. 373–378, IEEE, 2008.

[123] Kubo, K., Kawakami, Y., Fukunaga, T., James, R. S., Navas, C. A., and Herrel, A., "Influence of elastic properties of tendon structures on jump performance in humans," *Journal of Applied Physiology*, no. 87, pp. 2090–2096, 1999.

[124] Le Bouil, A., Amon, A., McNamara, S., and Crassous, J., "Emergence of cooperativity in plasticity of soft glassy materials," *Physical review letters*, vol. 112, no. 24, p. 246001, 2014.

[125] Leavitt, J., Bobrow, J., and Sideris, A., "Robust balance control of a one-legged, pneumatically-actuated, acrobot-like hopping robot," in *Robotics and Automation, 2004. Proceedings. ICRA'04. 2004 IEEE International Conference on*, 2004.

[126] Lee, W. and Raibert, M., "Control of hoof rolling in an articulated leg," in *Proceedings. 1991 IEEE International Conference on Robotics and Automation*, pp. 1386–1391, IEEE Comput. Soc. Press, 1991.

[127] Li, C., Hsieh, S. T., and Goldman, D. I., "Multi-functional foot use during running in the zebra-tailed lizard (callisaurus draconoides)," *The Journal of experimental biology*, vol. 215, no. 18, pp. 3293–3308, 2012.

[128] Li, C. and Umbanhowar, P., "Sensitive dependence of the motion of a legged robot on granular media," *Proceedings of the*, vol. 106, no. 9, pp. 3029–3034, 2009.

[129] Li, C., Zhang, T., and Goldman, D. I., "A terradynamics of legged locomotion on granular media," *Science*, vol. 339, no. 6126, pp. 1408–1412, 2013.

[130] Losos, J., "The evolution of form and function: morphology and locomotor performance in West Indian Anolis lizards," *Evolution*, 1990.

[131] Lötstedt, P., "Mechanical systems of rigid bodies subject to unilateral constraints," *SIAM Journal on Applied Mathematics*, vol. 42, no. 2, pp. 281–296, 1982.

[132] Lutz, G. J. and Rome, L. C., "Built for jumping: the design of the frog muscular system.," *Science (New York, N.Y.)*, vol. 263, pp. 370–2, Jan. 1994.

[133] Maladen, R. D., Ding, Y., Li, C., and Goldman, D. I., "Undulatory swimming in sand: subsurface locomotion of the sandfish lizard," *science*, vol. 325, no. 5938, pp. 314–318, 2009.

[134] Maladen, R. D., Ding, Y., Umbanhowar, P. B., and Goldman, D. I., "Undulatory swimming in sand: experimental and simulation studies of a robotic sandfish," *The International Journal of Robotics Research*, vol. 30, no. 7, pp. 793–805, 2011.

[135] Maladen, R. D., Ding, Y., Umbanhowar, P. B., Kamor, A., and Goldman, D. I., "Mechanical models of sandfish locomotion reveal principles of high performance subsurface sand-swimming," *Journal of The Royal Society Interface*, vol. 8, no. 62, pp. 1332–1345, 2011.

[136] Man, H. D., Lefeber, D., and Vermeulen, J., "Control on irregular terrain of a hopping robot with one articulated leg," *ICAR Workshop II: New Approaches on Dynamic ...*, 1997.

[137] Manchester, I. R., Mettin, U., Iida, F., and Tedrake, R., "Stable dynamic walking over uneven terrain," *The International Journal of Robotics Research*, vol. 30, no. 3, pp. 265–279, 2011.

[138] Marques, M. D. P. M., *Differential inclusions in nonsmooth mechanical problems: Shocks and dry friction*, vol. 9. Birkhauser, 1993.

[139] Marsh, R., "Jumping ability of anuran amphibians," *Advances in veterinary science and comparative medicine*, vol. 38, pp. 51–111, 1994.

[140] Marsh, R., "Jumping ability of anurans.," pp. 51 – 111, 1994.

[141] Matsuoka, K., "A mechanical model of repetitive hopping movements," *Biomechanisms*, vol. 5, no. 2, pp. 251–258, 1980.

[142] McGeer, T., "Passive dynamic walking," *The International Journal of Robotics Research*, 1990.

[143] McGowan, C., "The mechanics of jumping versus steady hopping in yellow-footed rock wallabies," *Journal of experimental biology*, vol. 208, no. 14, pp. 2741–2751, 2005.

[144] McMahon, T. a. and Cheng, G. C., "The mechanics of running: how does stiffness couple with speed?," *Journal of biomechanics*, vol. 23 Suppl 1, pp. 65–78, Jan. 1990.

[145] McMahon, T. A. and Cheng, G. C., "The mechanics of running: how does stiffness couple with speed?," *Journal of biomechanics*, vol. 23, pp. 65–78, 1990.

[146] McNeill Alexander, R., *Elastic mechanisms in animal movement*. Cambridge [etc.]: Cambridge University Press, 1988.

[147] Mehrandezh, M., "Jumping height control of an electrically actuated, one-legged hopping robot: modelling and simulation," *Decision and Control, 1995., Proceedings of the 34th IEEE Conference on*, 1995.

[148] Moreau, J. J., "Standard inelastic shocks and the dynamics of unilateral constraints," in *Unilateral problems in structural analysis*, pp. 173–221, Springer, 1985.

[149] Moritz, C. T. and Farley, C. T., "Human hopping on very soft elastic surfaces: implications for muscle pre-stretch and elastic energy storage in locomotion," *Journal of Experimental Biology*, vol. 208, no. 5, pp. 939–949, 2005.

[150] Morrey, J. and Lambrecht, B., "Highly mobile and robust small quadruped robots," in *Intelligent Robots and Systems, 2003.(IROS 2003). Proceedings. 2003 IEEE/RSJ International Conference on*, 2003.

[151] Muramatsu, S., Fukudome, A., Miyama, M., Arimoto, M., and Kijima, A., "Energy expenditure in maximal jumps on sand," *Journal of physiological anthropology*, vol. 25, no. 1, pp. 59–61, 2006.

[152] Newhall, K. and Durian, D., "Projectile-shape dependence of impact craters in loose granular media," *Physical Review E*, vol. 68, no. 6, p. 060301, 2003.

[153] Niiyama, R. and Kuniyoshi, Y., "A Pneumatic Biped with an Artificial Musculoskeletal System," in *4th Int. Symposium on Adaptive Motion of Animals and Machines*, pp. 80–81, 2008.

[154] Niiyama, R., Nagakubo, A., and Kuniyoshi, Y., "Mowgli: A bipedal jumping and landing robot with an artificial musculoskeletal system," in *Robotics and Automation, 2007 IEEE International Conference on*, no. April, pp. 2546–2551, IEEE, 2007.

[155] Ohashi, E. and Ohnishi, K., "Hopping height control for hopping robots," *Electrical Engineering in Japan*, vol. 155, pp. 64–71, Apr. 2006.

[156] Okubo, O., Nakano, E., and Handa, M., "Design of a jumping machine using self-energizing spring," *Intelligent Robots and Systems' 96, IROS 96, Proceedings of the 1996 IEEE/RSJ International Conference on*, 1996.

[157] Pandy, M. G., Zajac, F. E., Sim, E., and Levine, W. S., "An optimal control model for maximum-height human jumping.," *Journal of biomechanics*, vol. 23, pp. 1185–98, Jan. 1990.

[158] Pandy, M. and Zajac, F., "Optimal muscular coordination strategies for jumping," *Journal of biomechanics*, vol. 24, no. 1, pp. 1–10, 1991.

[159] Pang, J.-S. and Trinkle, J. C., "Complementarity formulations and existence of solutions of dynamic multi-rigid-body contact problems with coulomb friction," *Mathematical programming*, vol. 73, no. 2, pp. 199–226, 1996.

[160] Papantoniou, K., "Electromechanical design for an electrically powered, actively balanced one leg planar robot," *Intelligent Robots and Systems' 91.'Intelligence for Mechanical Systems, Proceedings IROS'91. IEEE/RSJ International Workshop on*, 1991.

[161] Peck, M., "Dynamics of a gyroscopic hopping rover," in *Proceeding of the 11 th Annual AAS/AIAA Space Flight Mechanics Meeting, Santa Barbara, CA*, 2001.

[162] Pfeifer, R., Lungarella, M., and Iida, F., "Self-organization, embodiment, and biologically inspired robotics.," *Science (New York, N.Y.)*, vol. 318, pp. 1088–93, Nov. 2007.

[163] Playter, R., Buehler, M., and Raibert, M., "Bigdog, unmanned systems technology viii," in *Proc. SPIE*, vol. 6230, 2006.

[164] Poncelet, J. V., "Cours de mecanique industrielle," *Paris (1829/1835)*, 1829.

[165] Pöschel, T. and Schwager, T., *Computational granular dynamics: models and algorithms*. Springer Science & Business Media, 2005.

[166] Pouliquen, O. and Forterre, Y., "A non-local rheology for dense granular flows," *Philosophical Transactions of the Royal Society of London A: Mathematical, Physical and Engineering Sciences*, vol. 367, no. 1909, pp. 5091–5107, 2009.

[167] Pratt, G. A. and Williamson, M. M., "Series elastic actuators," in *Intelligent Robots and Systems 95.'Human Robot Interaction and Cooperative Robots', Proceedings. 1995 IEEE/RSJ International Conference on*, vol. 1, pp. 399–406, IEEE, 1995.

[168] Prosser, J. and Kam, M., "Vertical control for a mechanical model of the one-legged hopping machine," in *Control Applications, 1992., First IEEE Conference on*, 1992.

[169] Qian, F., Zhang, T., Korff, W., Umbanhowar, P. B., Full, R. J., and Goldman, D. I., "Principles of appendage design in robots and animals determining terradynamic performance on flowable ground," *Bioinspiration & biomimetics*, vol. 10, no. 5, p. 056014, 2015.

[170] Qian, F., Zhang, T., Li, C., Masarati, P., Birkmeyer, P., Pullin, A., Hoover, A., Fearing, R. S., and Golman, D. I., "Walking and running on yielding and fluidizing ground," *RSS*, p. 345, 2013.

[171] Raibert, M., "Running on four legs as though they were one," *Robotics and Automation, IEEE Journal of*, vol. 2, no. 2, pp. 70–82, 1986.

[172] Raibert, M., *Legged robots that balance*. The MIT Press, Cambridge, MA, 1985.

[173] Raibert, M. and Brown Jr., H., "Experiments in balance with a 2D one-legged hopping machine," *Journal of Dynamic Systems, Measurement, and Control*, vol. 106, pp. 75–81, 1984.

[174] Rand, A., "Jumping ability of certain anurans, with notes on endurance," *Copeia*, vol. 1952, no. 1, pp. 15–20, 1952.

[175] Rand, A. and Rand, P., "The relation of size and distance jumped in Bufo marinus," *Herpetologica*, vol. 22, no. 3, pp. 206–209, 1966.

[176] Rapaport, D. C., *The art of molecular dynamics simulation*. Cambridge, UK: Cambridge University Press, 2004.

[177] Richardson, E., "The impact of a solid on a liquid surface," *Proceedings of the Physical Society*, vol. 61, no. 4, p. 352, 1948.

[178] Ringrose, R., "Self-stabilizing running," in *Robotics and Automation, 1997. Proceedings., 1997 IEEE International Conference on*, 1997.

[179] Roberts, T. and Marsh, R., "Probing the limits to muscle-powered accelerations: lessons from jumping bullfrogs," *Journal of Experimental Biology*, vol. 206, no. 15, pp. 2567—-2580, 2003.

[180] Robins, B. and Curtis, W., *New principles of gunnery*. Richmond Publishing Company Limited, 1972.

[181] Sakakibara, J., Nakagawa, M., and Yoshida, M., "Stereo-piv study of flow around a maneuvering fish," *Experiments in fluids*, vol. 36, no. 2, pp. 282–293, 2004.

[182] Sato, A., *A Planar Hopping Robot with One Actuator*. PhD thesis, 2004.

[183] Sayyad, A., Seth, B., and Seshu, P., "Single-legged hopping robotics research A review," *Robotica*, vol. 25, pp. 1–27, Apr. 2007.

[184] Scarfogliero, U., Stefanini, C., and Dario, P., "Design and Development of the Long-Jumping Grillo Mini Robot," in *2007 IEEE ICRA*, no. April, (Rome, Italy), pp. 10–14, 2007.

[185] Schofield, A. and Wroth, P., "Critical state soil mechanics," 1968.

[186] Seguin, A., Bertho, Y., and Gondret, P., "Influence of confinement on granular penetration by impact," *Physical Review E*, vol. 78, no. 1, p. 010301, 2008.

[187] Seyfarth, A., Blickhan, R., and Van Leeuwen, J., "Optimum take-off techniques and muscle design for long jump," *Journal of Experimental Biology*, vol. 203, no. 4, pp. 741–750, 2000.

[188] Sharpe, S. S., Ding, Y., and Goldman, D. I., "Environmental interaction influences muscle activation strategy during sand-swimming in the sandfish lizard *Scincus scincus*," *The Journal of Experimental Biology*, vol. 216, no. 2, pp. 260–274, 2012.

[189] Stewart, D. E., "Rigid-body dynamics with friction and impact," *SIAM review*, vol. 42, no. 1, pp. 3–39, 2000.

[190] Stewart, D. E. and Trinkle, J. C., "An implicit time-stepping scheme for rigid body dynamics with inelastic collisions and coulomb friction," *International Journal for Numerical Methods in Engineering*, vol. 39, no. 15, pp. 2673–2691, 1996.

[191] Stoeter, S. and Rybski, P., "Autonomous stair-hopping with scout robots," in *Intelligent Robots and Systems, 2002. IEEE/RSJ International Conference on*, 2002.

[192] Stone, M. B., Bernstein, D. P., Barry, R., Pelc, M. D., Tsui, Y.-K., and Schiffer, P., "Stress propagation: Getting to the bottom of a granular medium," *Nature*, vol. 427, no. 6974, pp. 503–504, 2004.

[193] Stone, M., Barry, R., Bernstein, D., Pelc, M., Tsui, Y., and Schiffer, P., "Local jamming via penetration of a granular medium," *Physical Review E*, vol. 70, no. 4, p. 041301, 2004.

[194] Takeuchi, K. and Kuswadi, S., "Continuous hopping motion control experiment of one linear actuator robot," in *SICE 2002. Proceedings of the 41st SICE Annual Conference*, 2002.

[195] Tapia, F., Espíndola, D., Hamm, E., and Melo, F., "Effect of packing fraction on shear band formation in a granular material forced by a penetrometer," *Physical Review E*, vol. 87, no. 1, p. 014201, 2013.

[196] Tasora, A. and Anitescu, M., "A matrix-free cone complementarity approach for solving large-scale, nonsmooth, rigid body dynamics," *Computer Methods in Applied Mechanics and Engineering*, vol. 200, no. 5, pp. 439–453, 2011.

[197] Treff, H., "Der Absprungwinkel beim schrägen Sprung des Galagos (Galago senegalensis)," *Journal of Comparative Physiology A: Neuroethology, Sensory, Neural, and Behavioral Physiology*, vol. 132, 1970.

[198] Tsimring, L. S. and Volfson, D., "Modeling of impact cratering in granular media," in *Powders and Grains 2005* (García-Rojo, R., Herrmann, H. J., and McNamara, S., eds.), vol. 2, pp. 1215–1223, 2005.

[199] Tsimring, L. and Volfson, D., "Modeling of impact cratering in granular media," *Powders and grains*, vol. 2, pp. 1215–1223, 2005.

[200] Tsukagoshi, H. and Sasaki, M., "Design of a higher jumping rescue robot with the optimized pneumatic drive," in *Robotics and Automation, 2005. ICRA 2005. Proceedings of the 2005 IEEE International Conference on*, no. April, pp. 1276–1283, 2005.

[201] Tufillaro, N. B., Mello, T. M., Choi, Y. M., and Albano, A. M., "Period doubling boundaries of a bouncing ball," *Journal De Physique*, vol. 47, no. 9, pp. 1477–1482, 1986. Times Cited: 29.

[202] Uehara, J., Ambroso, M., Ojha, R., and Durian, D., "Low-speed impact craters in loose granular media," *Physical Review Letters*, vol. 90, no. 19, p. 194301, 2003.

[203] Umbanhowar, P. and Goldman, D., "Granular impact and the critical packing state," *Physical Review E*, vol. 82, pp. 1–4, July 2010.

[204] Uno, K., Ohmori, M., and Kondo, R., "A hopping robot with impulsive actuator," in *SICE 2002. Proceedings of the 41st SICE Annual Conference*, 2002.

[205] van Soest, A., Schwab, A., Bobbert, M., and van Ingen Schenau, G., "The influence of the biarticularity of the gastrocnemius muscle on vertical-jumping achievement," *Journal of biomechanics*, vol. 26, no. 1, pp. 1–8, 1993.

[206] Vanhooydonck, B. and Aerts, P., "Power generation during locomotion in Anolis lizards: an ecomorphological approach," *Ecology and Biomechanics: A Mechanical Approach to the Ecology of Animals and Plants*, pp. 253–269, 2006.

[207] Vogel, S., *Life's devices: the physical world of animals and plants*. Princeton University Press, 1988.

[208] Voigt, M., Simonsen, E., Dyhre-Poulsen, P., and Klausen, K., "Mechanical and muscular factors influencing the performance in maximal vertical jumping after different prestretch loads," *Journal of biomechanics*, vol. 28, no. 3, 1995.

[209] von Stryk, O. and Bulirsch, R., "Direct and indirect methods for trajectory optimization," *Annals of Operations Research*, vol. 37, pp. 357–373, 1992.

[210] Wagner, H., "Phenomena associated with impacts and sliding on liquid surfaces," *Z. Angew. Math. Mech*, vol. 12, no. 4, pp. 193–215, 1932.

[211] Waitukaitis, S. R. and Jaeger, H. M., "Impact-activated solidification of dense suspensions via dynamic jamming fronts," *Nature*, vol. 487, no. 7406, pp. 205–209, 2012.

[212] Walsh, A. M., Holloway, K. E., Habdas, P., and de Bruyn, J. R., "Morphology and scaling of impact craters in granular media," *Physical review letters*, vol. 91, no. 10, p. 104301, 2003.

[213] Wei, T., Nelson, G., and Quinn, R., "Design of a 5-cm monopod hopping robot," in *Robotics and Automation, 2000. Proceedings. ICRA'00. IEEE International Conference on*, 2000.

[214] Westervelt, E., Grizzle, J. W., and Koditschek, D. E., "Hybrid Zero Dynamics of Planar Biped Walkers," *IEEE Transactions on Automatic Control*, vol. 48, pp. 42–56, jan 2003.

[215] Wilson, R., Franklin, C., and James, R., "Allometric scaling relationships of jumping performance in the striped marsh frog Limnodynastes peronii," *Journal of Experimental Biology*, vol. 1946, pp. 1937–1946, 2000.

[216] Woledge, R., Curtin, N., and Homsher, E., "Energetic aspects of muscle contraction.," *Monographs of the Physiological society*, vol. 41, p. 1, 1985.

[217] Wu, J., Yu, B., and Yun, M., "A resistance model for flow through porous media," *Transport in porous media*, vol. 71, no. 3, pp. 331–343, 2008.

[218] Yeadon, M., "The simulation of aerial movement II. A mathematical inertia model of the human body," *Journal of Biomechanics*, 1990.

[219] Zajac, F., Zomlefer, M., and Levine, W., "Hindlimb muscular activity, kinetics and kinematics of cats jumping to their maximum achievable heights," *Journal of Experimental Biology*, vol. 94304, no. 153, pp. 73–86, 1981.

[220] Zajac, F. E., "Muscle coordination of movement: a perspective," *Journal of Biomechanics*, vol. 26, pp. 109–124, 1993.

[221] Zeglin, G., *Uniroo–a one legged dynamic hopping robot.* Dissertation, Massachusetts Institute of Technology, 1991.

[222] Zhang, L., Xu, D., Makhsous, M., and Lin, F., "Stiffness and viscous damping of the human leg," in *Proc. of the 24th Ann. Meeting of the Am. Soc. of Biomech., Chicago, IL*, 2000.

[223] Zhang, T. and Goldman, D. I., "The effectiveness of resistive force theory in granular locomotion," *Physics of Fluids (1994-present)*, vol. 26, no. 10, p. 101308, 2014.

[224] Zhang, T., Qian, F., Li, C., Masarati, P., Hoover, A. M., Birkmeyer, P., Pullin, A., Fearing, R. S., and Goldman, D. I., "Ground fluidization promotes rapid running of a lightweight robot," *The International Journal of Robotics Research*, vol. 32, no. 7, pp. 859–869, 2013.

[225] Zhang, W. and Wang, G., "Toward a folding-legged uniped that can learn to jump," in *Systems, Man, and Cybernetics, 1997. Computational Cybernetics and Simulation., 1997 IEEE International Conference on*, 1997.

[226] Zug, G., "Anuran locomotion: structure and function. I. Preliminary observations on relation between jumping and osteometrics of appendicular and postaxial skeleton," *Copeia*, 1972.

[227] Zug, G., "Anuran locomotion-structure and function, II: Jumping performance of semiaquatic, terrestrial, and arboreal frogs.," *Smithsonian Contributions to Zoology*, no. 276, 1978.

Probing the dynamics of a simple jumping robot on hard and soft ground

Jeffrey J. Aguilar

170 Pages

Directed by Professor Daniel I. Goldman

Jumping is an important behavior for many animals and robots. Unlike periodic gaits such as hopping or running, whereby energy generated in previous cycles can be leveraged to efficiently sustain motion, jumping relies almost purely on a transient burst of activity to produce take-off from rest. While bioinspired robots have utilized some jumping mechanisms revealed from numerous biological studies, there have been few systematic studies of the dynamics of these transient behaviors, particularly on complex media like sand. This dissertation presents a robophysics approach (the pursuit of principles of self generated motion) to systematically study the dynamics of jumping on both hard and deformable ground. For jumping on hard ground, the present work expands on the results from Aguilar et al. [3], which characterized the dependence of jumping performance on the robot's hybrid air/ground dynamics, and analyses how relative jumping performance and power requirements of different actuation strategies change at different scales of mass, gravity, stiffness and forcing amplitude. To contrast with the dynamics of jumps on hard ground (in which the unyielding ground supplies the necessary normal force to counteract downward motion), we study a relatively simple deformable medium: dry granular media, which can exhibit both solid and fluid-like dynamics. Through the simultaneous analysis of both the robot and granular dynamics during jumping, our study reveals not only actuation principles crucial to jumping on complex media, but also new granular physics [2], like an added mass effect induced by a jammed granular cone beneath the robot's foot. Additionally, in collaboration with the Professor Aaron Ames' group at Georgia Tech, we incorporate these granular dynamics into a motion planning

optimizer to produce optimal open loop controlled jumps.